



UNIVERSIDAD DE LAS PALMAS DE GRAN CANARIA
Institute for Applied Microelectronics
Information and Communication Systems

Master of Science in Telecommunication Technologies



Master's Thesis

Evaluation of band selection techniques in the classification of hyperspectral images of brain tumors

Author: Mrs. Beatriz Martínez Vega
Supervisor(s): Dr. Gustavo Marrero Callicó
Dr. Himar Fabelo Gómez
Mr. Samuel Ortega Sarmiento
Date: July 2019



t +34 928 451 150
+34 928 451 086
f +34 928 451 083

e: iuma@iuma.ulpgc.es
w: www.iuma.ulpgc.es

Campus Universitario de Tafira
35017 Las Palmas de Gran Canaria



UNIVERSIDAD DE LAS PALMAS DE GRAN CANARIA
Institute for Applied Microelectronics
Information and Communication Systems

Master of Science in Telecommunication Technologies



Master's Thesis

**Evaluation of band selection techniques in the
classification of hyperspectral images of brain tumors**

Signatures

Author: Mrs. Beatriz Martínez Vega Signature:

Supervisor(s): Dr. Gustavo Marrero Callicó Signature:

Dr. Himar Fabelo Gómez Signature:

Mr. Samuel Ortega Sarmiento Signature:

Date: **July 2019**



t +34 928 451 150
+34 928 451 086
f +34 928 451 083

e: iuma@iuma.ulpgc.es
w: www.iuma.ulpgc.es

Campus Universitario de Tafira
35017 Las Palmas de Gran Canaria



UNIVERSIDAD DE LAS PALMAS DE GRAN CANARIA
Institute for Applied Microelectronics
Information and Communication Systems

Master of Science in Telecommunication Technologies



Master's Thesis

**Evaluation of band selection techniques in the
classification of hyperspectral images of brain tumors**

Evaluation

Grade:

President:

Signature:

Secretary:

Signature:

Member:

Signature:

Date: July 2019



t +34 928 451 150
+34 928 451 086
f +34 928 451 083

e: iuma@iuma.ulpgc.es
w: www.iuma.ulpgc.es

Campus Universitario de Tafira
35017 Las Palmas de Gran Canaria

Abstract

The main objective of this Master Thesis is to study and evaluate different band selection algorithms in order to identify the most relevant bands in hyperspectral (HS) images to allow an accurate delineation of brain tumors during surgical procedures. The employed HS database was composed of 26 HS images of in-vivo human brain obtained during neurosurgical procedures. For each image, a certain number of pixels were labeled in four different classes in order to create a labeled dataset, employed to develop and evaluate a classification model following a leave-one-patient-out cross-validation methodology using 6 test HS images. Four types of classes were defined: normal tissue, tumor tissue, hypervascularized tissue and background.

During the development of the project, different methodologies were carried out. Firstly, the most representative bands for each test HS image with different optimization algorithms were selected. After identifying these bands, all test images were evaluated using the coincident bands between the obtained results. The process starts by evaluating the test images with all the bands selected, then employing the bands that were repeated in at least two test images, and so on until reaching the maximum number of coincident levels in each case. Once this extensive evaluation was carried out, it was decided which set of bands were the ones that provided the most relevant information. The evaluation metrics employed in these experiments were: overall accuracy, sensitivity, specificity, Matthews correlation coefficient and the qualitative classification maps. The results obtained with the band selection algorithms were compared with the reference results employing all the bands in the HS images.

The results demonstrate that the proposed methodology based on the Genetic Algorithm optimization method improves the accuracy results in identifying different classes for brain cancer detection application, employing only 48 bands. The most relevant spectral ranges identified were: 440.5-465.96 nm, 498.71-509.62 nm, 556.91-575.1 nm, 593.29-615.12 nm, 636.94-666.05 nm, 698.79-731.53 nm and 884.32-902.51 nm.

Resumen

El objetivo principal de este Trabajo Fin de Máster es el de estudiar y evaluar diferentes algoritmos de selección de bandas para identificar las bandas más relevantes en imágenes hiperespectrales (HS) que permitan una delineación precisa de los tumores cerebrales durante los procedimientos quirúrgicos. La base de datos de HS empleada estaba compuesta por 26 imágenes de HS de cerebro humano in-vivo obtenidas durante procedimientos neuroquirúrgicos. En cada una de las imágenes, se etiquetó un cierto número de píxeles en cuatro clases para crear un conjunto de datos etiquetado que se empleó para desarrollar y evaluar un modelo de clasificación siguiendo una metodología de *cross-validation* de un paciente con 6 pruebas de imágenes de HS. Se definieron cuatro tipos de clases: tejido normal, tejido tumoral, tejido hipervascularizado y *background*.

Durante el desarrollo del proyecto se llevaron a cabo diferentes metodologías. Primero, se seleccionaron las bandas más representativas para cada imagen HS de test con diferentes algoritmos de optimización. Después de identificar estas bandas, todas las imágenes de test se evaluaron utilizando las bandas coincidentes entre los resultados obtenidos. Se comenzó por evaluar las imágenes de test con todas las bandas seleccionadas, luego empleando las bandas que se repitieron en al menos dos imágenes de test, y así sucesivamente hasta alcanzar el número máximo de niveles coincidentes en cada caso. Una vez que se llevó a cabo esta extensa evaluación, se decidió qué conjunto de bandas eran las que proporcionaban la información más relevante. Las métricas de evaluación empleadas en estos experimentos fueron: *overall accuracy*, sensibilidad, especificidad, *Matthews correlation coefficient* y mapas de clasificación cualitativos. Los resultados obtenidos con los algoritmos de selección de banda se compararon con los resultados de referencia empleando todas las bandas en las imágenes de HS.

Los resultados demuestran que la metodología propuesta basada en el método de optimización del algoritmo genético mejoró los resultados de *accuracy* en la identificación de las diferentes clases para la aplicación de detección de cáncer cerebral, empleando solo 48 bandas. Los rangos espectrales más relevantes identificados fueron: 440.5-465.96 nm, 498.71-509.62 nm, 556.91-575.1 nm, 593.29-615.12 nm, 636.94-666.05 nm, 698.79-731.53 nm y 884.32-902.51 nm.

Acknowledgements

This section is dedicated to all the people who, in one way or another, have helped me to develop this Master Thesis. I would like to thank my tutors, my friends and my family.

Thanks to my tutors, Gustavo, Himar and Samuel, for their time, patience and work, especially patience. Thanks to my family, for all the unconditional support they have given me to achieve my goal. Thanks to my friends, both outside and inside the race, for the moral support and giving me strength in the most difficult moments.

.

Contents

<i>Abstract</i>	i
<i>Resumen</i>	iii
<i>Acknowledgements</i>	v
List of Figures	9
List of Tables.....	11
List of Acronyms.....	13
Chapter 1: Introduction	15
1.1 Context.....	15
1.2 Objectives	16
1.3 Methodology	16
1.4 Document organization	17
Chapter 2: State-of-the-art.....	19
2.1 Introduction	19
2.2 Hyperspectral images.....	19
2.3 Dimensional reduction	20
2.3.1 Feature extraction methods.....	21
2.3.2 Feature selection methods	21
2.4 Band selection methods for HSI	21
2.5 Optimization algorithms	24
2.5.1 Genetic Algorithm.....	24
2.5.2 Particle Swarm Optimization.....	25
2.5.3 Ant Colony Optimization.....	26
2.6 Support Vector Machine Classifier	27
2.7 Summary.....	28
Chapter 3: In-Vivo HS Human Brain Image Database.....	29
3.1 Introduction	29
3.2 Intraoperative HS Acquisition System.....	29
3.3 Acquisition of HS images during surgery	30
3.3.1 Patient preparation.....	31
3.3.2 Hyperspectral image capture	32
3.3.3 Tissue resection	33
3.3.4 Expert evaluation	33
3.3.5 Samples labelling.....	33
3.3.6 Complete HS database	33
3.4 Summary.....	36
Chapter 4: Methodology.....	37
4.1 Introduction	37
4.2 Proposed processing frameworks	38
4.2.1 Evaluation metrics.....	38
4.2.2 Basic processing framework (BPF) with GA and PSO.....	43
4.2.3 Optimized processing framework (OPF) with GA and PSO.....	43
4.2.4 Reference results and evaluation methodology for the BPF	45
4.2.5 Reference results and evaluation methodology for the OPF.....	45
4.2.6 Band selection using the ACO algorithm.....	46
4.2.7 Evaluation of test database with the same bands	47
4.3 Summary.....	48
Chapter 5: Experimental results	49
5.1 Introduction	49
5.2 Band selection evaluation using BPF	50
5.2.1 Reference results.....	50
5.2.2 Genetic Algorithm evaluation	51
5.2.3 BPF with PSO evaluation	54
5.3 Band selection evaluation using OPF.....	57
5.3.1 Reference results.....	57
5.3.2 OPF with GA evaluation	58
5.3.3 OPF with PSO evaluation	60
5.4 Comparison of the BPF and OPF results	61

5.5 Band selection using the FoM evaluation metric.....	63
5.5.1 OPF with FoM evaluation metric	64
5.5.2 OPF with FoM ^{Penalized} evaluation metric	66
5.6 Comparison of the OPF results	68
5.7 Coincident selected bands evaluation	72
5.7.1 OPF with GA using FoM evaluation	72
5.7.2 OPF with GA using FoM ^{Penalized} evaluation	73
5.7.3 OPF with PSO using FoM ^{Penalized} evaluation	75
5.7.4 Comparison of the coincident selected bands results.....	76
5.8 Band selection evaluation using ACO algorithm	78
5.8.1 ACO with the entire training dataset.....	78
5.8.2 ACO with the reduced training dataset.....	79
5.8.3 Coincident selected bands evaluation using ACO	80
5.9 Summary.....	82
Chapter 6: Conclusions & Future Lines	87
6.1 Conclusions	87
6.2 Future lines.....	88
References.....	89

List of Figures

Figure 2-1. Structure of a hypercube and spectral signatures of a brain tumor [9].	20
Figure 2-2. The RMSEP values obtained by SPA, UVE, and BFWA [25].	22
Figure 2-3. The change curve classification accuracy for 3 HSI datasets [30].	23
Figure 2-4. Number of selected bands versus number of generations for the GA selection on 50, 100, 150 and 220 bands [31].	24
Figure 2-5. Recombination and mutation process.	25
Figure 2-6. Simulation of the selection process of the ant colonies of the best route between the nest and the food [40].	27
Figure 2-7. Support Vector Machine linear hyperplane between two classes [46].	28
Figure 3-1. HELICoiD demonstrator acquisition platform. (a, b) VNIR and NIR HS cameras mounted on the scanning platform; (c-e) Light source QTH connected to the fiber optic system for the transmission of light to obtain a light emission on the scanning platform; (f, g) stepper motor coupled to the shaft and connected to the stepper motor controller to perform the linear movement of the cameras; (h) Positioning of the camera used to identify the position of the field of vision of the cameras (FOV); (i) The Up & Down system used to focus the HS cameras; (j) and (k) Manual pan and tilt systems used to correctly orient the scanning platform [48].	30
Figure 3-2. Data acquisition and labelling procedure [51].	31
Figure 3-3. Meninges' structure [53].	32
Figure 3-4. IGS system pointer. (a) IGS system pointer over the tumor surface. (b) IGS system screen snapshot with the IGS system pointer coordinates [51].	32
Figure 4-1. Flow diagram of the general process to select the best bands.	38
Figure 4-2. Leave-One-Out Cross-Validation method [63].	39
Figure 4-3. Brain tumor (a) synthetic RGB and (b) classification map.	42
Figure 4-4. Graphic of the genetic algorithm generation.	42
Figure 4-5. Flow diagram of the BPF for the identification of the most representative bands for the GA and PSO algorithms.	43
Figure 4-6. Flow diagram of the training dataset optimization algorithm.	44
Figure 4-7. Flow diagram of the OPF for the identification of the most representative bands for the GA and PSO algorithms using the reduced training dataset.	44
Figure 4-8. Flow diagram of the evaluation metrics computation with the (a) entire labelled dataset and (b) with the selected bands.	45
Figure 4-9. Flow diagram of the evaluation metrics computation with (a) all bands (reference results) and (b) selected bands using the reduced labeled dataset.	46
Figure 4-10. Flow diagram of the (a) band selection process with the ACO algorithm and the (b) evaluation metrics computation with the selected bands.	47
Figure 5-1. Reference results obtained with all bands and the entire dataset for the SVM training. (a) Synthetic RGB representation of the HS cube with the tumor area surrounded by a yellow line. (b) Classification map.	51
Figure 5-2. Resulting classification maps after GA use with 30 generations and the entire dataset for the SVM training. (a) Synthetic RGB representation of the HS cube with the tumor area surrounded by a yellow line. (b) Reference classification map. (c) Classification Map.	53
Figure 5-3. Resulting classification maps after GA use with 60 generations and the entire dataset for the SVM training. (a) Synthetic RGB representation of the HS cube with the tumor area surrounded by a yellow line. (b) Reference classification map. (c) Classification Map.	54
Figure 5-4. Resulting classification maps after PSO use with 30 generations and the entire dataset for the SVM training. (a) Synthetic RGB representation of the HS cube with the tumor area surrounded by a yellow line. (b) Reference classification map. (c) Classification Map.	56

Figure 5-5. Resulting classification maps after PSO use with 60 generations and the entire dataset for the SVM training. (a) Synthetic RGB representation of the HS cube with the tumor area surrounded by a yellow line. (b) Reference classification map. (c) Classification Map.....	57
Figure 5-6. Reference results obtained with all bands and the reduced dataset for the SVM training. (a) Synthetic RGB representation of the HS cube with the tumor area surrounded by a yellow line. (b) Classification map. ...	58
Figure 5-7. Resulting classification maps after GA use with 60 generations and the reduced dataset for the SVM training. (a) Synthetic RGB representation of the HS cube with the tumor area surrounded by a yellow line. (b) Reference classification map. (c) Classification Map.....	59
Figure 5-8. Resulting classification maps after PSO use with 60 generations and the reduced dataset for the SVM training. (a) Synthetic RGB representation of the HS cube with the tumor area surrounded by a yellow line. (b) Reference classification map. (c) Classification Map.....	60
Figure 5-9. Boxplot diagram of the (a) overall accuracy and (b) sensitivity of the tumor class of all the evaluated techniques	62
Figure 5-10. Classifications maps of the test dataset. (a) Synthetic RGB images with a yellow line determining the area tumor. (b and c) Reference results with the entire and reduced dataset. (d and e) GA algorithm using 60 generations with entire and reduced dataset. (f and g) PSO algorithm using 60 generations with entire and reduced dataset.	63
Figure 5-11. Resulting classification maps after GA FoM and the reduced dataset for the SVM training. (a) Synthetic RGB representation of the HS cube with the tumor area surrounded by a yellow line. (b) Reference classification map. (c) Classification Map	65
Figure 5-12. Resulting classification maps after PSO FoM and the reduced dataset for the SVM training. (a) Synthetic RGB representation of the HS cube with the tumor area surrounded by a yellow line. (b) Reference classification map. (c) Classification Map	66
Figure 5-13. Resulting classification maps after GA FoM _{Penalized} and the reduced dataset for the SVM training. (a) Synthetic RGB representation of the HS cube with the tumor area surrounded by a yellow line. (b) Reference classification map. (c) Classification Map.....	67
Figure 5-14. Resulting classification maps after PSO FoM _{Penalized} and the reduced dataset for the SVM training. (a) Synthetic RGB representation of the HS cube with the tumor area surrounded by a yellow line. (b) Reference classification map. (c) Classification Map	68
Figure 5-15. Boxplot diagram of the overall accuracy (a) and sensitivity of the tumor class (b) of all FoM evaluated techniques.	69
Figure 5-16. Classifications maps of the test dataset. (a) Synthetic RGB images with a yellow line determining the area tumor. (b) OPF Reference. (c and d) OPF GA and PSO (e) OPF GA FoM. (f) OPF PSO FoM. (g) OPF GA FoM _{Penalized} . (h) OPF PSO FoM _{Penalized}	71
Figure 5-17. Classifications maps of the test dataset using the selected bands by the GA FoM technique.....	73
Figure 5-18. Classifications maps of the test dataset using the selected bands by the GA FoM _{Penalized} technique.	74
Figure 5-19. Classifications maps of the test dataset using the selected bands by the PSO FoM penalized technique.	76
Figure 5-20. Best cases classifications maps. (a) Synthetic RGB images with a yellow line determining the area tumor. (b) OPF Reference. (c and d) OPF GA FoM and FoM _{Penalized} and (e) OPF PSO FoM _{Penalized}	77
Figure 5-21. Resulting classification maps after ACO and the entire dataset for the SVM training. (a) Synthetic RGB representation of the HS cube with the tumor area surrounded by a yellow line. (b) Reference classification map. (c) Classification Map.	79
Figure 5-22. Resulting classification maps after ACO and the reduced dataset for the SVM training. (a) Synthetic RGB representation of the HS cube with the tumor area surrounded by a yellow line. (b) Reference classification map. (c) Classification Map	80
Figure 5-23. Classifications maps of the test dataset using the selected bands by the ACO algorithm.	82
Figure 5-24. Best case classification map. (a) Synthetic RGB images with a yellow line determining the area tumor. (b) OPF Reference. (c) OPF GA FoM _{Penalized} LI.	84
Figure 5-25. Normalized average signature of the classes and final selected bands.	85

List of Tables

Table 2-1. Classification results for selected wavelength combinations [29].	22
Table 3-1. RGB of hyperspectral dataset.	34
Table 3-2. Ground truth maps of hyperspectral dataset	34
Table 3-3. HELICoiD labelled pixel train dataset	35
Table 3-4. HELICoiD labelled pixel test dataset	35
Table 4-1. Experiments summary	48
Table 5-1. Reference results obtained with all bands and the entire dataset for the SVM training.	51
Table 5-2. GA 30 generations results obtained with all bands and the entire dataset for the SVM training.	52
Table 5-3. GA 60 generations results obtained with all bands and the entire dataset for the SVM training.	54
Table 5-4. PSO 30 generations results obtained with all bands and the entire dataset for the SVM training.	55
Table 5-5. PSO 60 generations results obtained with all bands and the entire dataset for the SVM training.	56
Table 5-6. Reference results obtained with all bands and the reduced dataset for the SVM training	58
Table 5-7. GA results obtained with all bands and the reduced dataset for the SVM training.	59
Table 5-8. PSO results obtained with all bands and the reduced dataset for the SVM training.	60
Table 5-9. OPF GA FoM results obtained with all bands and the reduced dataset for the SVM training.	64
Table 5-10. OPF PSO FoM results obtained with all bands and the reduced dataset for the SVM training.	65
Table 5-11. GA FoM _{Penalized} results obtained with all bands and the reduced dataset for the SVM training.	67
Table 5-12. PSO FoM _{Penalized} results obtained with all bands and the reduced dataset for the SVM training.	68
Table 5-13. Average and standard deviation of accuracy, sensitivity, specificity and MCC using GA FoM of all images.	72
Table 5-14. Average and standard deviation of accuracy, sensitivity, specificity and MCC using GA FoM _{Penalized} of all images.	74
Table 5-15. Average and standard deviation of accuracy. sensitivity. specificity and MCC using PSO FoM _{Penalized} Of all images.	75
Table 5-16. Best cases average and standard deviation of accuracy. sensitivity. specificity and MCC.	77
Table 5-17. Accuracy, sensitivity, specificity and MCC results using the entire dataset with ACO.	78
Table 5-18. Accuracy, sensitivity, specificity and MCC results using the reduced dataset with ACO.	80
Table 5-19. Average and standard deviation of accuracy, sensitivity, specificity and MCC using ACO.	81
Table 5-20. Accuracy, sensitivity, specificity and MCC results using OPF-GA-FoM _{Penalized} L1.	84
Table 5-21. Accuracy, sensitivity, specificity and MCC results using OPF-GA-FoM _{Penalized} L1.	85

List of Acronyms

Acronym	Meaning
ACO	Ant Colony Optimization
AI	Artificial Intelligent
ALO	Ant Lion optimizer
BFWA	Binary Firework Algorithm
BPF	Basic Processing Framework
FA	Factor Analysis
FWA	Firework Algorithm
GA	Genetic Algorithm
HSI	Hyperspectral Image
LOOCV	Leave-One-Out Cross-Validation
MCC	Matthews Correlation Coefficient
MDS	Multidimensional Scalar
OA	Overall Accuracy
OPF	Optimized Processing Framework
PCA	Principal Component Analysis
PSO	Particle Swarm Optimization
RMSEP	Root Mean Squared Error of Prediction
SAM	Spectral Angle Mapper
SPA	Successive Projection Algorithm
SVM	Support Vector Machine
UVE	Uninformative Viable Elimination
WSVM	Wavelet Support Vector Machine

Chapter 1: Introduction

1.1 Context

This Master Thesis is developed within the research line of hyperspectral imaging (HSI) acquisition and processing for medical applications that is currently carried out by the Division of Integrated Systems (DSI) of the University Institute for Applied Microelectronics (IUMA) of the University of Las Palmas de Gran Canaria (ULPGC), specifically in the field of intraoperative brain cancer diagnosis.

In addition, IUMA has been involved in projects financed by both public and private entities, in the field of processing HS images in different areas. Among these projects are:

- **HELICoiD Project (CNET-ICT-618080)**

This Master Thesis will use the HELICoiD project database. HellicoiD was a European collaboration project between four universities (ULPGC, *Imperial College of Science, Technology and Medicine of London*, Polytechnic University of Madrid, *Assosiation pour la Recherche et le Développement des Methodes et Processus Industriels de Paris - Armines*), three industrial partners (Medtronic Iberica SA, *General Equipment for Medical Imaging S.A.*, *Virtual Angle B.V.*) and two hospitals (Canary Foundation for Research and Health, *University Hospital of Southampton NHS Foundation Trust*), financed by the Executive Research Agency (REA) of the European Union.

The purpose of this project was to develop a demonstrator capable of differentiating between healthy and tumor tissue in real time during neurosurgery interventions by means of hyperspectral images, thus enabling real-time resection of tumor tissue to be confirmed in real time, avoiding excessive resection of adjacent healthy tissue and indeterminations due to displacement of brain mass.

The ITHaCA project is the continuation of the HELICoiD project, since it ended in December 2016.

- **ITHaCA Project (ProID2017010164)**

This Master Thesis is framed within the ITHaCA project (IndenTificación Hiperespectral de tumores CerebrAles), funded by the Canarian Agency for Research,

Innovation and the Information Society of the Canary Islands Government¹. This is a multidisciplinary project that integrates engineers, neurosurgeons and pathologists. Its main objective is to perform a real-time accurate differentiation and classification by using hyperspectral images of different types of brain tumors. This fundamental research project is promoted by the IUMA (University Institute of Applied Microelectronics) of the University of Las Palmas de Gran Canaria and FUNCANIS (Canarian Foundation for Health Research), the research management foundation of the University Hospital of Gran Canaria Doctor Negrín (HUGCDN).

1.2 Objectives

The main objective of this Master Thesis is to study and evaluate different band selection algorithms in order to identify the most relevant bands in HSI that allow an accurate delineation of brain tumors during surgical procedures. This relevant band identification will allow reducing the HS camera size as well as reducing the computational cost of processing the HS data. Thus, specific HS sensors for brain tumor detection could be developed. Specifically, the specific objectives that must be reached to achieve the main objective are the following ones:

- To study different band selection algorithms employed for HS images.
- To apply supervised classification techniques using HS cubes that have been reduced in bands as input data.
- To evaluate how each band selection algorithm affects the final classification result in terms of quantitative and qualitative evaluation.
- To determine the band selection technique that offers the best relationship between the accuracy of the results and the minimum number of bands employed.

1.3 Methodology

The methodology followed in this research work is tightly related with the objectives described before. This methodology can be summarized as follows.

1. To study the basic concepts about HS images related to dimensional reduction techniques.
2. To research the different optimization algorithms for the selection of bands to be used for HS images analysis.
3. To research the different evaluation metrics to be used for the experimental procedures. There are several types of evaluation metrics, so, after an exhaustive study, some of them were selected for the evaluation of the results.
4. To develop an algorithm to find the most suitable optimization method and identify the most relevant bands for this particular application.

¹ <https://ithaca.iuma.ulpgc.es/>

5. To analyze and evaluate the final results obtained.

1.4 Document organization

This document has been structured in six chapters that are organized as follow:

- Chapter 1: Introduction.** In the present chapter, the context and objectives that have led to the development of this Master Thesis are described. In addition, the structure of the document is presented.
- Chapter 2: State-of-the-art.** In this chapter, the necessary knowledge to develop this Master Thesis is explained. It makes a study of the previous works carried out where band selection techniques are used in HSI as well as the explanation of the algorithms employed in this work.
- Chapter 3: In-Vivo HS Human Brain Image Database.** This chapter describes the intraoperative HS acquisition system employed to acquire the in-vivo HS human brain database employed in this work. In addition, the procedure followed to intraoperatively capture the HS images during the surgical procedures is explained.
- Chapter 4: Methodology.** In this chapter, the different proposed processing methods for the identification of the most representative bands of the HS images are described.
- Chapter 5: Experimental results.** In this part of the document, the results obtained after processing the HS images, with the different methods explained in Chapter 4, are shown.
- Chapter 6: Conclusions and future lines.** This last chapter exposes the conclusions that have been drawn after analyzing in depth the results obtained. In addition, the on-going works are described.

Chapter 2: State-of-the-art

2.1 Introduction

In this Master Thesis, the use of optimization algorithms to reduce the dimensionality of hyperspectral (HS) images is proposed. This chapter describes the background knowledge necessary for the development of the work. Firstly, a brief introduction of Hyperspectral Imaging (HSI) is presented, due to this type of images will conform the database to be used. Secondly, two of the most-extended techniques that has been proposed in the literature to reduce the high dimensionality of these types of images will be explained. Besides, several studies where these techniques are applied in different HSI applications will be analyzed. Finally, the basic functioning of the three main optimization algorithms selected is explained: Genetic Algorithm (GA), Particle Swarm Optimization (PSO) and Ant Colony Optimization (ACO). These algorithms will be used in the development of the project in the last section.

2.2 Hyperspectral images

Hyperspectral imaging (HSI) is a technology that combines conventional imaging and spectroscopy to obtain simultaneously the spatial and the spectral information from an object [1]. HSI provides abundant information that covers hundreds of spectral bands for each image pixel [2]. Thanks to the sensors that HS cameras employ, hyperspectral (HS) images show the radiance of the materials within each pixel area, which have a large number of spectral wavelengths, exploiting the fact that all materials reflect, absorb or emit electromagnetic energy in certain wavelengths. Each pixel contains an almost continuous spectrum (radiance², reflectance³ or absorbance⁴), acting as a fingerprint (the *so-called* spectral signature) that can be used to characterize the chemical composition of that particular pixel. In other words, it can be used to identify the captured objects in a certain scene with high precision and quality.

² Measure of the amount of electromagnetic radiation leaving or arriving at a point on a surface.

³ Measure of the ability of a surface to reflect light or other electromagnetic radiation.

⁴ Measure of the light-absorbing ability of an object.

As a result of spatial and spectral sampling, HS image sensors produce a three-dimensional (3D) data structure with spatial and spectral components, called a HS cube. In Figure 2-1, it can be seen that the spectral signatures change when different objects are analyzed. For example, if all the pixels are extracted in the same spatial location and we represent their spectral values as a function of the wavelength, the result is the average spectrum of all the materials in the resolution cell. In this case, it can be observed in Figure 2-1 the spectral signatures of a brain tumor [3], [4].

This type of imaging technique was created for remote sensing applications, however, over the years its development and fields of application have been extended to other areas such as food quality [5], art conservation [6], archaeology [7], biomedicine [8], etc. In this project, HSI is used in the medical field, specifically as an aid tool for the detection of human brain tumors.

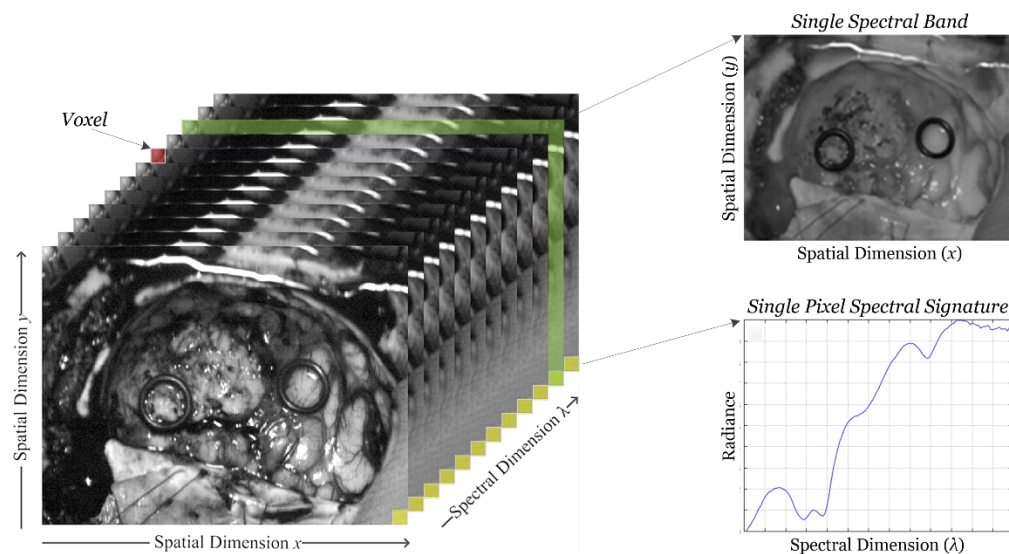


Figure 2-1. Structure of a hypercube and spectral signatures of a brain tumor [9].

2.3 Dimensional reduction

HS images are characterized by “the curse of dimensionality” [10] having a high dimensionality due to the rich amount of information they contain. However, this fact causes that the computing time required to process the data is extremely high and also, in some cases, the processed data contain redundant information. Thus, it is necessary to employ processing algorithms that reduce the dimensionality of the HS data without losing the relevant information.

This dimensional reduction process consists on the transformation of the data, characterized by their high dimensionality, into a significant representation of such data in a reduced size. Ideally, this low-dimensional representation should be composed by the minimum number of parameters necessary to take into account the fundamental characteristics of the data [11]. In consequence, there are two types of methods that allow this transformation: feature selection [12] and feature extraction [13]. In this Master Thesis, the main goal is to apply feature selection algorithms to reduce the

dimensionality of the HS human brain data for brain cancer identification. Although this same study is also valid for any type of HS images.

2.3.1 Feature extraction methods

Feature extraction algorithms are able to reduce, scale and rotate the original feature space of the HS data through a transformation matrix. This transformation optimizes a given criterion on the training data so, it can be formulated as a linear transformation which projects feature vectors on a transformed subspace defined by relevant directions [14]. Some of the algorithms that allow this type of transformation are *Principal Component Analysis (PCA)* [15], *Factor Analysis (FA)* [16], or *Multidimensional Scalar (MDS)* [17], among others.

2.3.2 Feature selection methods

The feature selection algorithms applied to the HSI, aim to find the optimal subset of these images, making all possible combinations that allows the image. This process reduces the dimensionality of the data by selecting the most discriminant bands of the dataset [14]. Some of the algorithms that allow carrying out this process are optimization algorithms such as the *Genetic Algorithm (GA)* [18], *Particle Swarm Algorithm (PS)* [19], *Ant Colony Optimization (ACO)* [20], etc.

2.4 Band selection methods for HSI

As commented in section 2.2, the use of HS images has increased considerably in different industrial and research areas. One of the main field of application is remote sensing [21], however, other applications such as military , agronomic [23], or medical [24], are gaining strength.

Because of this growth, it is becoming extremely necessary the reduction of the dimensionality of the HS images in order to provide cost-effective sensors for real-time execution applications. Thus, different algorithms are currently have been studied in the literature with the goal of making this reduction in the best possible way. In this section, some of the most relevant studies found in the literature are presented, where different techniques are analyzed in order to identify which wavelengths in the HS images provide more information for certain applications.

The most common applications where HS images have been used in combination with feature selection algorithms are in the food quality area. In [25], Yu *et al.* focus their research on detecting the amount of moisture found in soybeans using the spectral region over 400-1000 nm. This work performs a comparative study of the following algorithms: *Binary Firework Algorithm (BFWA)* [26], *Successive Projections Algorithm (SPA)* [27] and *Uninformative Variable Elimination Algorithm (UVE)* [28]. Figure 2-2 shows that the best result is obtained with the BFWA algorithm, since with four spectral bands (wavelengths), the Root Mean Squared Error of Prediction (RMSEP⁵) is lower than 6%.

⁵ Measure of the difference between predicted values and the actual values.

However, in the other cases, the RMSEP increases to 10% and 14% using the SPA and UVE algorithms, respectively. It is observed that if the number of bands increases, the RMSEP decreases, nevertheless, BFWA continues to give the best result with only four bands. However, the researchers decided to select 12 bands, to prevent the model to be unstable at some point. The 12 wavelengths selected were 457.95, 509.48, 567.44, 586.76, 612.52, 657.6, 696.24, 747.76, 773.52, 850.8, 908.76 and 934.52 nm.

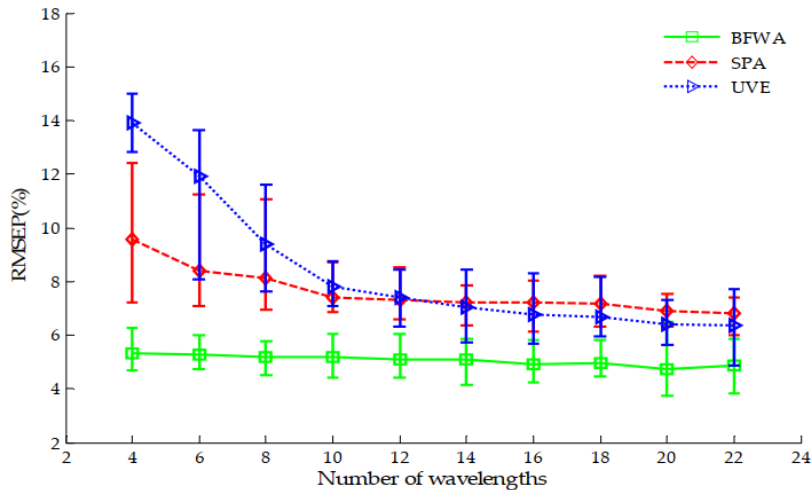


Figure 2-2. The RMSEP values obtained by SPA, UVE, and BFWA [25].

Another study performed by Nagasubramanian *et al.*, also focused on the food quality inspection through HSI, has the goal to detect the state of rot in soybeans [29]. In this case, instead of making a comparative with different algorithms, authors employed the *Genetic Algorithm* (GA) combined with the *Support Vector Machine* (SVM) classifier. The study concludes that the most suitable number of wavelengths for this application was 6 (from 240 spectral bands), which 3 of them were the RGB wavelengths (475.56 (B), 548.91 (G) and 652.14 (R) nm) and the other 3 selected by the GA, being 516.31, 720.05 and 915.64 nm. The results obtained after performing the combinations of selected wavelengths are shown in Table 2-1. The F1-Score⁶ and the overall classification accuracy obtained after using only the RGB wavelengths were 0.79 and 76.92%, respectively. However, when the 6 wavelengths selected by the classifier were used, the F1-Score and the overall classification accuracy were 0.97 and 97%, respectively, significantly improving the results.

Table 2-1. Classification results for selected wavelength combinations [29].

Band Combination	Confusion Matrix	Precision	Recall	F1-Score	Healthy Acc.** (%)	Infected Acc.** (%)	Overall Accuracy (%)
3 (RGB)	TP=17; FP=8 FN=1; TN=13	0.68	0.94	0.79	92.85	68.00	76.92
6	TP=18; FP=1 FN=0; TN=20	0.94	1.00	0.97	100.00	94.00	97.00

**Accuracy per class

⁶ Harmonic mean between precision and recall. Statistical measure to rate performance.

Other main area that uses HS images is remote sensing. In these applications, one of the main requirements is that the size of the data should not be high to avoid high delays in the transmission of the data. In this sense, there are several studies performed on how to efficiently reduce the dimensionality of the data. In the study performed by Wang *et al.*, a modified Ant Lion Optimization (ALO) and Wavelet Support Vector Machine (WSVM) was proposed [30]. The objective of this method is to select the lowest number of bands as accurately as possible. The ALO algorithm is combined with the WSVM to improve the stability of the classification result. To evaluate the algorithm, several public standardized databases are used, Botswana with 145 bands, KSC with 176 bands and Indian Pines with 185 bands (acquired by the NASA EO-1 satellite, Kennedy Space Center (KSC) and AVIRIS respectively). The range of these databases ranges from 0.4 to 2.5 μm . Figure 2-3, shows the precision change curve of each of the databases. It can be seen that, the precision when selecting more bands is stabilized. This fact can be observed when selecting the 125, 141 and 153 main bands for the Botswana, KSC and Indian Pines datasets. For the worst case, the accuracy is 85.3%, while in the rest it is higher than 93%.

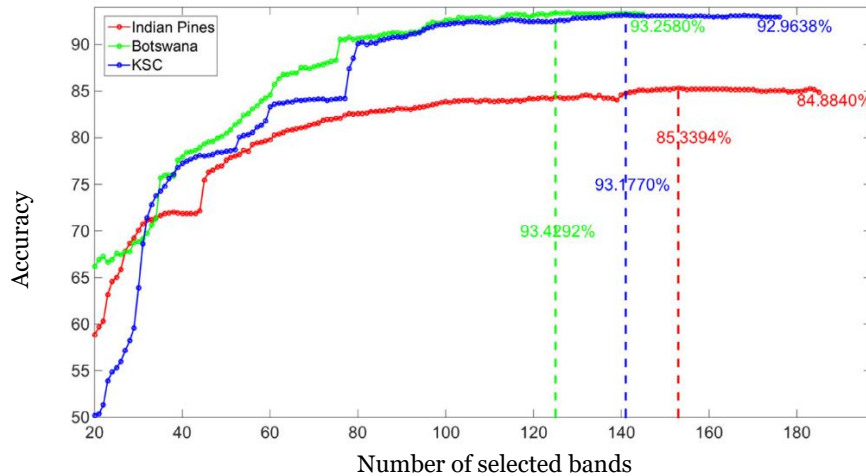


Figure 2-3. The change curve classification accuracy for 3 HSI datasets [30].

On the other hand, in the study performed by Yu *et al.*, also related with remote sensing, they used the GA algorithm combined with the K-Nearest Neighbor (KNN) algorithm for the selection of features, reducing the computation time and improving or maintaining the accuracy of the automatic classifiers [31]. As in the previous case, the researchers employed the same public HS images. The goal was to find the most relevant bands that provides the best classification results. Several experiments were performed. These consisted in reducing the number of bands while maintaining the classification error below 10%. The first experiment evaluates from the database the first 50 bands through GA with 100 generations. The next experiment is the same process with the first 100 bands. The third and last experiment was to repeat the same procedure with the first 150 bands and with all the bands of the database, respectively. Figure 2-4 shows on the Y-axis the number of selected bands reduced and the X-axis the number of generations performed to find the most significant bands. It can be seen that with the original HS cube, composed by 220 bands, the best result was obtained after performing 90 generations in the GA and a number of bands somewhat lower than 35. With 150 bands, after performing the generation 70, the number of optimized bands is maintained with a number of 15-16 bands. This result is repeated when evaluating only 50 bands after generation 50. However, with a database of 100 bands, upon reaching generation 78, the number of bands is reduced to less than 10.

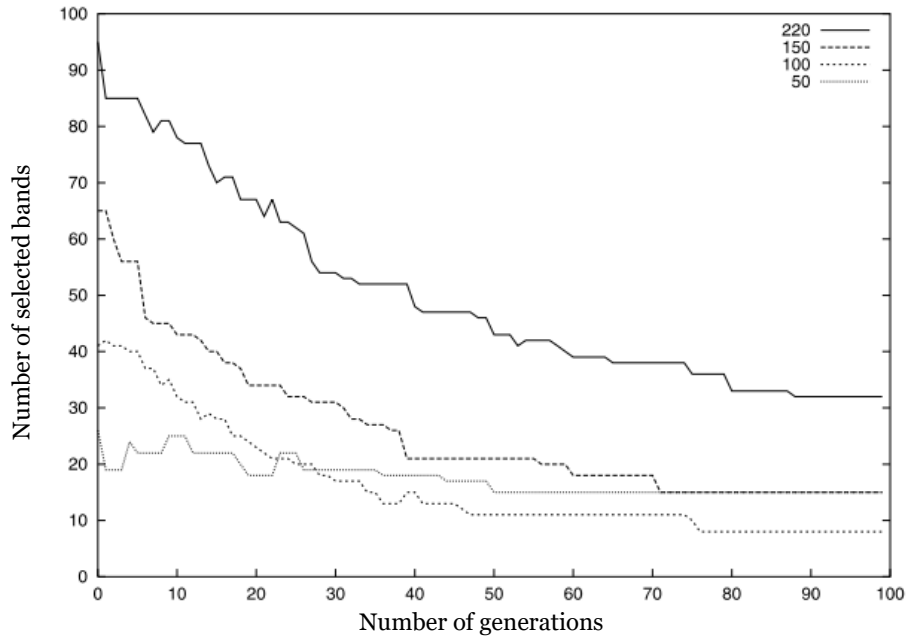


Figure 2-4. Number of selected bands versus number of generations for the GA selection on 50, 100, 150 and 220 bands [31].

2.5 Optimization algorithms

In this section, the different optimization algorithms used to carry out this Master thesis are explained. The optimization algorithms are aimed to find the best combination of elements from an initial set of available elements. Normally, these type of algorithms are focused on reaching the global minimum of the function to be analyzed. Next, the GA, PSO and ACO algorithms will be explained.

2.5.1 Genetic Algorithm

The *Genetic Algorithm* (GA) is an optimization algorithm that mimics the process of natural selection. GA tries to find the optimal solution (usually the global minimum) of the function to be studied. The main advantage of this algorithm is its great ability to work with a large number of variables [32], [33].

The objective of this algorithm is to optimize a series of parameters (genes) that will be then concatenated with each other, when necessary, those that provide the best results (chromosome). In order to find these most important values, it is necessary to generate populations in a random manner whose size is chosen by the user. This population allows to improve the performance of the algorithm [34]. Once these parameters are defined, the GA must perform the following steps:

- 1) **Initialization:** In this step, the selection of the population is performed in a random way.
- 2) **Evaluation:** The goal is to study the results obtained from the initial population (parents) and each of the descendant generations (children).
- 3) **Selection:** This point is responsible for keeping the best result obtained during the evaluation process.

- 4) **Recombination:** In this step, the combination of the different initial contributions (parents) for the creation of better solutions (children) is performed. This crossing is performed by dividing the populations in two (or more) parts and exchanging part of those populations with each other, in the way that is observed in the Figure 2-5.a.
- 5) **Mutation:** This technique is performed in the same way as in recombination step. However, instead of exchanging parts of the populations among themselves, a single value of each of the populations is modified, as shown in Figure 2-5.b.
- 6) **Replacement:** After performing the recombination and mutation, these generations (children) replace the initial populations (parents).

The steps 2 to 6 are repeated as many times as are necessary until the best solution is found [18].

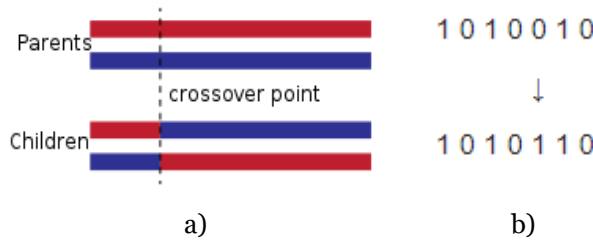


Figure 2-5. Recombination and mutation process.

2.5.2 Particle Swarm Optimization

The *Particle Swarm optimization* (PSO) algorithm is a stochastic technique that is based on the behavior of bee swarms. This algorithm highlights its effectiveness in multidimensional optimization problems [35]. This methodology is based on the survival of some living beings. In this case, the algorithm is inspired by the procedure carried out by bees to find the place with the major quantity of flowers. At first, the bees begin to move randomly and each bee remembers where they located the most flowers. In addition, the bee, somehow, knows where the rest of the bees have found more flowers, so that, with no prior knowledge about which place has the highest density of flowers, the bee chooses a place between those two points. However, the bee can find another area with more flowers between these two points, so it repeats the same process and instead of choosing one of the two points, choose a middle point. This process is repeated by each bee as many times as necessary until they find the area with the most quantity of flowers [36].

As well as the genetic algorithm, PSO is initialized with a random initial population. However, in this case, each possible solution, known as particle, has also assigned a random velocity [19]. Each particle updates and stores the best position found for far ($pbest$) and also stores and updates the best position of the rest of the swarm ($gbest$). To represent the velocity update, the algorithm uses the next equation:

$$v_i(t+1) = \alpha v_i + c_1 * rand * (pbest(t) - x_i(t)) + c_2 * rand * (gbest(t) - x_i(t)) \quad (2.1)$$

where v_i is the velocity vector, x_i is the position vector, α is the weight of the particle that controls the recognition of the place, c_1 and c_2 are the acceleration constants of the particles (usually take a value of 2 by default), and $rand$ is a random number between 0 and 1 [35].

Once the parameters that conform the algorithm are obtained, the swarm is generated by means of the following steps:

- 1) **Initialization:** This step initializes a random population with different positions and velocities.
- 2) **Selection:** In this step, each particle evaluates the best location found and the best position found by the rest of the swarm.
- 3) **Evaluation:** Here, a comparison of all the results and selection of the pbest is performed. The same process is applied to find the best gbest.
- 4) **Replacement:** In this last step, the new results replace the initial population and the process is repeated up to a maximum number of generations established by the user or until the solution converges [37].

2.5.3 Ant Colony Optimization

The 2.5.3 *Ant Colony Optimization* (ACO) algorithm is based on a metaheuristic procedure, which aims to obtain acceptable solutions in problems of combinatorial optimizations in a reasonable computational time.

As the name suggests, this algorithm is based on the composition of the ant colonies. The ants, when searching for food, separate and begin to make trips in a random way. Once an ant gathers food, while carrying the food to the nest, it expels pheromones along the way. Depending on the quality or quantity of the food found, the amount of pheromones will vary. On the other hand, the evaporation of the pheromones causes the pheromones to disappear, so that, if these routes are not reinforced, they end up disappearing. This process is repeated until you find the best possible route.[38], [39]. In Figure 2-6, an example of the selection process of the best path through a group of ants is presented. Figure 2-6.a shows the initial case, without pheromones in the environment, while Figure 2-6.b shows that the group is separated by choosing random paths to find the food. During the path, ants start to expel pheromones, as it can be seen Figure 2-6.c, and, then, the most ants return by the shortest route, increasing the amount of pheromones in the short path (Figure 2-6.d). Finally, after some time, the pheromones of the long path will evaporate [40].

Taking into account this selection process, the algorithm is characterized by having a main component, the pheromone model. This model is a parameterized probabilistic model, which consists of a vector of parameters that indicate the trajectory followed by pheromones. These values are updated until the minimum values of the problem are reached [38].

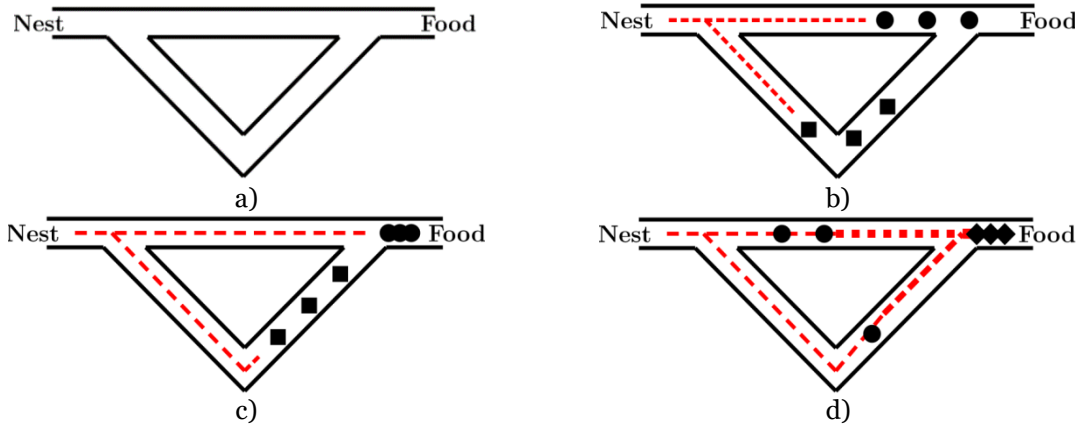


Figure 2-6. Simulation of the selection process of the ant colonies of the best route between the nest and the food [40].

2.6 Support Vector Machine Classifier

In this Master Thesis, apart from techniques of “band selection” techniques, the *Support Vector Machine* (SVM) classifier will be used throughout the study.

The Support Vector Machine classifier is a binary classification algorithm. Its objective is to find out the best hyperplane that allows to separate the different data with a maximum margin [41].

To perform the calculation of the hyperplane, it is necessary to have a dataset x_i where $x_i \in \mathbb{R}^d$ (d is the dimension of each sample), and labels associated with these data y_i where $y_i \in \mathbb{R}$ [42]. Each label provides information about the data x_i , if $y_i = 1$, the class is positive and if $y_i = -1$, the class is negative. According to the data input x_i , it can be written as follows:

$$\hat{y} = x_i \cdot w + b \quad (2-2)$$

Where \hat{y} is the predicted class for instance x_i , and the parameters w and b define the hyperplane which has the maximum margin as a characteristic ($w \in \mathbb{R}^d$) and ($b \in \mathbb{R}$). The values of these parameters are obtained through a training set, which is based on an ordered sequence of data and labels (x_i, y_i) [43]. In Figure 2-7 an example of a hyperplane found by SVM is presented.

For the development of this Master Thesis, it is necessary to use the SVM multiclass classifier. Since the SVM is a binary classifier, it is necessary to perform transformations for the identification of all classes. The most used method is the one-vs-one [44]. This method finds and generates linear hyperplanes ($k-1$) between different classes (k) [45].

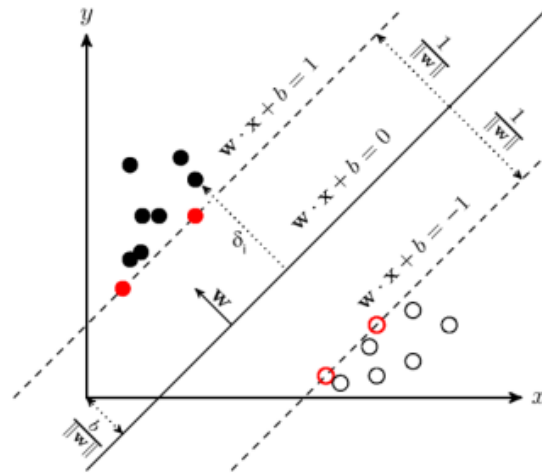


Figure 2-7. Support Vector Machine linear hyperplane between two classes [46].

2.7 Summary

In this chapter, a state of the art has been presented, where the purpose of HS images and their basic characteristics has been explained. On the other hand, taking into account that these images can exhibit redundant information, the main goal is to reduce its size without losing information by means of dimensional reduction techniques, specifically through the selection of features, which can lead in cheaper instrumentation for a given application. Several articles have been analyzed that make use of these types of procedures. Finally, three optimization algorithms were selected to identify which bands that conform the HS image are the most relevant ones.

Chapter 3: In-Vivo HS Human Brain Image Database

3.1 Introduction

This chapter will describe the database used during the realization of this Master Thesis. This database is composed by HS images of human brain tissue. This research work will aim to find the most relevant bands of the HS images by using this database.

In addition, a general description of the procedure carried out to obtain the HS images during the execution of the European HELICoiD project (from where the data were obtained) will be provided.

The HELICoiD project was a European collaborative project funded by the Executive Research Agency (REA), through the Future and Emerging Technologies program (FET-Open), within the framework of the 7th Framework Program of the European Union [47]. HELICoiD aimed to generate a demonstrator capable of differentiating between healthy tissue and tumor tissue in real-time during neurosurgical operations using HSI. During the development of the HELICoiD project, an intraoperative experimental system was developed [48], which provided to neurosurgeons in surgical-time a thematic map where the boundaries of the tumor were identified with the goal of performing an accurate resection of the tumor [49].

3.2 Intraoperative HS Acquisition System

To carry out the process of acquisition of the database, it was decided to use a custom intraoperative HS acquisition system [47], [48], [50]. This system was developed within the HELICoiD research project.

Figure 3-1, shows the platform of the intraoperative HS acquisition system used during a neurosurgery operation at the Doctor Negrín University Hospital in Las Palmas, Gran Canaria, Spain [51]. This system consists of two *pushbroom* cameras: a Hyperspec® VNIR A-Series camera (Figure 3-1.a), which covers the spectral range from 400 to 1000 nm. It has a dispersion of 0.74 nm and a spectral resolution of 2-3 nm (with a 25 µm slit), and is capable of capturing 826 spectral bands and 1004 spatial pixels, and a Hyperspec® NIR 100 / U camera (Figure 3-1.b), which covers the spectral range from

900 to 1700 nm. It has a dispersion per pixel of 4.8 nm and a resolution of 5 nm (with a 25 μm slit), 172 spectral channels and 320 spatial pixels [48].

On the other hand, this system also has a light source (Figure 3-1.c and Figure 3-1.e), composed of a QTH lamp (Quartz-Tungsten-Halogen) connected to a cold light emitter through a fiber optic cable (Figure 3-1.d). This lighting system prevents the high temperatures emitted by the light source from reaching the surface of the brain. Finally, the cameras are fixed to a scanning platform (Figure 3-1.f and Figure 3-1.g), covering a useful area of 230 mm. This displacement is necessary since the cameras, being pushbroom type, only capture a single spatial dimension.

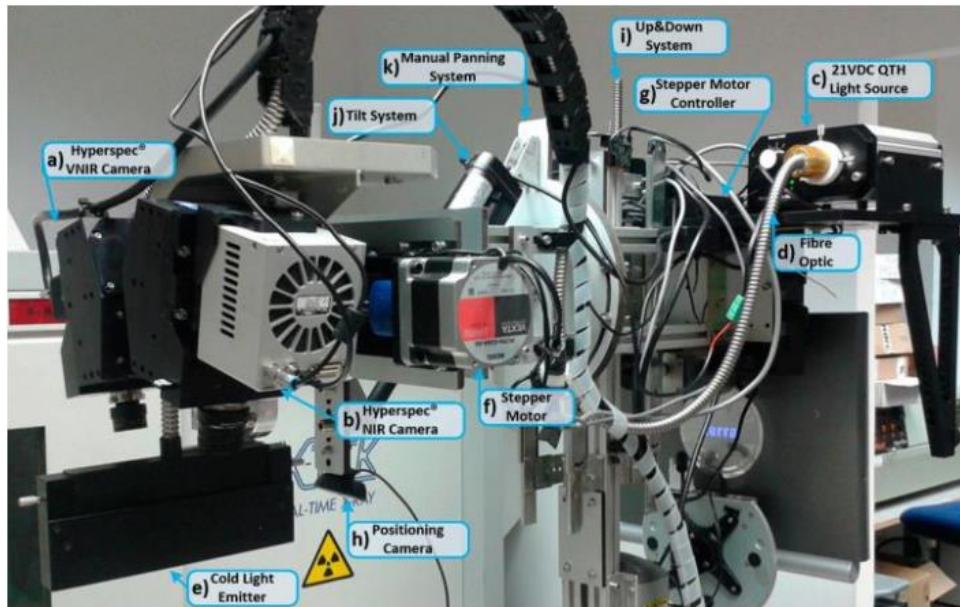


Figure 3-1. HELICoiD demonstrator acquisition platform. (a, b) VNIR and NIR HS cameras mounted on the scanning platform; (c-e) Light source QTH connected to the fiber optic system for the transmission of light to obtain a light emission on the scanning platform; (f, g) stepper motor coupled to the shaft and connected to the stepper motor controller to perform the linear movement of the cameras; (h) Positioning of the camera used to identify the position of the field of vision of the cameras (FOV); (i) The Up & Down system used to focus the HS cameras; (j) and (k) Manual pan and tilt systems used to correctly orient the scanning platform [48].

3.3 Acquisition of HS images during surgery

The process to follow for a correct labeling of the samples can be observed in Figure 3-2 where the procedure to be followed is shown. The following subsections explain these steps [52]. First, Figure 3-2.a shows the acquisition system for intraoperative HS imaging that is used in the Hospital Doctor Negrín during a neurosurgery operation. Second, Figure 3-2.b and Figure 3-2.c show the spectral range with which the camera works, from 400 to 1000 nm, capturing 826 spectral bands and 1004 pixels per line. Third, Figure 3-2.d shows the RGB image with the two markers indicating which tissue is tumor (left) and which healthy tissue (right), and Figure 3-2.e and Figure 3-2.f show the histopathological analysis of surface tissue samples that are within the markers. Fourth, the Figure 3-2.g shows golden map where some pixels have been labelled and checked by the surgeon. In this case, there are four classes: the healthy tissue being the green color (class 1), the tumoral tissue with the red color (class 2), the hypervascularized

represented with the blue color (class 3) and the background with the black color (class 4). Finally, Figure 3-2.h shows the mean and standard deviation of the spectral signatures of the four classes that make up the image.

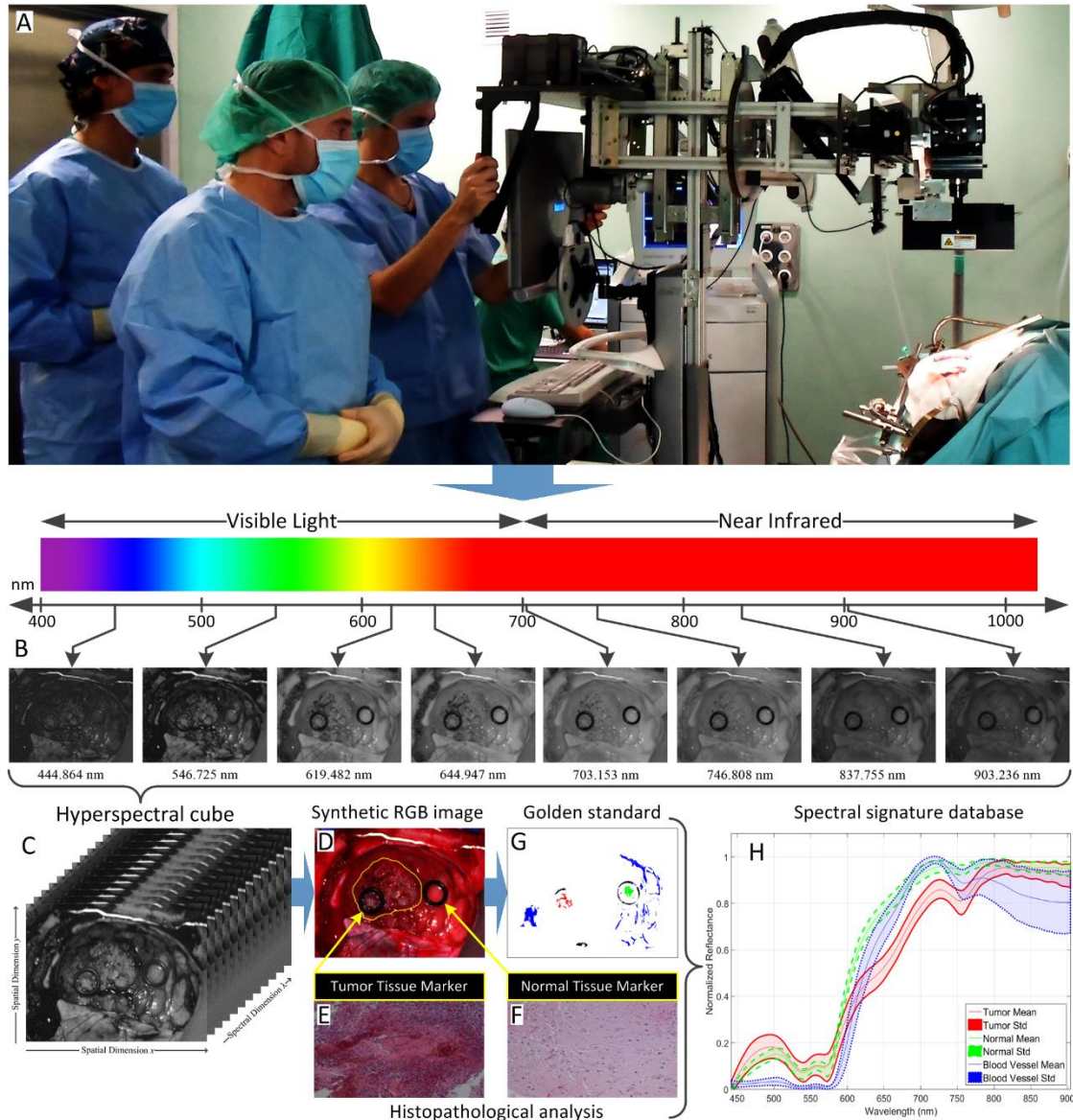


Figure 3-2. Data acquisition and labelling procedure [51].

3.3.1 Patient preparation

Time before performing the operation, the patient is given an image guide stereotactic⁷ (IGS), composed of the MRI (*Magnetic Resonance Imaging*) and the CT (*Computed Tomography*) scan. Once the previous procedure has been carried out, the patient is generally subjected to general anesthesia, the skull is exposed and drilled by

⁷ System that allows finding the exact position of a particular part inside the body before an operation.

means of a high-speed drill. Next, a craniotomy is inserted into the hole created and a craniotomy⁸ with a craniotome is performed. Once a part of the skull has been removed, the last step is to extract the dura⁹ to be able to start operating.

3.3.2 Hyperspectral image capture

The capture process is performed between the extraction of the dura mater and the rupture of the arachnoid and pia mater. If the tumor is located on the surface, a series of sterilized markers, usually two, are placed according to the surgeon's instructions for the correct identification between healthy tissue and tumor. The exact location of the markers is by means of the IGS system pointer to identify the location of the markers on the brain. This pointer allows knowing the position of the markers with respect to an MRI or CT previously performed. Figure 3-3 and Figure 3-4 show the structure of the three meninges and the use of the IGS system pointer, respectively.

Using the HELICoiD demonstrator, several images were captured with and without markers. Thanks to the markers, the process of labeling the pixels becomes easier, since this labeling can be compared with the results of histopathological analysis, because a biopsy is performed inside said markers that will be analyzed by pathology [51].

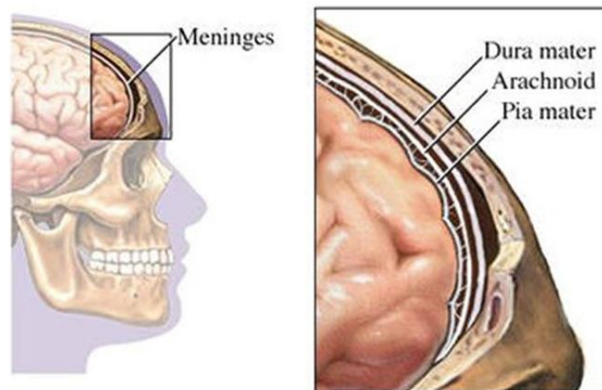


Figure 3-3. Meninges' structure [53]



Figure 3-4. IGS system pointer. (a) IGS system pointer over the tumor surface. (b) IGS system screen snapshot with the IGS system pointer coordinates [51]

⁸ Surgical removal of part of the skull to expose the brain.

⁹ Fibrous membrane forming the outer of the central nervous system.

3.3.3 Tissue resection

Once the HS image is obtained, the neurosurgeons begin with the resection of the tumor tissue. First, a biopsy is performed and sent to pathology in a container labeled as HELICoiD. These samples will be the gold reference for performing a proper labeling and then the correct development of the algorithm. When possible, a new HS image is captured during the resection process.

3.3.4 Expert evaluation

Samples sent to pathology are subjected to two standard processes: first, the sample is fixed with formalin and then stained by means of hematoxylin¹⁰-eosin¹¹ and any other dye if necessary to establish a correct diagnosis. The pathologists are the only ones that can determine the type of tissue that the sample belongs to. These results are classified as tumor or normal (healthy) tissue. In addition, the tumor samples are divided in the type of tumor and its corresponding malignancy degree [54].

3.3.5 Samples labelling

After the pathological result confirmation is obtained, the labeling process is carried out by using a semi-automatic labeling tool developed to this end based on the Spectral Angle Mapper (SAM) algorithm [51]. These pixels are labeled into four classes related with a certain color: healthy tissue (class 1 - green), tumor tissue (class 2 - red), hypervascularized tissue (class 3 - blue) and background (class 4 - black).

3.3.6 Complete HS database

The final HS database employed in this Master Thesis is composed by 26 HS cubes belonging to 16 different patients, obtained at the University Hospital Doctor Negrín of Las Palmas de Gran Canaria. This database consists of Glioblastoma primary brain tumors.

This database was divided into two sets, one part for training and another for testing. However, due to the experiments performed were done using a leave-one-patient-out methodology (that will be explained in Chapter 4:), the remaining test HS images are also included in the training database. The selection of the test database was made taking into account that in these images some pixels with the four classes to be predicted are labelled

Table 3-1 and Table 3-2 show the RGB images and the gold reference of the test group, respectively. Table 3-3 and Table 3-4 show the number of pixels labeled from the training and test datasets, respectively.

¹⁰ Acid coloring matter obtained from the Wood of a tree.

¹¹ Any of a class of rose-colored stains or dyes, all being bromine derivatives of fluorescein.

Table 3-1. RGB of hyperspectral dataset

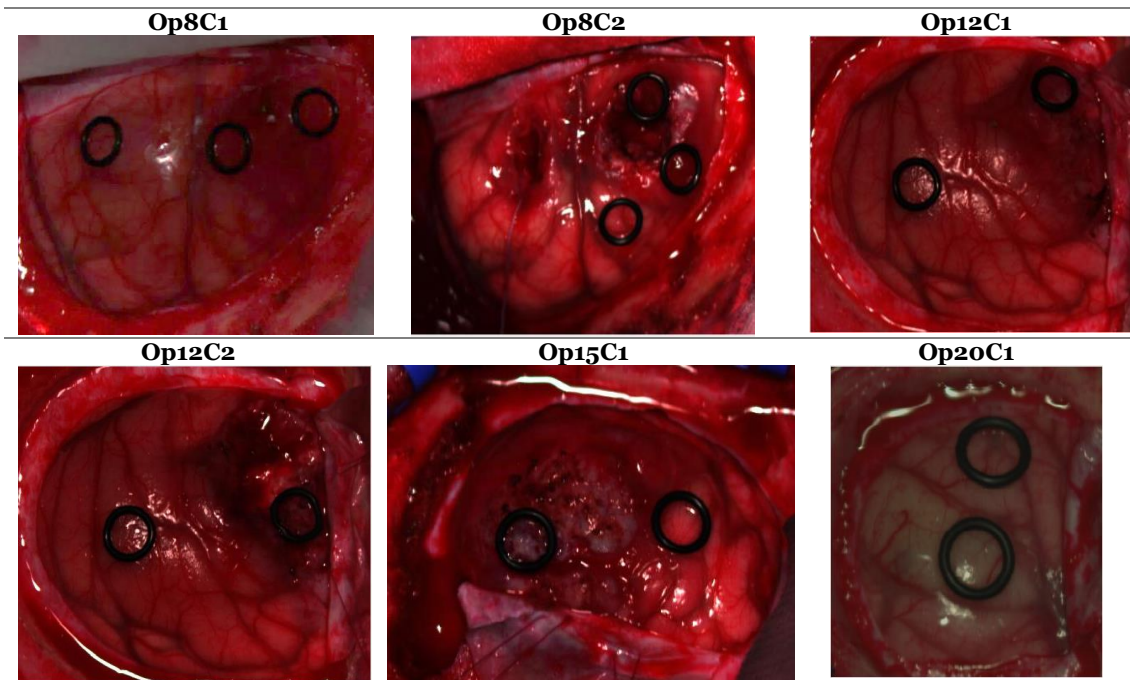


Table 3-2. Ground truth maps of hyperspectral dataset

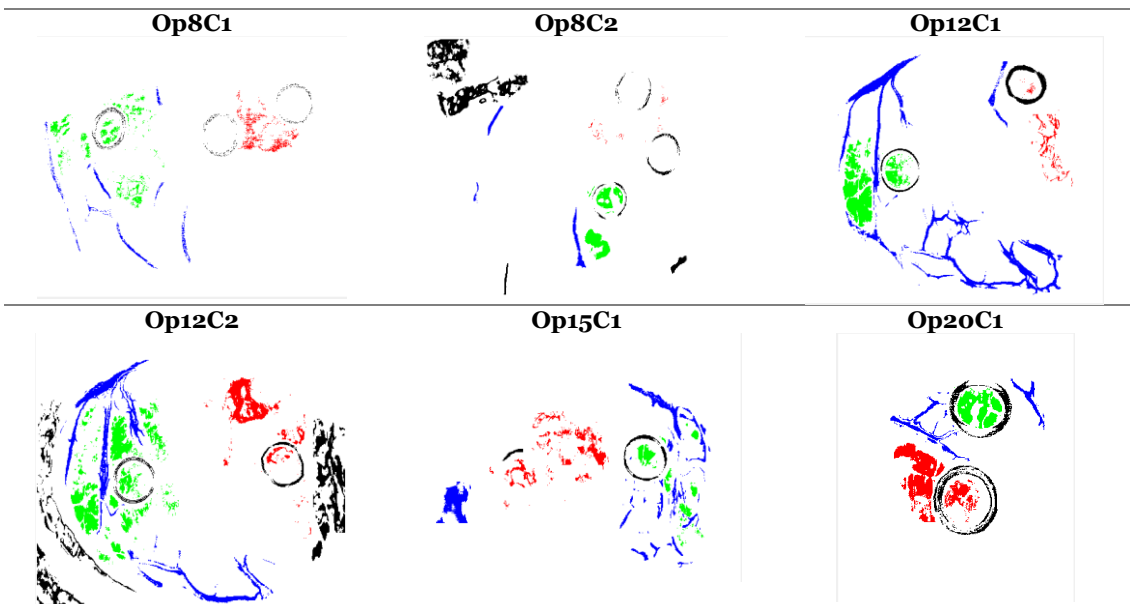


Table 3-3. HELICoiD labelled pixel train dataset

Patient ID	Image ID	Size (width x height x bands)	#Labeled Pixels			
			Normal	Tumor	Hypervascularized	Background
4	2	389 x 345 x 128	4.681	0	686	1.746
5	1	483 x 488 x 128	5.937	0	1.709	18.960
7	1	582 x 400 x 128	7.449	0	1.033	0
8	1	460 x 549 x 128	2.225	964	1.204	550
	2	480 x 553 x 128	1.895	92	834	6.997
10	3	371 x 461 x 128	10.303	0	2.230	3.275
12	1	443 x 497 x 128	4.365	820	8.495	1.306
	2	445 x 498 x 128	6.413	3.115	5.407	7.200
13	1	298 x 253 x 128	1.735	0	82	455
14	1	317 x 244 x 128	0	0	1	1.715
15	1	376 x 494 x 128	1.176	1.936	3.924	454
16	1	335 x 323 x 128	3.944	0	185	9.723
	2	335 x 326 x 128	345	0	0	2.546
	3	315 x 321 x 128	566	0	192	1.343
	4	383 x 297 x 128	1.110	64	970	705
	5	414 x 292 x 128	2.591	0	377	4.292
17	1	441 x 399 x 128	1.240	57	39	2.171
18	1	479 x 462 x 128	13.196	0	451	9.552
	2	510 x 434 x 128	4.614	0	919	5.427
19	1	601 x 535 x 128	6.437	0	1.267	1.743
20	1	378 x 330 x 128	1.541	3.439	1.370	2.180
21	1	452 x 334 x 128	3.165	0	720	4.406
	2	448 x 324 x 128	2.112	0	391	1.518
	5	433 x 340 x 128	832	0	1.423	1.088
22	1	597 x 527 x 128	2.803	0	936	3.436
	2	611 x 527 x 128	8.100	0	563	0
16	26		98.775	10.487	35.408	92.788
Total:			237.458			

Table 3-4. HELICoiD labelled pixel test dataset

Patient ID	Image ID	Size (width x height x bands)	#Labeled Pixels			
			Normal	Tumor	Hypervascularized	Background
8	1	460 x 549 x 128	2.225	964	1.204	550
	2	480 x 553 x 128	1.895	92	834	6.997
12	1	443 x 497 x 128	4.365	820	8.495	1.306
	2	445 x 498 x 128	6.413	3.115	5.407	7.200
15	1	376 x 494 x 128	1.176	1.936	3.924	454
20	1	378 x 330 x 128	1.541	3.439	1.370	2.180
4	6		17.615	10.366	21.234	18.687
Total:			67.902			

3.4 Summary

This chapter has explained the procedure necessary for a correct acquisition of HS brain tissue images during surgical operations that were carried out to obtain the database employed in this work. The database is divided in two sets, one set to train (Table 3-3) and another to test (Table 3-4). The training set consists of 26 *in-vivo* images of the brain surface of 16 patients. In the case of the test folder, it is composed by 6 captures of 6 patients. In each of the images, under the supervision of surgeons, it has been made the process of labeling of some of the pixels that compose the HS images. This labeling process is divided into four classes: normal tissue, tumor tissue, hypervascularized and background. In Table 3-3 and Table 3-4, the number of pixels labeled in each of the classes is observed for all the HS images that compose the training and test sets. It is observed that the training set is composed of more than 200,000 labeled pixels, while the test set is composed of nearly 68,000 labeled pixels.

Chapter 4: Methodology

4.1 Introduction

This section explains the different approaches proposed for the selection of the most representative bands in this work.

First, a general methodology is proposed in order to evaluate the classification with the bands selected by the GA and PSO algorithms. Once the results obtained have been evaluated, some drawbacks were found, so some modifications were proposed to solve these problems. One of the main drawbacks of the proposed structure was the excessive computation time per image. In addition, our dataset is unbalanced in terms of classes. An excessive number of labeled pixels for the training of the supervised classifier can produce misclassifications between the different classes in the dataset. As a solution, it was decided to develop an algorithm based on the unsupervised k -means algorithm for obtaining a reduced and balanced labeled dataset. With this algorithm, the training database is processed, reducing its size containing the most relevant information and balancing the classes (having the same number of labelled pixels in each class). In this way, it was possible to significantly reduce the computation time, and also to solve the problem of the unbalance of the labeled pixels between the classes.

Once the training dataset was reduced using k -means and verified, it was integrated into the initial general structure, generating a new framework. This new framework was evaluated with the same objective: the selection of the most representative bands with the GA and PSO algorithms. Then, once both procedures were evaluated, it was necessary to compare them with some reference results that allowed verifying if such procedures really improved the classification results. Therefore, the next step was to evaluate the use of all the bands with the entire and reduced labelled dataset.

Next, after analyzing the results obtained, it was decided to study another optimization algorithm based on the ant colony methodology (ACO algorithm). This algorithm was studied independently because its internal structure is quite different from the other two optimization algorithms.

Finally, the results obtained were analyzed with the same evaluation metrics: overall accuracy, sensitivity, specificity, custom Figures of Merit (FoM), Matthews Correlation Coefficient (MCC) and classification maps.

4.2 Proposed processing frameworks

In this section, we carefully explain the initial methodology that was followed during the development of this Master Thesis to find the most relevant bands of the HS images in order to provide an accurate classification of brain tumors. In general, all the proposed processing frameworks are composed by four main steps: relevant bands selection, supervised classifier training, supervised classification prediction and results evaluation (Figure 4-1).

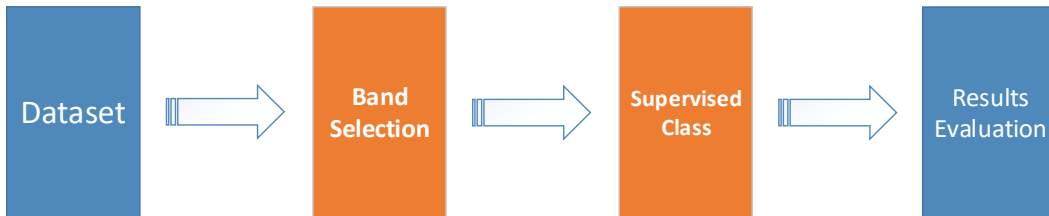


Figure 4-1. Flow diagram of the general process to select the best bands.

For the development and evaluation of the proposed processing frameworks, it was required the use of the labeled dataset presented in Chapter 3:. However, due to the quantity of execution iterations that has to be performed in each experiment for each proposed algorithm for the training of the supervised classifier, a specific approach to train the classifier using a reduced labeled dataset is proposed (Section 4.2.3).

The supervised classifier chosen to develop the model is the SVM algorithm. This algorithm has been already employed in several works to classify the in-vivo human brain HS image database employed in this study [55]. In this Master Thesis, no other classifiers have been employed since the main focus of this work was to study the different optimization algorithms. This classifier has been selected because, after an exhaustive analysis of different studies, where several optimization algorithms were evaluated, the classifier with the best results was the SVM algorithm [56]–[59]. For this project, the LIBSVM [60] public library was used for the implementation of the SVM algorithm.

4.2.1 Evaluation metrics

The evaluation metrics are used to evaluate the performance of an algorithm, in our case, the quality of the classification is evaluated with a determined number of selected bands used as input of a classifier. Many of these metrics tend to generate somewhat deceptive results, so it is necessary to evaluate the results with different methods. In addition, for all the experiments performed in this work, a *cross-validation* methodology was followed. In the next sections, each of the evaluation metrics used in this work are explained in detail.

4.2.1.1 Leave-One-Patient-Out Cross-Validation

Cross-validation is a statistical method of evaluation and comparison of learning algorithms. This method divides the data into two segments: one used to train a model and the other used to validate the model. The process that uses cross-validation is as follows: in each iteration, the algorithm uses $n - 1$ data folds to learn one or more models, and then the learned models are asked to make predictions about the data in the validation fold. The performance of each learning algorithm in each iteration is tracked using a certain evaluation metric [61].

There are several techniques to be used within the cross-validation: holdout, k-fold and leave-one-out. In this work we employed the leave-one-out methodology to evaluate the results.

The Leave-One-Out Cross-Validation (LOOCV) is a statistical estimation technique that is currently applied in machine learning and bioinformatics. This technique involves the partition of the original data set into n subsets of equal size. The model is trained n times (n is the number of instances), using each subset in turn as a test set, and the remaining subsets as the training set, as it can be seen in Figure 4-2. The general accuracy can be obtained by averaging the precision values calculated in each subset [62].

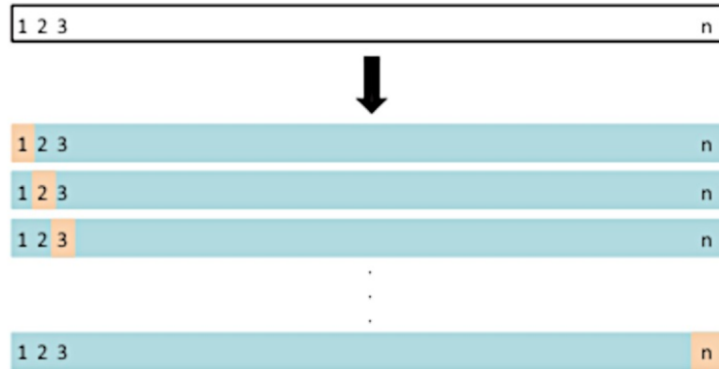


Figure 4-2. Leave-One-Out Cross-Validation method [63].

4.2.1.2 Overall Accuracy, Sensitivity and Specificity

To clearly explain the functioning of the sensitivity and specificity evaluation metrics, our case study is used as an example to determine if a certain pixel in an HS image represents cancer or not. For this purpose, it is necessary to previously introduce the following terms: true positive (TP), the pixel is cancer and the test is positive; false positive (FP), the pixel is not cancer and the test is positive; true negative (TN), the pixel is not cancer and the test is negative; and false negative (FN), the pixel is cancer but the test is negative [64].

4.2.1.2.1 Overall Accuracy

The Overall Accuracy (OA) indicates, in this example, the general detection of pixels with or without cancer. This metric shows how many pixels with and without cancer could be identified correctly [65]. Equation 4.1 shows the procedure to perform the calculation of the overall accuracy.

In addition to the standard OA, another metric has been proposed for the identification of the best results obtained with the optimization algorithms but taking into account also the number of selected bands. This $OA_{penalized}$ is based on the OA presented in Equation 4.1 but including a penalty in the case that a high number of bands is used. Equation 4.2 presents the mathematical expression to compute this $OA_{penalized}$, where λ is the number of bands selected by the algorithm and λ_{max} is the total number of bands in the original dataset.

OA has a value range between 0 to 1, where 0 represents a completely wrong prediction and 1 indicates a completely correct prediction. Otherwise, $OA_{penalized}$ has the same range value, but 1 represents a completely wrong prediction and 0 indicates a

completely correct prediction, due to the objective of the algorithms is to find the global minimum.

$$OA = \frac{TP + TN}{TP + FP + TN + FN} \quad (4.1)$$

$$OA_{penalized} = 1 - \frac{OA}{1 + \frac{\lambda}{\lambda_{max}}} \quad (4.2)$$

4.2.1.2.2 Sensitivity

Sensitivity represents, in this example, the correct percentage of identification of pixels with cancer. Equation 4.3 shows the necessary procedure to calculate the sensitivity of a model [66]. This metric ranges between values of 0%-100%, where 0% indicates that no pixels with cancer have been identified and 100% that all pixels with cancer have been correctly identified.

$$Sensitivity = \frac{TP}{TP + FN} \quad (4.3)$$

4.2.1.2.3 Specificity

Specificity represents, in this example, the correct percentage of identification of pixels without cancer. Equation 4.4 shows the necessary procedure to calculate the specificity of a model [66]. This metric ranges between values of 0%-100%, where 0% indicates that no pixels without cancer have been identified and 100% that all pixels without cancer have been correctly identified.

$$Specificity = \frac{TN}{TN + FP} \quad (4.4)$$

4.2.1.3 Matthews Correlation Coefficient (MCC)

The Matthews correlation coefficient (MCC) is mainly used to analyze classifiers that work with unbalanced data [67]. This metric indicates the correlation coefficient between the observed and the predicted values. MCC has a value range between -1 to 1, where -1 represents a completely wrong prediction and 1 indicates a completely correct prediction. Equation 4.5 shows the procedure necessary to calculate the MCC metric [68].

$$MCC = \frac{TP \times TN - FP \times FN}{\sqrt{(TP + FP)(TP + FN)(TN + FP)(TN + FN)}} \quad (4.5)$$

4.2.1.4 FoM for balanced accuracy per class

The specific FoM employed to obtain the most relevant bands with the optimization algorithms in the OPF has the goal of finding the most balanced accuracy results for each class, as observed in Equation 4.5, where n is the number of classes, i and j are the indices of the classes that are being calculated. The mathematical expression of the $ACC_{perClass}$ in a multiclass classification is obtained by dividing the total number of successful results

(TP) for a particular class by the total population of this class ($TP + FN$). This expression is equal to the sensitivity of a certain class in a multiclass classification problem. Equation 4.6 shows the mathematical expression of the $ACC_{perClass}$.

In addition to the previously presented FoM, another metric has been proposed for the identification of the best results obtained with the optimization algorithms but taking into account also the number of selected bands. This $FoM_{penalized}$ is based on the FoM presented in Equation 4.7 but including a penalty in the case that a high number of bands is used. Equation 4.8 presents the mathematical expression to compute this $FoM_{penalization}$, where λ is the number of bands selected by the algorithm and λ_{max} is the total number of bands in the original dataset.

FoM has a value range between 0 to 1, where 0 represents a completely wrong prediction and 1 indicates a completely correct prediction. Otherwise, $FoM_{penalized}$ has the same range value, but 1 represents a completely wrong prediction and 0 indicates a completely correct prediction, due to the objective of the algorithms is to find the global minimum.

$$FoM = \frac{1}{2} \cdot \left(\sum_{\substack{i,j \\ i < j}}^n \frac{ACC_i + ACC_j}{|ACC_i - ACC_j| + 1} \right) \cdot \binom{n}{2}^{-1} \quad (4.6)$$

$$ACC_{perClass} = \frac{TP}{TP + FN} \quad (4.7)$$

$$FoM_{penalized} = 1 - \frac{FoM}{1 + \frac{\lambda}{\lambda_{max}}} \quad (4.8)$$

4.2.1.5 Classification Map

This evaluation metric allows to visually identify where each of the different classes are located. This metric is employed to visually evaluate the classification results obtained when the entire HS cube is processed, including labeled and non-labeled pixels. After performing the classification of the HS cube, a certain color is assigned to each class. This process allows mainly evaluating the results obtained in the prediction of non-labeled pixels.

In our case, the colors that are represented in the classification map are the following: the green color was assigned to the first class (healthy tissue); the red color was assigned to the second class (tumor tissue); the blue color was assigned to the third class (hypervascularized tissue); the black color was assigned to the fourth class (background).

Figure 4-3 shows an example of a RGB image transformed to the classification map.

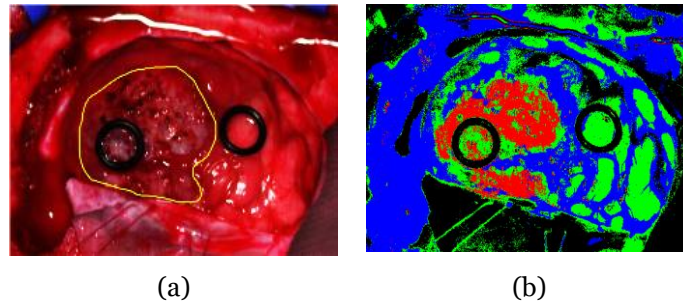


Figure 4-3. Brain tumor (a) synthetic RGB and (b) classification map.

4.2.1.6 GA and PSO number of generations rule

The optimization algorithms GA and PSO perform a determined number of generations that is calculated in the following way: $100 * numberOfVariables$. In this case, we have 128 variables, so we had to perform 12,800 generations. In our case, the average time at the time of making a generation was about 4 hours. Very long time to calculate 12800 generations per image. Therefore, it was decided in the beginning to carry out 30 generations. However, taking into account the obtained results, by using only 30 generations, was decided to increase the number of generations due to in some cases the results did not converge.

Figure 4-4 shows the evaluation of the GA generation, where it is clearly observed that with 30 generations it does not converge, and when the generations double, the values of the generations come to converge. As can be seen, when 30 generations are evaluated, the best $OA_{penalized}$ is 0.492, and with 60, it is 0.47. As the difference is not remarkable, it is decided to evaluate both generations.

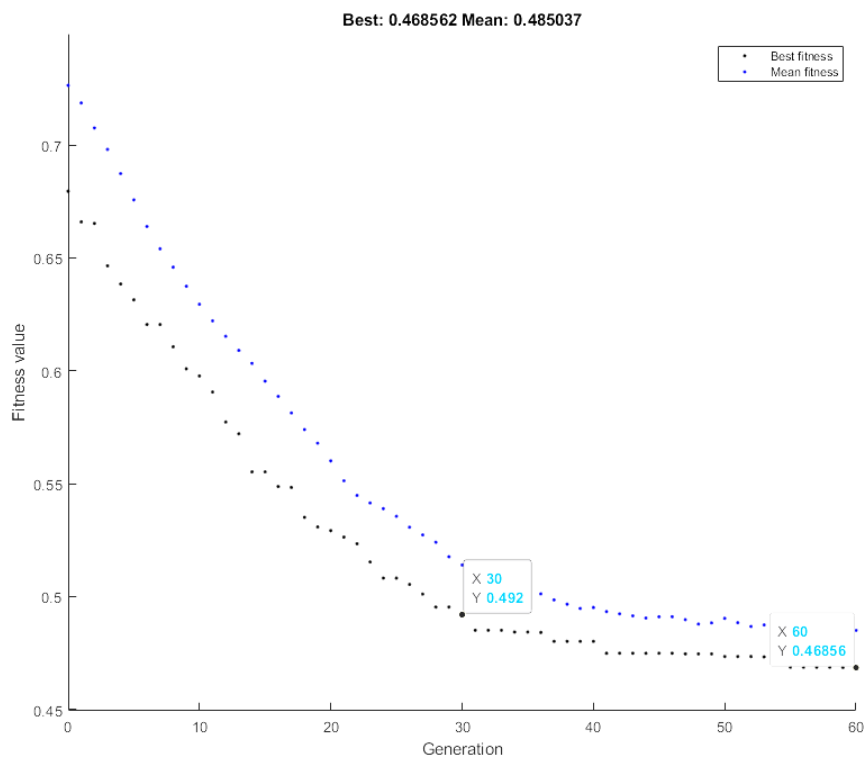


Figure 4-4. Graphic of the genetic algorithm generation.

4.2.2 Basic processing framework (BPF) with GA and PSO

The first proposed processing framework has the goal to evaluate the results obtained with the band selection algorithm (GA and PSO) when employing the entire labeled dataset for the training of the SVM classifier.

Figure 4-5 shows the flow diagram of this method, where the database is divided in two performing a leave-one-patient-out cross-validation. In this method, the labeled data of one patient is employed to test the algorithm and the remaining data from the other patients is used to train and generate the classification model. The detailed procedure is as follows. First, the training data are employed in the optimization algorithm, where the initial bands, to be used for the classification, are randomly selected. After this band selection procedure, a classification model is generated and evaluated with the test dataset, obtaining a classification result that is evaluated using the $OA_{penalized}$ metric. The value of this metric is stored and then, the procedure is iteratively executed using other bands selected by the optimization algorithm. The algorithm is executed until performs all possible combinations, returning the best metric, or when after a high number of iterations, the metric remains constant. Once the algorithm finishes the execution, it returns the best metric and the identification of the optimal bands to obtain this metric. At the end, the previously presented procedure is performed for each test HS image following the leave-one-patient-out cross-validation methodology.

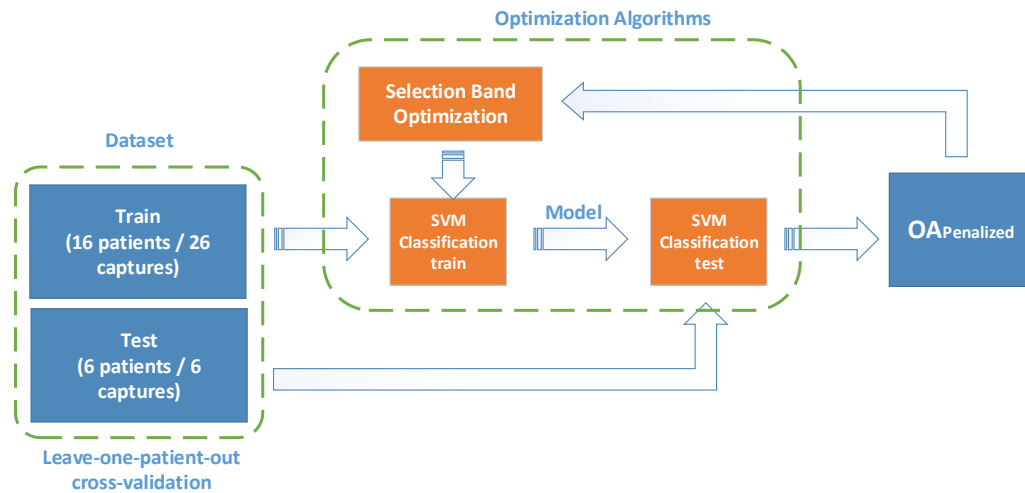


Figure 4-5. Flow diagram of the BPF for the identification of the most representative bands for the GA and PSO algorithms.

4.2.3 Optimized processing framework (OPF) with GA and PSO

After performing some experiments with the BPF, it was observed that the execution time was very high, reaching in some cases around four hours for execute only one generation in the GA or PSO.

Taking into account that the number of generations performed was done per test image, it was necessary to find some techniques that allowed reducing the execution time. Another problem was using all the pixels that compose the hyperspectral image as the labeled samples were unbalanced. This was due to the fact that, in the training base, there are patients who did not have a brain tumor, significantly reducing the number of

samples labeled of the tumor class with respect to the rest of the classes. This difference in level can be seen in Table 3-3.

In order to solve these problems, it was decided to use only 4,000 pixels (1,000 pixels per class) for training the SVM classifier, thus balancing all classes and dramatically reducing the size of the training database (from ~200,000 to 4,000 pixels). This procedure was done through a methodology based on the *K-means* clustering algorithm [69]. This algorithm aims to find and group K groups of data (called *clusters*) by means of the evaluation of a similarity metric among the samples. Therefore, similar elements (in our case spectral signatures from the pixels of the HS image) will be grouped in the same cluster.

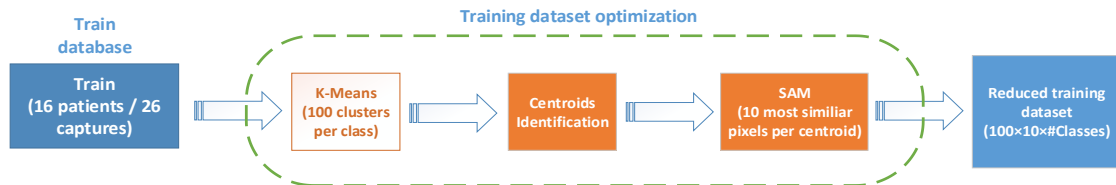


Figure 4-6. Flow diagram of the training dataset optimization algorithm.

Following the steps observed in Figure 4-6, the training dataset optimization algorithm has the goal of reducing the training dataset in order to eliminate redundant information. First, through the K-means algorithm, 100 clusters are identified for each class group (4 classes in our case). Then, the centroids of each cluster are employed as a reference pixel to compute the Spectral Angle Mapper (SAM) algorithm in order to detect the most similar pixels to the centroid of each cluster. In our case, the 10 most similar pixels were selected for each centroid. SAM algorithm measures the spectral similarity between two spectra. In this case, the spectrum is obtained as a vector in an n -dimensional space, where n is the number of bands. This algorithm allows to determine how similar the spectra are to each other by calculating the angle formed by the two spectra [70].

Finally, after the execution of the training dataset reduction algorithm, the reduced training dataset composed by 1,000 pixels per class (4,000 pixels in total) is obtained. This dataset contains the most important information available in the training dataset that will be used to perform the experiments dramatically reducing the execution time of the algorithms.

In Figure 4-7, it can be observed the modification performed to include the training dataset optimization algorithm in the complete procedure for band selection.

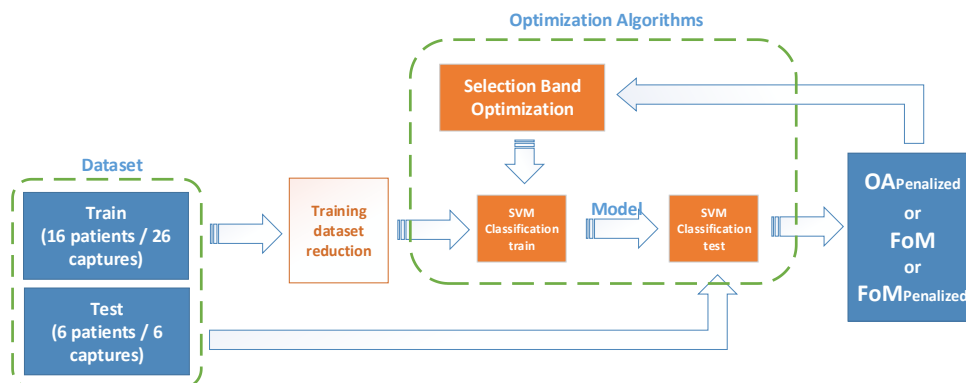


Figure 4-7. Flow diagram of the OPF for the identification of the most representative bands for the GA and PSO algorithms using the reduced training dataset.

4.2.4 Reference results and evaluation methodology for the BPF

As explained before, in the proposed methodology two different optimization algorithms were used: *Genetic Algorithm* (GA) and *Particle Swarm Optimization* (PSO). Before analyzing the results obtained with each of the algorithms in the BPF, the performance of the SVM classifier was evaluated employing the HS dataset without removing any band (Figure 4-8). These results will be employed as a reference results for the comparison of the results employing the band selection algorithms and also to find out if there really are improvements in tumor detection using a smaller number of bands. The evaluation metrics used were **overall accuracy**, **sensitivity**, **specificity** and **MCC** for the quantitative evaluation and **the classification map** obtained after processing the entire HS cube of the test image for the qualitative evaluation.

Once the initial results were obtained, the optimization algorithms were executed in the BPF and the optimal selected bands for each test image were identified. Then, the evaluation metrics were computed. The procedure is the same as the one shown in Figure 4-8.a. However, when the database is loaded, the bands to be analyzed are directly selected, as it can be seen in Figure 4-8.b.

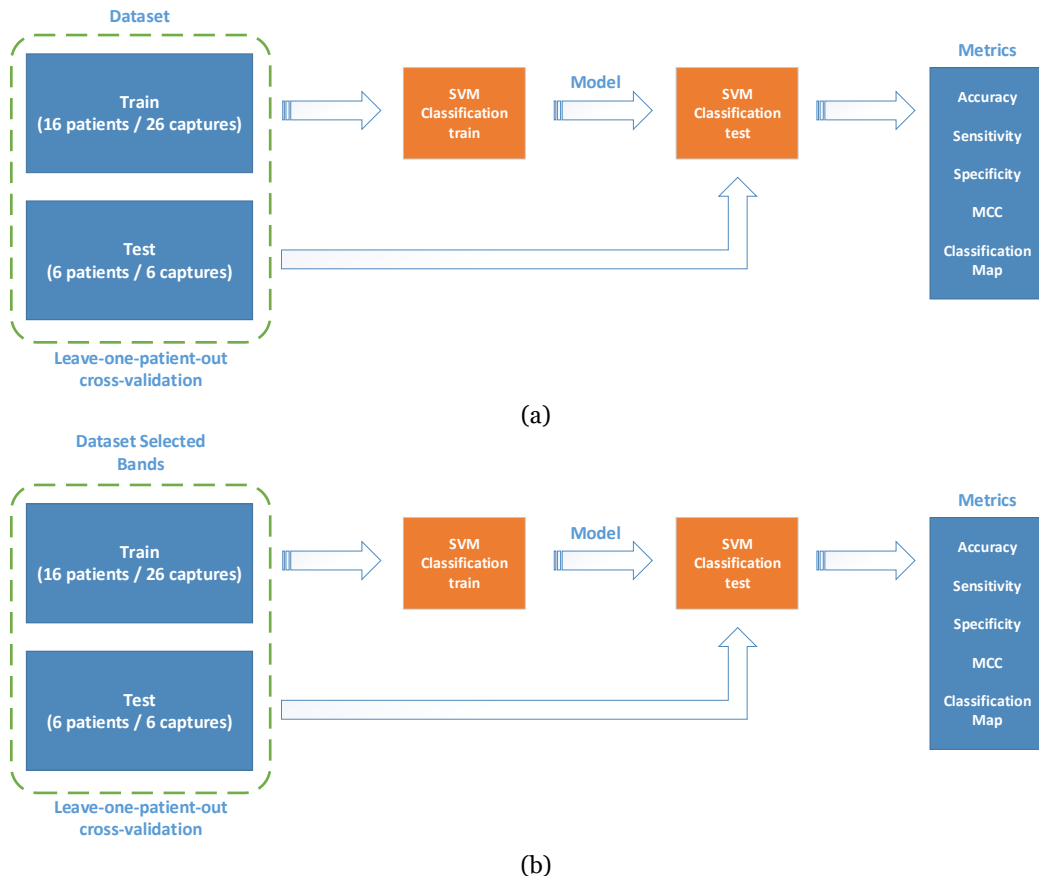


Figure 4-8. Flow diagram of the evaluation metrics computation with the (a) entire labelled dataset and (b) with the selected bands.

4.2.5 Reference results and evaluation methodology for the OPF

For the generation of the reference results and the evaluation of the results obtained with the OPF, the same methodology as the one presented in the previous section was carried out. In the following figure, Figure 4-9, the flow diagrams are shown where the integration of the database reduction step is included.

Once completed, the first two cases of study, the results obtained were analyzed. Therefore, the best cases are re-evaluated by making a series of changes in the FoM. This change consisted in returning in the output a balanced FoM between all the classes within the SVM classifier, with and without penalty of the use of the number of bands.

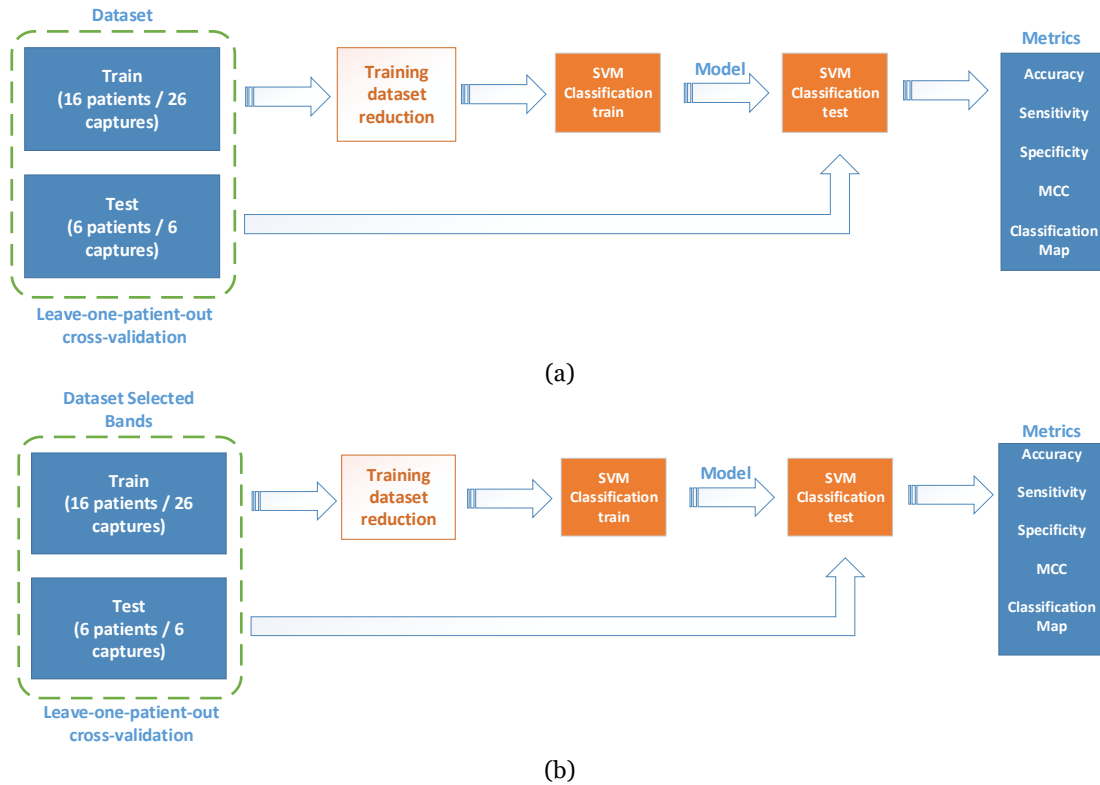


Figure 4-9. Flow diagram of the evaluation metrics computation with (a) all bands (reference results) and (b) selected bands using the reduced labeled dataset.

4.2.6 Band selection using the ACO algorithm

Finally, the ACO algorithm was analyzed. This algorithm was evaluated with the database with the entire and reduced labeled database as was done with the other optimization algorithms. Figure 4-10 shows the flow diagrams, where the band selection process and the evaluation process of these bands is respectively performed.

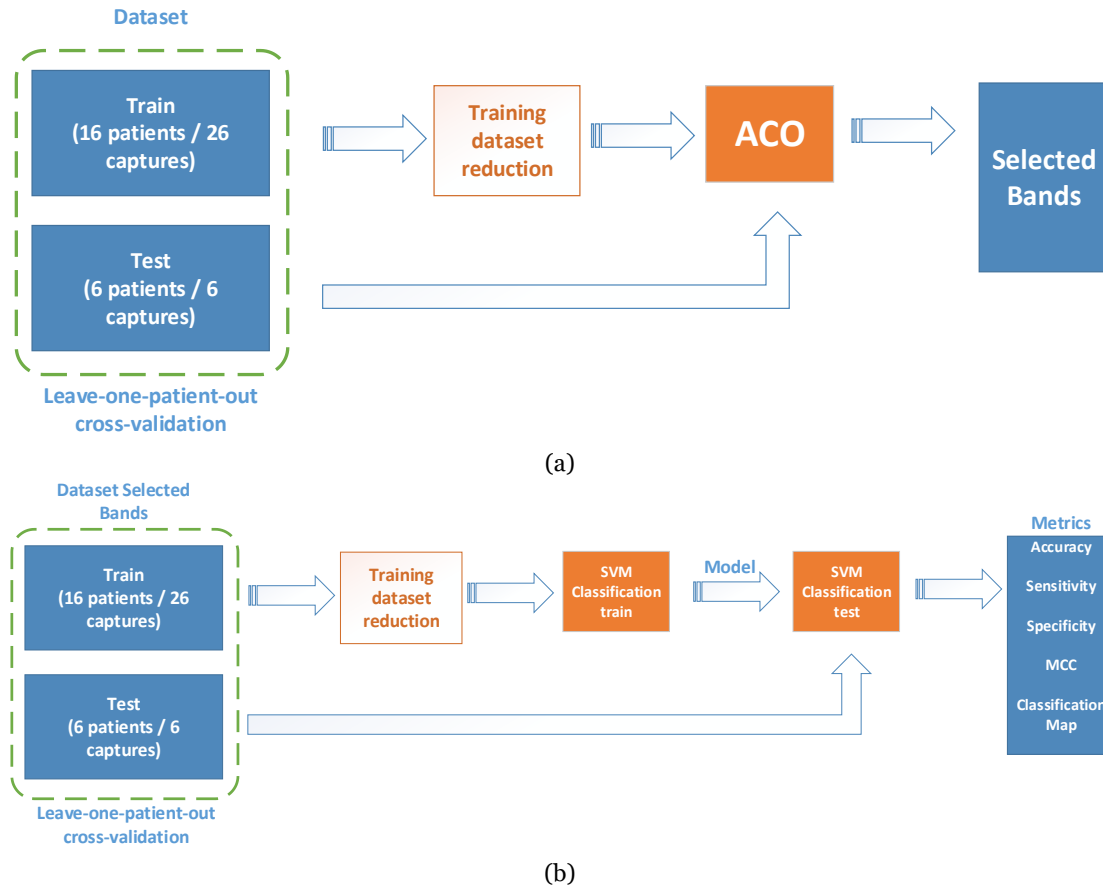


Figure 4-10. Flow diagram of the (a) band selection process with the ACO algorithm and the (b) evaluation metrics computation with the selected bands.

4.2.7 Evaluation of test database with the same bands

After obtaining and evaluating each of the combinations performed in the experiments, the four best cases obtained were selected for the following evaluation. In this case, all the images from the test database were evaluated using the same selected bands to generate and evaluate the classification model. This process is divided into a series of sub-levels.

- **First level:** all the bands that have been selected for each one of the test images were used to generate and evaluate the results.
- **Second level:** the bands that have been repeated in at least two test images were used to generate and evaluate the results.
- **Third level:** the bands that have been repeated in at least three test images were used to generate and evaluate the results.
- **Fourth level:** the bands that have been repeated in at least four test images were used to generate and evaluate the results.
- **Fifth level:** the bands that have been repeated in at least five test images were used to generate and evaluate the results.
- **Sixth level:** the bands that have been repeated in the six test images available in the test database were used to generate and evaluate the results.

4.3 Summary

In this chapter, the methodology followed throughout this Master Thesis to perform the experiments and evaluate the results has been described. Firstly, the band selection process using the entire and the reduced labeled dataset for the GA and PSO algorithms has been shown. Then, the evaluation process of the selected bands using the entire and the reduced labeled dataset has been presented. Finally, the developed approach to select the most representative bands by means of the ACO algorithm has been described. On the other hand, each one of the evaluation metrics used for the analysis of the results were detailed.

Table 4-1 summarizes all the experiments carried out to evaluate the different optimization algorithms with the entire and the reduced labeled dataset. First, all bands are evaluated with the complete and reduced database. Then, by means of the GA and PSO algorithms, the most representative bands are identified conditioned by the $OA_{penalized}$, both for the complete dataset and for the reduced one. After observing the results, for the best cases the same procedure is repeated but conditioned by FoM and $FoM_{penalized}$. Finally, the most important bands are calculated independently by using the ACO algorithm, both for the complete database and for the reduced database.

After comparing the results with the reference ones, it is observed that, for some cases, there are improvements when using a certain number of bands. However, each HS test image had different bands, so it was decided to evaluate the test images with the same bands obtained in the best cases. This procedure was divided into different coincidence levels. Initially, the patients were evaluated with all of the bands that were selected by the algorithm. Then, they were evaluated with all the bands that were found to be repeated in at least two patients, and so on.

Table 4-1. Experiments summary

Processing Framework Type	Reference	GA (#Generations)	PSO (#Generations)	ACO (#Iterations)
BPF	All Bands	30 ($OA_{penalized}$)	30 ($OA_{penalized}$)	600
		60 ($OA_{penalized}$)	60 ($OA_{penalized}$)	
OPF	All Bands	60 ($OA_{penalized}$)	60 ($OA_{penalized}$)	600
		60 (FoM)	60 (FoM)	
		60 ($FoM_{penalized}$)	60 ($FoM_{penalized}$)	

Chapter 5: Experimental results

5.1 Introduction

In this section, the results obtained with each optimization algorithm and its different variations are presented. Optimization algorithms try to find the best result of $OA_{\text{Penalized}}$ and FoM metrics, performing combinations at the time of selecting the bands. These experiments will be divided into the following structure:

1. Evaluation of the optimal bands for each test image obtained with the GA and PSO algorithms using the BPF (entire dataset) and the $OA_{\text{Penalized}}$ metric.
2. Evaluation of the optimal bands for each test image obtained with the GA and PSO algorithms using the OPF (reduced dataset) and the $OA_{\text{Penalized}}$ metric.
3. Evaluation of the optimal bands for each test image obtained with the GA and PSO algorithms evaluated with the designed FoM. This process is analyzed with the best cases obtained in the previous steps.
4. Evaluation of the optimal bands for the complete test image database using the OPF. This study is carried out with the best case obtained in the previous step.
5. Evaluation of the ACO algorithm for the band selection using the BPF and OPF methods.

For each case, these results were evaluated using the following evaluation metrics: OA, sensitivity, specificity, MCC and the classification map. These metrics were already explained in Chapter 4.2.1.

The first evaluation metric, in this case OA, is based on analyzing the correct prediction of reality. It is a global average of the results obtained for all the classes to be analyzed. The second evaluation metric, sensitivity, is responsible for indicating the percentage of success of the true positives for each of the classes. The third evaluation metric, specificity, otherwise the sensitivity, is responsible for indicating the percentage of true negatives for each of the classes. The fourth evaluation metric, Matthews Correlation Coefficient (MCC), has the same purpose as the second metric (sensitivity); however, this metric takes into account the differences in the size of the classes. Finally, the classification map is responsible for presenting the qualitative results, visualizing the RGB image when the entire HS test image is classified. The map is represented in four colors (green, red, blue and black) that are related to the four classes employed in the labeling process. The green color corresponds to class 1 and indicates healthy tissue, the red color corresponds to class 2 and indicates the tumor tissue, the blue color

corresponds to class 3 and indicates the hypervascularized tissue and finally, the black color corresponds to class 4 and indicates the background.

As discussed in Chapter 3, the test database consists of six HS images that belong to 4 different patients. A leave-one-patient-out cross-validation methodology was followed in order to obtain the classification results.

5.2 Band selection evaluation using BPF

In this section, the reference results obtained using all bands (128) and the results obtained after the evaluation of the most representative bands selected by the GA and PSO optimization algorithms, employing the $OA_{\text{Penalized}}$ metric to obtain the optimized results, are presented.

5.2.1 Reference results

The six HS images were evaluated with the 128 bands that compose the HS cubes for performing a comparison with the band selection algorithm results. The purpose of this is to find out if there are improvements using only a certain number of bands.

Table 5-1 shows the OA, sensitivity, specificity and MCC results obtained processing the HS test images with all the bands using the SVM algorithm. Observing the results, some of the most important aspects to highlight are the **OA**, which is around 79%, a relatively good result considering that no transformation was made. However, in the **sensitivity** results, the class with the worst result is the tumor class, where only 28% of pixels were detected correctly, being a very low result. This mainly occurs due to the unbalancing of the classes in the SVM training dataset. Regarding to the **specificity**, its percentage of success by classes is high, reaching in some cases 100%. Finally, if the **MCC** metric is observed, the success rate of the tumor class increases slightly (34%) because it takes into account the different sizes of the classes.

The qualitative results obtained with this reference method are shown in Figure 5-1, where the synthetic RGB images of each test image, with the tumor area surrounded by a yellow line, and the **classification maps** are presented. Looking at these results, only the *Op15C1* image clearly visualizes the area where the brain tumor is located. As for the other images, in some cases, such as *Op12C1* and *Op12C2*, some tumor is visualized in a specific area, providing some idea of where the tumor is located. *Op20C1* image shows no tumor and the rest of the images have some tumor pixels scattered in several different areas of the classification map.

Table 5-1. Reference results obtained with all bands and the entire dataset for the SVM training.

Patient ID	OA	Sensitivity				Specificity				MCC			
		NT	TT	HT	BG	NT	TT	HT	BG	NT	TT	HT	BG
Op8C1	58.2%	67.9%	15.5%	60.9%	100%	80.4%	89.7%	80.2%	72.8%	48.4%	7.1%	40.6%	53.8%
Op8C2	95.1%	96.6%	34.1%	98.5%	95.4%	96.1%	99.1%	99.8%	97.3%	89.1%	33.6%	98.0%	90.8%
Op12C1	93.3%	99.4%	46.8%	93.5%	99.5%	92.3%	100.0%	97.6%	99.8%	87.6%	67.1%	90.6%	98.6%
Op12C2	79.3%	97.2%	4.0%	98.2%	79.9%	86.7%	99.8%	82.6%	98.5%	79.1%	15.2%	73.5%	81.6%
Op15C1	88.3%	99.7%	67.6%	93.6%	98.0%	86.7%	100.0%	100.0%	99.4%	70.7%	77.8%	93.2%	95.9%
Op20C1	58.4%	97.2%	0.2%	79.8%	99.7%	49.8%	100.0%	99.8%	95.9%	37.7%	3.2%	85.8%	95.3%
AVG	78.8%	93.0%	28.0%	87.4%	95.4%	82.0%	98.1%	93.3%	93.9%	68.8%	34.0%	80.3%	86.0%

*NT: Normal Tissue; TT: Tumor Tissue; HT: Hypervascularized Tissue; BG: Background.

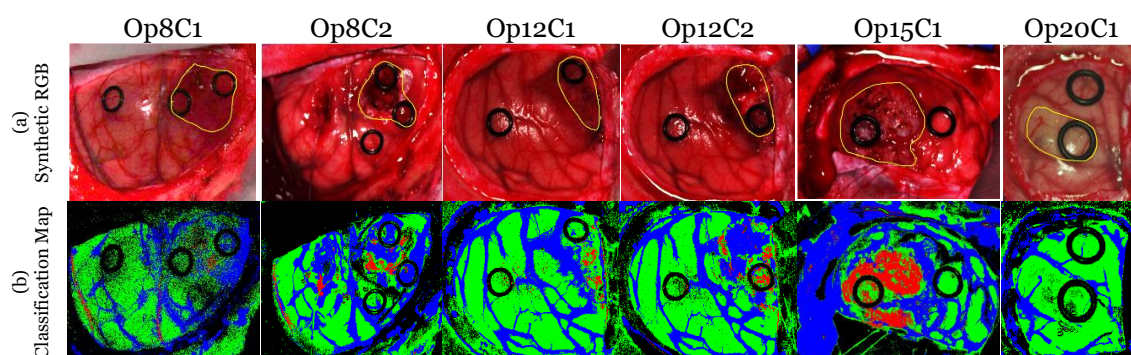


Figure 5-1. Reference results obtained with all bands and the entire dataset for the SVM training. (a) Synthetic RGB representation of the HS cube with the tumor area surrounded by a yellow line. (b) Classification map.

5.2.2 Genetic Algorithm evaluation

At the time to analyze the genetic algorithm, this algorithm was executed twice, with 30 and 60 generations. This is due to the fact that with 30 generations the global minimum was not found. Therefore, it was decided to double the number of generations in order to guarantee the identification of the global minimum and compare the results obtained with both number of generations. In this case, the results are observed after the evaluation of the optimal bands determined for each test image.

5.2.2.1 Genetic Algorithm evaluation using 30 generations

Once the genetic algorithm is generated, it shows which bands were selected for each image. Using these optimal selected bands, the evaluation metrics were computed using the SVM algorithm. Table 5-2 illustrates the results obtained with these bands after their evaluation.

Table 5-2. GA 30 generations results obtained with all bands and the entire dataset for the SVM training.

Patient ID	OA	Sensitivity				Specificity				MCC			
		NT	TT	HT	BG	NT	TT	HT	BG	NT	TT	HT	BG
Op8C1	65.8%	77.4%	44.7%	49.1%	100.0%	77.9%	87.1%	91.4%	82.7%	55.3%	34.1%	45.7%	64.6%
Op8C2	93.3%	97.1%	7.3%	97.2%	93.2%	94.2%	98.5%	100.0%	97.7%	85.7%	5.2%	98.3%	87.9%
Op12C1	90.5%	98.3%	42.2%	89.5%	99.3%	88.4%	99.9%	98.3%	99.4%	81.5%	62.5%	87.0%	97.2%
Op12C2	67.5%	97.6%	8.5%	95.4%	47.0%	65.5%	99.9%	81.7%	98.7%	57.8%	25.9%	72.3%	56.1%
Op15C1	70.2%	96.7%	0.0%	92.8%	96.1%	66.1%	100.0%	99.6%	98.0%	45.9%	NaN	89.3%	89.9%
Op20C1	55.8%	91.5%	0.0%	71.6%	99.4%	48.5%	99.7%	97.6%	92.6%	32.3%	-3.4%	75.2%	91.8%
AVG	73.9%	93.1%	17.1%	82.6%	89.2%	73.4%	97.5%	94.7%	94.8%	59.7%	24.9%	78.0%	81.2%
AVG ¥ (Ref)	78.8%	93.0%	28.0%	87.4%	95.4%	82.0%	98.1%	93.3%	93.9%	68.8%	34.0%	80.3%	86.0%

*NT: Normal Tissue; TT: Tumor Tissue; HT: Hypervascularized Tissue; BG: Background.
 ¥ Average reference results (employing 128 bands with the BPF method).

From the results obtained in this method it is possible to emphasize that the **OA** decreases slightly compared to the reference results, specifically from 78.8% to 73.9%. Besides, if the average **sensitivity** of class 2 (tumor class) is examined, it is clearly observed that the number of successfully classified pixels of this class has notably worsened, reaching 17%. It should be noted that the *Op15C1* image goes from a sensitivity of 67% (reference results) to 0%. This fact may be due to the number of generations is very small and is not able to find the optimal combination of spectral bands. In terms of **specificity**, the success rate is still high but lower than the reference results, with the worst case being the normal tissue class with 73.4%.

Another aspect to highlight is in the **MCC** metric, where, like in the rest of the metrics, the tumor class has the worst rate of success. Its percentage of success goes down from 34% to 24.9%. Particularly, in the *Op15C1* image the tumor class gives an indetermination. This is because no pixels have been predicted as true positive or false positive in the tumor class, giving equation 4.5 an indetermination. In *Op8C2*, *Op15C1*, *Op20C1* images the tumor class is really low, reaching in one case a negative success rate.

Figure 5-2 shows the **classification maps** after the evaluation of the most representative bands obtained through GA with 30 generations. Looking at each one of the **classification maps** and taking into account the reference maps, it is observed that the visualization of the location of the brain tumor worsens in general. Two image results to be highlighted are *Op8C1* and *Op15C1*. The first one, after using the optimization algorithm, improves the identification of the area affected by the tumor. Otherwise, GA has completely eliminated the tumor class on the *Op15C1* image, worsening significantly with respect to the reference map.

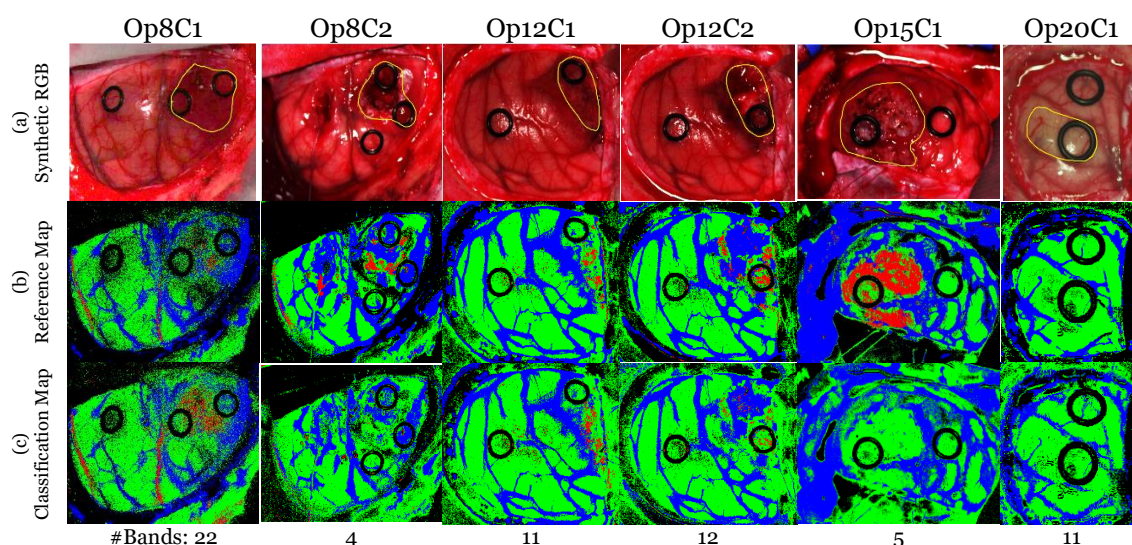


Figure 5-2. Resulting classification maps after GA use with 30 generations and the entire dataset for the SVM training. (a) Synthetic RGB representation of the HS cube with the tumor area surrounded by a yellow line. (b) Reference classification map. (c) Classification Map

5.2.2.2 GA evaluation using 60 generations

Once finished evaluating the GA algorithm with 30 generations, the same procedure was repeated with 60 generations. The resulting selected bands were not the same, so the evaluation metrics were computed again, providing the results shown in Table 5-3. It can be observed that the **OA** increases slightly after doubling the number of generations, from 73.9% to 75.9%. If the **sensitivity** is observed, it should be noted that all classes also increase their accuracy as the number of generations increase. However, in the case of the *Op8C2* image, the sensitivity in the tumor class worsens, getting to be eliminated completely. On the other hand, in the case of the *Op15C1*, where previously the worst case of sensitivity in the tumor class occurred, increases again to 38.9%. As for the *Op20C1*, the tumor class is still not detected.

With regard to **specificity**, all classes increase their success rate, where the worst case occurs in the normal tissue class with 81.2%. Regarding the **MCC** metric, as in the previous cases, the class with the worst success rate is the tumor class with 32.8%. From this metric it is worth mentioning the indetermination of the *Op8C2* image, due to not classifying any pixel as tumor class (no true and false positives), and the low success rate of the *Op20C1* image, independently of the slight improvement after using 60 generations.

Figure 5-3 shows the **classification maps** after the evaluation of the most representative bands obtained through GA with 60 generations. It should be noted that the fifth image (*Op15C1*) once again indicates where the brain tumor zone is clearly located. However, it also has some areas with false positives. Furthermore, the *Op20C1* image begins to show small groups of tumor pixels scattered randomly. It also shows some pixels of background in the middle of the classification maps where previously the normal class was identified and where, in fact, corresponds with the tumor area. The rest of patients more or less offer the same classification maps previously observed.

Table 5-3. GA 60 generations results obtained with all bands and the entire dataset for the SVM training.

Patient ID	OA	Sensitivity				Specificity				MCC			
		NT	TT	HT	BG	NT	TT	HT	BG	NT	TT	HT	BG
Op8C1	63.4%	76.6%	36.2%	48.2%	100.0%	74.3%	87.2%	89.6%	81.7%	50.9%	26.2%	42.0%	63.7%
Op8C2	93.0%	96.9%	0.0%	96.7%	93.1%	94.8%	100.0%	97.6%	97.1%	86.7%	NaN	87.5%	87.3%
Op12C1	91.8%	98.6%	43.7%	91.6%	99.1%	90.2%	99.8%	98.1%	99.6%	84.1%	62.9%	89.0%	97.8%
Op12C2	68.6%	97.1%	5.7%	95.2%	51.6%	67.9%	99.8%	81.4%	98.4%	59.5%	19.9%	71.6%	59.2%
Op15C1	80.6%	96.2%	38.9%	93.3%	97.4%	79.1%	99.8%	97.3%	98.6%	58.5%	55.9%	90.3%	92.3%
Op20C1	57.9%	95.1%	0.0%	79.6%	100.0%	81.0%	100.0%	99.1%	48.7%	69.6%	-0.8%	84.1%	47.2%
AVG	75.9%	93.4%	20.7%	84.1%	90.2%	81.2%	97.8%	93.8%	87.3%	68.2%	32.8%	77.4%	74.6%
AVG ¥ (Ref)	78.8%	93.0%	28.0%	87.4%	95.4%	82.0%	98.1%	93.3%	93.9%	68.8%	34.0%	80.3%	86.0%

*NT: Normal Tissue; TT: Tumor Tissue; HT: Hypervascularized Tissue; BG: Background.
 ¥ Average reference results (employing 128 bands with the BPF method).

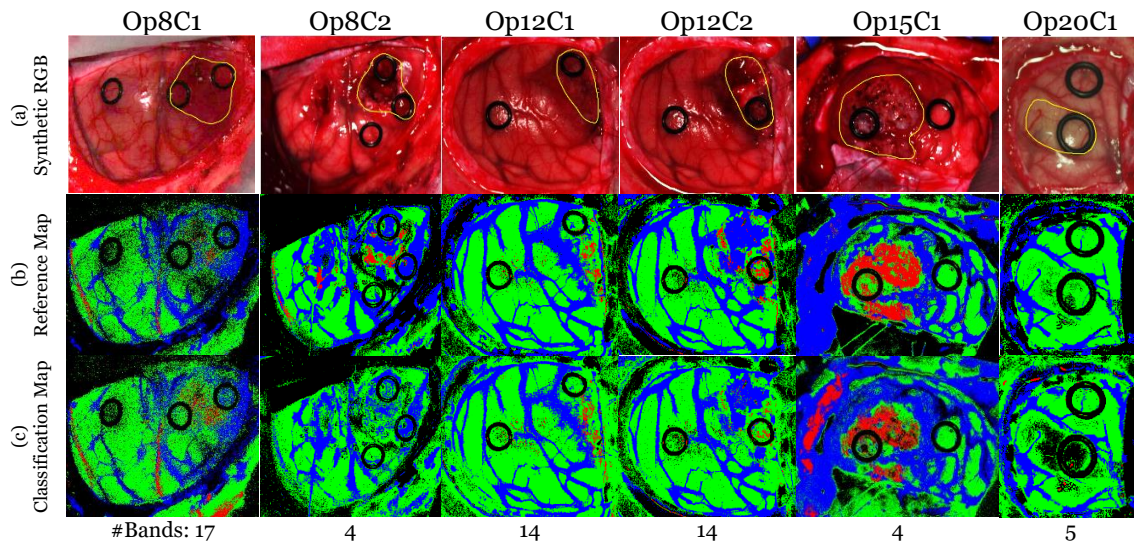


Figure 5-3. Resulting classification maps after GA use with 60 generations and the entire dataset for the SVM training. (a) Synthetic RGB representation of the HS cube with the tumor area surrounded by a yellow line. (b) Reference classification map. (c) Classification Map

5.2.3 BPF with PSO evaluation

Similarly, to the GA evaluation, the PSO algorithm was evaluated twice, with 30 and 60 generations. Evaluating only with 30 generations there was no possible to find the global minimum, so employing the 60 generations the algorithm was able to find the convergence.

5.2.3.1 PSO evaluation using 30 generations

After making the selection of the most representative bands with 30 generations, the SVM classification results were obtained using these selected bands. Table 5-4 shows the results obtained after the evaluation.

Table 5-4. PSO 30 generations results obtained with all bands and the entire dataset for the SVM training.

Patient ID	OA	Sensitivity				Specificity				MCC			
		NT	TT	HT	BG	NT	TT	HT	BG	NT	TT	HT	BG
Op8C1	58.4%	69.8%	21.8%	52.7%	100.0%	70.0%	88.8%	87.1%	75.1%	39.8%	13.5%	42.5%	56.5%
Op8C2	93.5%	97.1%	31.9%	97.8%	93.0%	95.3%	97.9%	99.6%	98.4%	87.8%	21.8%	97.0%	88.2%
Op12C1	90.9%	98.9%	46.2%	89.5%	99.5%	88.8%	99.9%	98.1%	99.7%	82.5%	66.1%	86.9%	98.2%
Op12C2	67.6%	97.0%	4.9%	95.9%	48.4%	67.6%	99.0%	80.0%	98.4%	59.4%	11.3%	70.9%	56.7%
Op15C1	82.6%	99.7%	47.9%	92.0%	98.4%	80.1%	100.0%	99.3%	99.4%	61.9%	63.4%	90.3%	96.2%
Op20C1	57.1%	95.6%	0.0%	74.7%	99.5%	49.6%	99.9%	99.4%	90.6%	36.5%	-2.3%	81.5%	89.7%
AVG	75.0%	93.0%	25.5%	83.8%	89.8%	75.2%	97.6%	93.9%	93.6%	61.3%	29.0%	78.2%	80.9%
AVG ¥ (Ref)	78.8%	93.0%	28.0%	87.4%	95.4%	82.0%	98.1%	93.3%	93.9%	68.8%	34.0%	80.3%	86.0%

*NT: Normal Tissue; TT: Tumor Tissue; HT: Hypervascularized Tissue; BG: Background.

¥ Average reference results (employing 128 bands with the BPF method).

After observing each one of the results obtained, it should be noted that the **OA** is slightly reduced compared to the reference results (Table 5-1), going down from 78.9% to 75%. Regarding **sensitivity**, the second class (tumor tissue) is again the one with the lowest success rate with 25.5%, decreasing also respect to the reference result (28%). The worst cases are observed in the fourth image (*Op12C2*) with 4.9%, and in the last image (*Op20C1*) without any successfully tumor pixel identification. The rest of the images improved slightly the results, giving the best result the *Op15C1* with 47.9%.

On the other hand, the **specificity** of each class in general is high, with class 1 with 75.2% as the worst result. These results also slightly reduce their success, where originally it was 82%. As for the **MCC**, class 2 returns to have the worst result compared to the rest, with 29%. The first, fourth and the sixth images are those who have a minor success, reaching 13.5% and the best case is the third image, with a 66.1%.

After looking at the **classification maps** shown in Figure 5-4, it should be noted that the *Op15C1* image is the one that most clearly shows where the brain tumor is located. The rest of the maps, however, show some small groups of pixels of the tumor class spread over the area where the brain tumor is found, such as images *Op12C1* and *Op12C2*. As for the last image, it does not show a single tumor pixel.

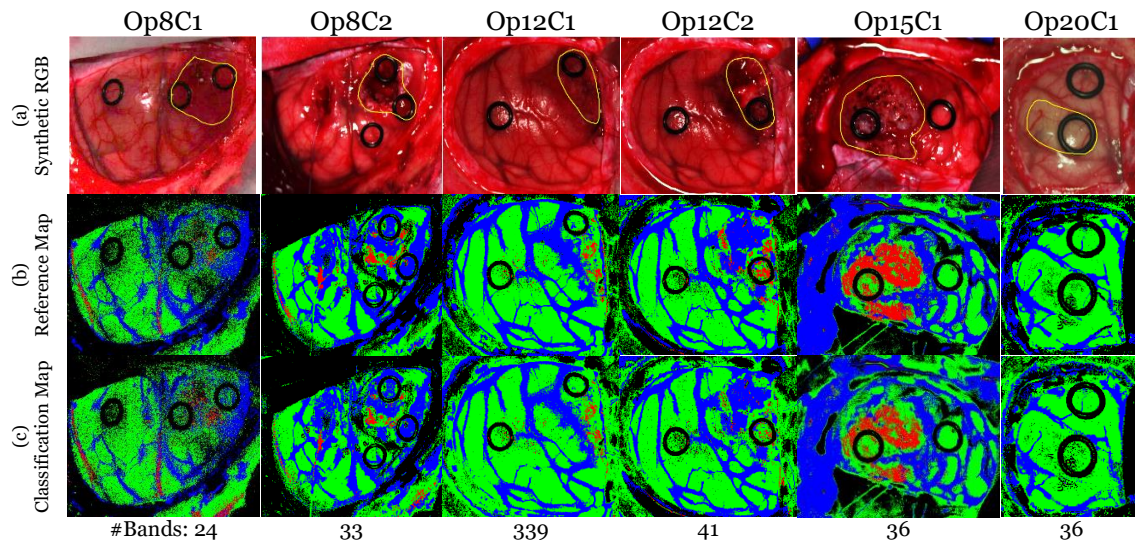


Figure 5-4. Resulting classification maps after PSO use with 30 generations and the entire dataset for the SVM training. (a) Synthetic RGB representation of the HS cube with the tumor area surrounded by a yellow line. (b) Reference classification map. (c) Classification Map

5.2.3.2 PSO evaluation using 60 generations

Once the PSO algorithm was evaluated with 30 generations, the same process was repeated with 60 generations. Then, the bands obtained were evaluated quantitatively and qualitatively using the evaluation metrics that are observed in Table 5-5 and Figure 5-5.

Table 5-5. PSO 60 generations results obtained with all bands and the entire dataset for the SVM training.

Patient ID	OA	Sensitivity				Specificity				MCC			
		NT	TT	HT	BG	NT	TT	HT	BG	NT	TT	HT	BG
Op8C1	61.1%	72.9%	29.7%	51.4%	100.0%	80.5%	87.0%	85.3%	76.9%	53.3%	19.3%	38.5%	57.8%
Op8C2	93.5%	96.6%	33.3%	98.1%	93.1%	95.2%	98.3%	99.4%	97.8%	87.4%	24.8%	96.2%	87.9%
Op12C1	90.9%	98.8%	40.6%	90.1%	99.4%	88.7%	99.9%	98.2%	99.6%	82.4%	61.5%	87.5%	98.1%
Op12C2	67.2%	96.3%	2.7%	95.9%	48.8%	67.3%	98.7%	80.3%	98.0%	58.5%	4.0%	71.3%	56.2%
Op15C1	82.5%	99.1%	47.5%	92.2%	98.4%	80.2%	100.0%	98.6%	99.4%	61.6%	63.1%	89.9%	96.2%
Op20C1	57.0%	95.2%	0.1%	74.2%	99.7%	50.2%	99.9%	99.3%	88.3%	36.7%	-0.2%	81.0%	87.4%
AVG	75.4%	93.1%	25.6%	83.7%	89.9%	77.0%	97.3%	93.5%	93.3%	63.3%	28.8%	77.4%	80.6%
AVG ¥ (Ref)	78.8%	93.0%	28.0%	87.4%	95.4%	82.0%	98.1%	93.3%	93.9%	68.8%	34.0%	80.3%	86.0%

*NT: Normal Tissue; TT: Tumor Tissue; HT: Hypervascularized Tissue; BG: Background.

¥ Average reference results (employing 128 bands with the BPF method).

If the results obtained after the evaluation of the 60 generations are carefully observed, it is possible to see that the average of each one of the results is practically the same than the PSO 30 generations results. The greatest change is in the **specificity** of the normal class, where there is an increment of 1.8% with respect to the result obtained with 30 generations. The **OA** metric increases only a 0.4% and the **sensitivity** of the tumor class increases 0.1%, where the *Op12C2* and *Op20C1* images are the ones with the worst rate of success. In this case, *Op12C2* gets worse, going down from 4.9% to 2.7% and the *Op20C2* image increases just a 0.1%. Regarding the **MCC** metric, the tumor class decreases a 0.2% while the normal class increases a 2%. The results for the rest of the classes remain more or less constant.

Figure 5-5 shows the classification maps of the six images to be evaluated, where it is possible to notice that the *Op15C1* clearly indicates where the brain tumor is located and its shape. However, some false positives are displayed in the upper left part of the image.

As for the other images, *Op8C1* and *Op8C2* show different small areas where there may be brain tumor. In these cases, it is not possible to clearly identify the location of the tumor and its size. Regarding *Op12C1* and *Op12C2*, small amounts of pixels of the tumor class are observed in the same area, giving a slight idea where the tumor is located. As for the *Op20C1* image, no pixel with the tumor class is observed, being impossible to find out its location and its form.

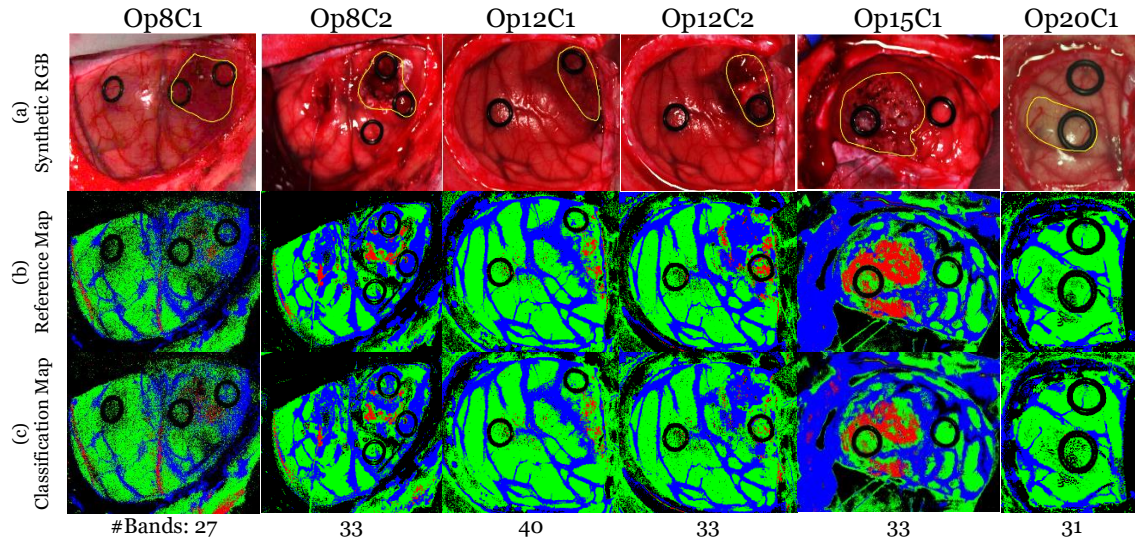


Figure 5-5. Resulting classification maps after PSO use with 60 generations and the entire dataset for the SVM training. (a) Synthetic RGB representation of the HS cube with the tumor area surrounded by a yellow line. (b) Reference classification map. (c) Classification Map

5.3 Band selection evaluation using OPF

In this section, the same structure proposed in Section 5.2 is followed. The reference values (128 bands) and the results obtained after the generation of the GA and PSO algorithms, employing the $OA_{\text{Penalized}}$ metric to obtain the optimized results, are presented.

5.3.1 Reference results

The HS images were evaluated with the 128 bands that compose the HS cubes for performing a comparison with the band selection algorithm results. The purpose of this is to find out if there are improvements using only a certain number of bands.

Table 5-6 shows the accuracy, sensitivity, specificity and MCC results obtained as reference results with the OPF methodology. Observing these results, it should be noted that when balancing the number of pixels per class, the **OA** rate drops by around 4% (74.3%) when compared with the reference results with the entire dataset (78.8%). However, it is worth noticing that in terms of **sensitivity**, the class that has the worst result is the tumor class, with 44.8%. Comparing this result with the Table 5-1 (reference results of the BPF), the success rate increases significantly, specifically a 16.8%. Nevertheless, there are still images with a minimum success rate in identifying the tumor class, such as the *Op20C1* with a 1.6%.

Otherwise, all the results of the **specificity** are high, giving the worst case the background class with 77%. With respect to the **MCC** metric, the class with the worst result is the tumor class with 42.5%, again giving the worst result the *Op20C1* image with 9.3%.

After analyzing the quantitative results, an analysis of the **classification maps** obtained was carried out. From Figure 5-6, it should be noted that the *Op15C1* and *Op8C1* images clearly show the location and shape of the brain tumor, although they have some false positives. On the other hand, *Op12C1* and *Op12C2* do not clearly show the shape and size of the tumor, but indicate where the tumor is located. In the case of *Op8C2*, the pixels of the tumor class are distributed throughout the classification map, preventing the determination of the shape and location of the brain tumor. Finally, the *Op20C1* image is still unable of performing the identification of the brain tumor location.

Table 5-6. Reference results obtained with all bands and the reduced dataset for the SVM training.

Patient ID	OA	Sensitivity				Specificity				MCC			
		NT	TT	HT	BG	NT	TT	HT	BG	NT	TT	HT	BG
Op8C1	45.3%	32.2%	49.1%	38.6%	100.0%	87.1%	78.5%	97.6%	46.0%	22.8%	28.3%	47.5%	32.2%
Op8C2	93.5%	89.3%	47.8%	88.8%	96.3%	98.9%	96.7%	99.6%	92.8%	90.4%	26.2%	91.7%	88.6%
Op12C1	89.9%	79.8%	76.1%	94.6%	99.6%	95.2%	99.5%	98.8%	93.1%	77.1%	82.3%	92.6%	77.3%
Op12C2	69.9%	59.4%	13.3%	98.7%	78.2%	88.1%	98.3%	81.0%	79.3%	49.6%	22.9%	74.0%	56.8%
Op15C1	91.0%	88.3%	80.7%	95.6%	98.7%	95.1%	99.6%	99.8%	94.7%	79.1%	86.0%	95.2%	77.6%
Op20C1	56.3%	83.3%	1.6%	79.9%	100.0%	61.8%	99.9%	99.4%	61.3%	37.7%	9.3%	85.0%	60.5%
AVG	74.3%	72.0%	44.8%	82.7%	95.5%	87.7%	95.4%	96.0%	77.9%	59.4%	42.5%	81.0%	65.5%

*NT: Normal Tissue; TT: Tumor Tissue; HT: Hypervascularized Tissue; BG: Background.

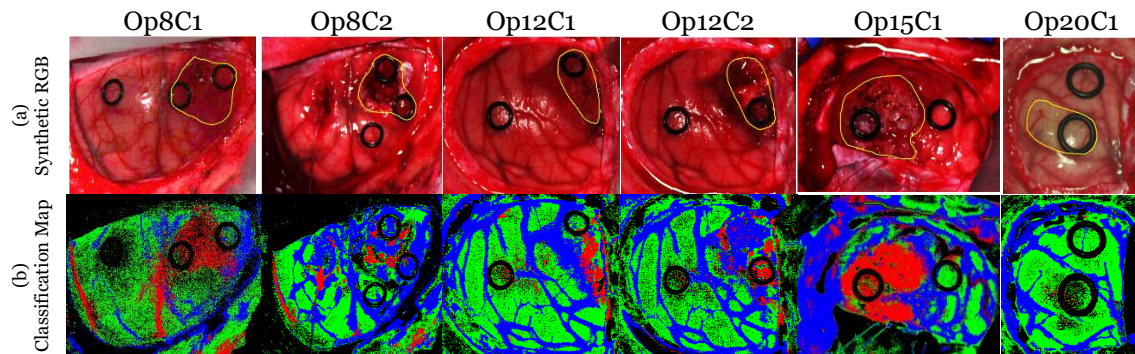


Figure 5-6. Reference results obtained with all bands and the reduced dataset for the SVM training. (a) Synthetic RGB representation of the HS cube with the tumor area surrounded by a yellow line. (b) Classification map.

5.3.2 OPF with GA evaluation

Once the genetic algorithm is generated, it shows which optimal bands were selected for each test image. Therefore, the GA is executed with 60 generations. For this case, the observed results show the evaluation of the bands selected for each image by the optimization algorithm in Table 5-7.

Table 5-7. GA results obtained with all bands and the reduced dataset for the SVM training.

Patient ID	OA	Sensitivity				Specificity				MCC			
		NT	TT	HT	BG	NT	TT	HT	BG	NT	TT	HT	BG
Op8C1	67.7%	58.9%	90.3%	46.8%	100.0%	95.5%	74.9%	98.3%	80.8%	58.8%	57.8%	57.6%	61.1%
Op8C2	92.5%	98.4%	26.1%	91.9%	92.1%	95.5%	97.6%	98.3%	98.8%	89.2%	16.8%	87.5%	87.2%
Op12C1	89.7%	80.1%	83.0%	93.6%	99.0%	94.5%	94.0%	99.1%	99.3%	76.2%	58.3%	91.7%	96.5%
Op12C2	72.0%	85.9%	31.3%	98.4%	57.8%	76.0%	96.5%	84.9%	97.1%	57.0%	37.4%	78.2%	62.1%
Op15C1	94.7%	98.5%	88.9%	96.3%	94.8%	95.4%	99.4%	98.5%	99.6%	86.3%	91.3%	94.7%	95.2%
Op20C1	58.0%	94.2%	0.0%	83.2%	99.1%	87.6%	99.5%	98.9%	46.7%	77.5%	-4.6%	86.3%	44.0%
AVG	79.1%	86.0%	53.3%	85.0%	90.5%	90.7%	93.6%	96.3%	87.0%	74.2%	42.8%	82.7%	74.3%
AVG ¥ (Ref)	74.3%	72.0%	44.8%	82.7%	95.5%	87.7%	95.4%	96.0%	77.9%	59.4%	42.5%	81.0%	65.5%

*NT: Normal Tissue; TT: Tumor Tissue; HT: Hypervascularized Tissue; BG: Background.

¥ Average reference results (employing 128 bands with the OPF method).

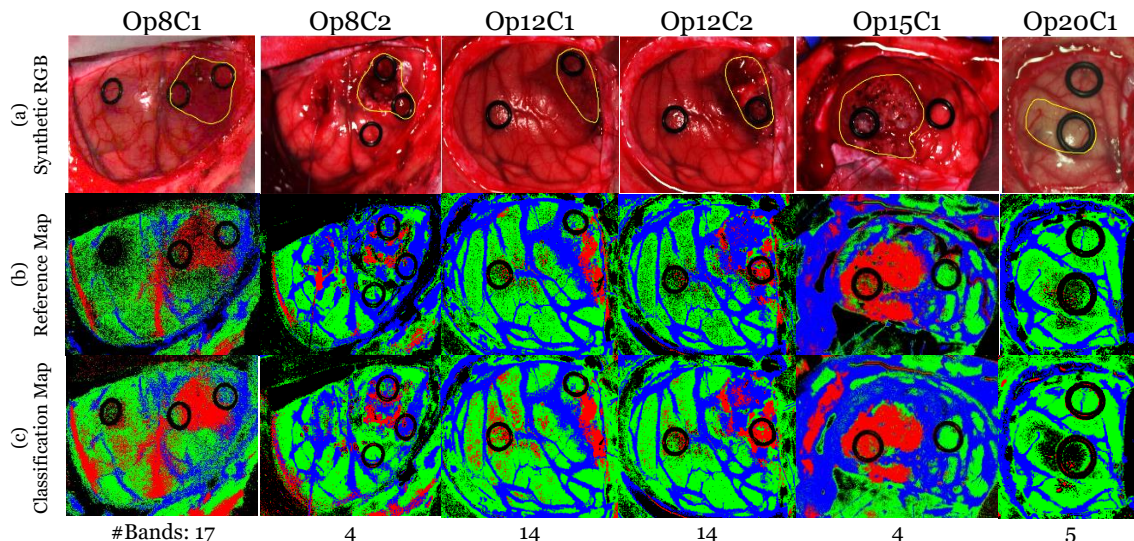


Figure 5-7. Resulting classification maps after GA use with 60 generations and the reduced dataset for the SVM training. (a) Synthetic RGB representation of the HS cube with the tumor area surrounded by a yellow line. (b) Reference classification map. (c) Classification Map

Comparing the results of the genetic algorithm with the reference results, it can be observed that the **OA** increases by 4.8% using GA. The **sensitivity** of the tumor class goes from 44.8% to 53.3%, with the worst case in the image *Op20C1* that does not re-label the tumor class. As for the **specificity**, these remain practically the same, giving the worst result the background class with 87%. Finally, the **MCC** slightly improved in the tumor class, specifically from 42.5% to 42.8%, giving as a worse result the *Op20C1* with -4.6%.

Next, Figure 5-7 after the evaluation of the most representative bands obtained through GA with 60 generations.

Observing the **classification maps** of Figure 5-7, it can be seen that *Op20C1* does not show tumor, only some pixels distributed throughout the classification map. The *Op8C1* and *Op8C2* images show where the brain tumor is located (top right corner) and many false positives throughout the classification map. *Op12C1* and *Op12C2*, like previous patients, show without having a clear form where the tumor is located, however, they also possess some pixels of the tumor class spread over the classification map. As

for the image *Op15C1*, it clearly shows the location and shape of the tumor. However, it also has a high number of false pixels of the tumor class on the left side of the classification map.

5.3.3 OPF with PSO evaluation

Like the GA, PSO is executed with 60 generations. Once the algorithm is generated, Table 5-8 shows the results obtained with the optimal bands selected for each test image.

Table 5-8. PSO results obtained with all bands and the reduced dataset for the SVM training.

Patient ID	OA	Sensitivity				Specificity				MCC			
		NT	TT	HT	BG	NT	TT	HT	BG	NT	TT	HT	BG
Op8C1	57.2%	44.5%	81.1%	36.9%	100.0%	91.8%	69.6%	97.6%	68.4%	41.3%	46.0%	47.1%	49.1%
Op8C2	92.1%	93.7%	33.3%	89.2%	93.2%	98.4%	94.6%	99.7%	96.1%	92.2%	13.6%	92.4%	86.4%
Op12C1	89.7%	80.0%	60.1%	95.8%	99.5%	96.1%	95.1%	95.7%	98.2%	78.8%	47.0%	91.3%	92.5%
Op12C2	64.9%	76.1%	32.9%	97.5%	45.6%	70.1%	93.7%	83.2%	92.9%	42.6%	32.0%	76.7%	45.1%
Op15C1	89.6%	96.0%	68.9%	96.5%	98.7%	90.6%	99.9%	99.3%	97.3%	74.9%	78.5%	95.5%	87.2%
Op20C1	56.5%	88.0%	0.0%	80.0%	99.7%	68.0%	99.9%	98.3%	55.1%	48.5%	-2.4%	82.8%	53.8%
AVG	75.0%	79.7%	46.1%	82.6%	89.5%	85.8%	92.1%	95.6%	84.7%	63.0%	35.8%	81.0%	69.0%
AVG ¥ (Ref)	74.3%	72.0%	44.8%	82.7%	95.5%	87.7%	95.4%	96.0%	77.9%	59.4%	42.5%	81.0%	65.5%

*NT: Normal Tissue; TT: Tumor Tissue; HT: Hypervascularized Tissue; BG: Background.

¥ Average reference results (employing 128 bands with the OPF method).

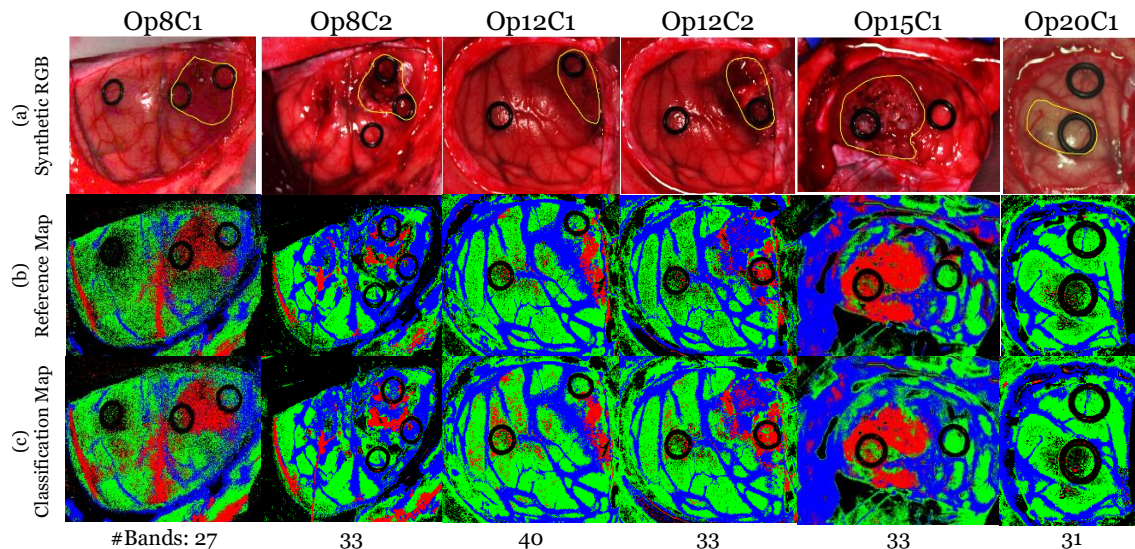


Figure 5-8. Resulting classification maps after PSO use with 60 generations and the reduced dataset for the SVM training. (a) Synthetic RGB representation of the HS cube with the tumor area surrounded by a yellow line. (b) Reference classification map. (c) Classification Map

Comparing the results obtained with the Table 5-6, the results slightly vary. The **OA** only increases 0.7%. In terms of **sensitivity**, the tumor class is again the lowest with the same percentage of success, specifically 46.1%. However, if it is observed that the results of all the images of this class, more or less takes remain constant, except for the first image, *Op8C1*, which improves almost 32% in the identification of the tumor.

Respecting to **specificity**, the results remain practically the same. Finally, with respect to the **MCC** metric, as in the previous metrics, the results remain constant, except the tumor class, that get worse, specifically 35.8%. However, with the image *Op8C1*, improves by around 28%.

Observing the **classification maps**, it should be noted that the results obtained are practically the same as those shown in Figure 5-6. Therefore, as previously commented the *Op15C1* image is the one that most clearly shows where the brain tumor is located. The rest of the maps, show different areas of tumors spread over the classification map. Nevertheless, it can be observed that this tumor is located where there is higher concentration of pixels of the tumor class, with the exception of the last patient, who does not indicate where the brain tumor is located, because it shows some small pixels spread over the classification map.

5.4 Comparison of the BPF and OPF results

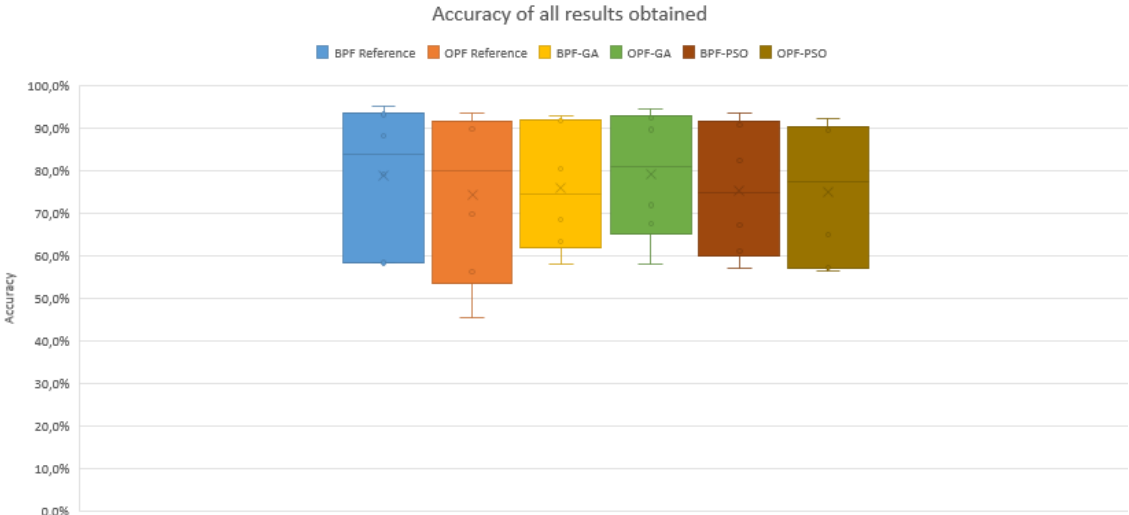
In this section, a comparison of the OA and sensitivity of the tumor class results obtained in all the evaluations presented previously is performed. In order to determine which methodologies are the best ones, boxplots have been employed (Figure 5-9). In this comparison, only the results of 60 generations have been included for the GA and PSO algorithms.

Figure 5-9.a shows the OA of all the results obtained so far. It should be noted that all are between the same ranges, from 55% to 92-93%. Analyzing each of the developed techniques, it can be observed that among the patients many results vary. For example, observing the reference results with the reduced dataset (OPF Reference), there is one patient with an accuracy of 91% and another patient with an accuracy of 55%. In this case, we look for the algorithm that generates good and similar results for all the images. Taking this approach into account, it was decided that the two best cases, analyzing only the OA, are the GA with the reduced dataset (OPF-GA) and the PSO with the complete dataset (BPF-PSO) followed very closely by the PSO algorithm with the reduced dataset (OPF-PSO).

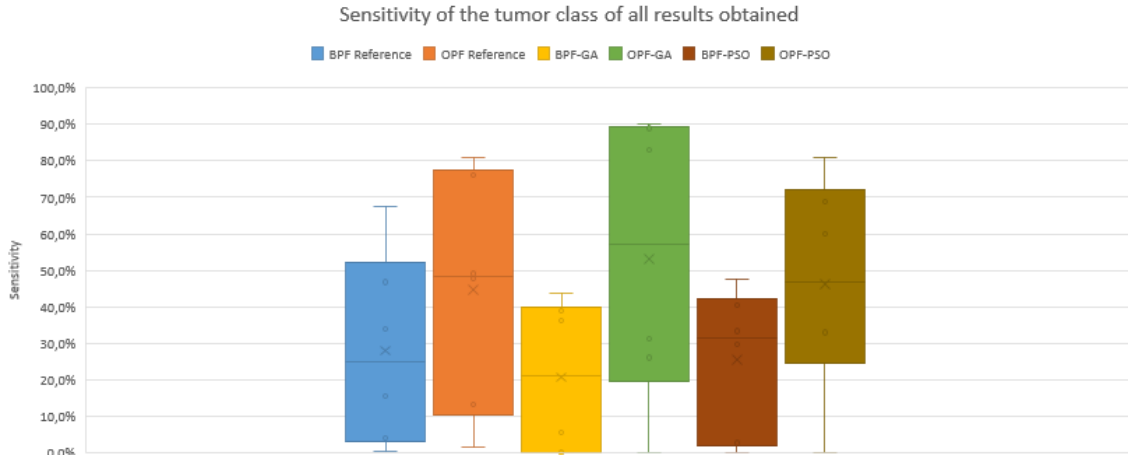
Regarding Figure 5-9.b, it can be clearly seen that the techniques that use the reduced dataset have better sensitivity results, reaching in the best case around 90%, as it is in the case of GA (OPF-GA). The next best case is the PSO algorithm with the reduced dataset (OPF-PSO), reaching 80% at some point. As for the rest of the methods, it can be seen that the best cases of sensitivity do not exceed 50. Looking at the two graphs at the same time, it is observed that one of the models that best OA has, is one that has worse sensitivity (BPF-GA). Therefore, another metric is needed to select the best model.

Figure 5-10 illustrates all the classification maps obtained so far. These maps allow a better visualization of the results. Figure 5-10.a shows the RGB images indicating the location of the tumor with a yellow circle. Taking these images as reference, it is observed that the techniques that use the complete database (BPF method), Figure 5-10 .b, d and e, are only able to detect the tumor in the image *Op15C1*. As for the techniques using the reduced database (OPF method), Figure 5-10.c, e and g, are able to show where the tumor is in the images, although false positives exist in almost all the images. Finally, it is observed that the *Op20C1* image does not identify the tumor for any of the cases.

Making a combination of the results observed in these metrics, it was decided to evaluate both optimization algorithms (GA and PSO) using a new proposed metric (the FoM presented in Section 4.2.1) and only employing the OPF method.



(a)



(b)

Figure 5-9. Boxplot diagram of the (a) overall accuracy and (b) sensitivity of the tumor class of all the evaluated techniques

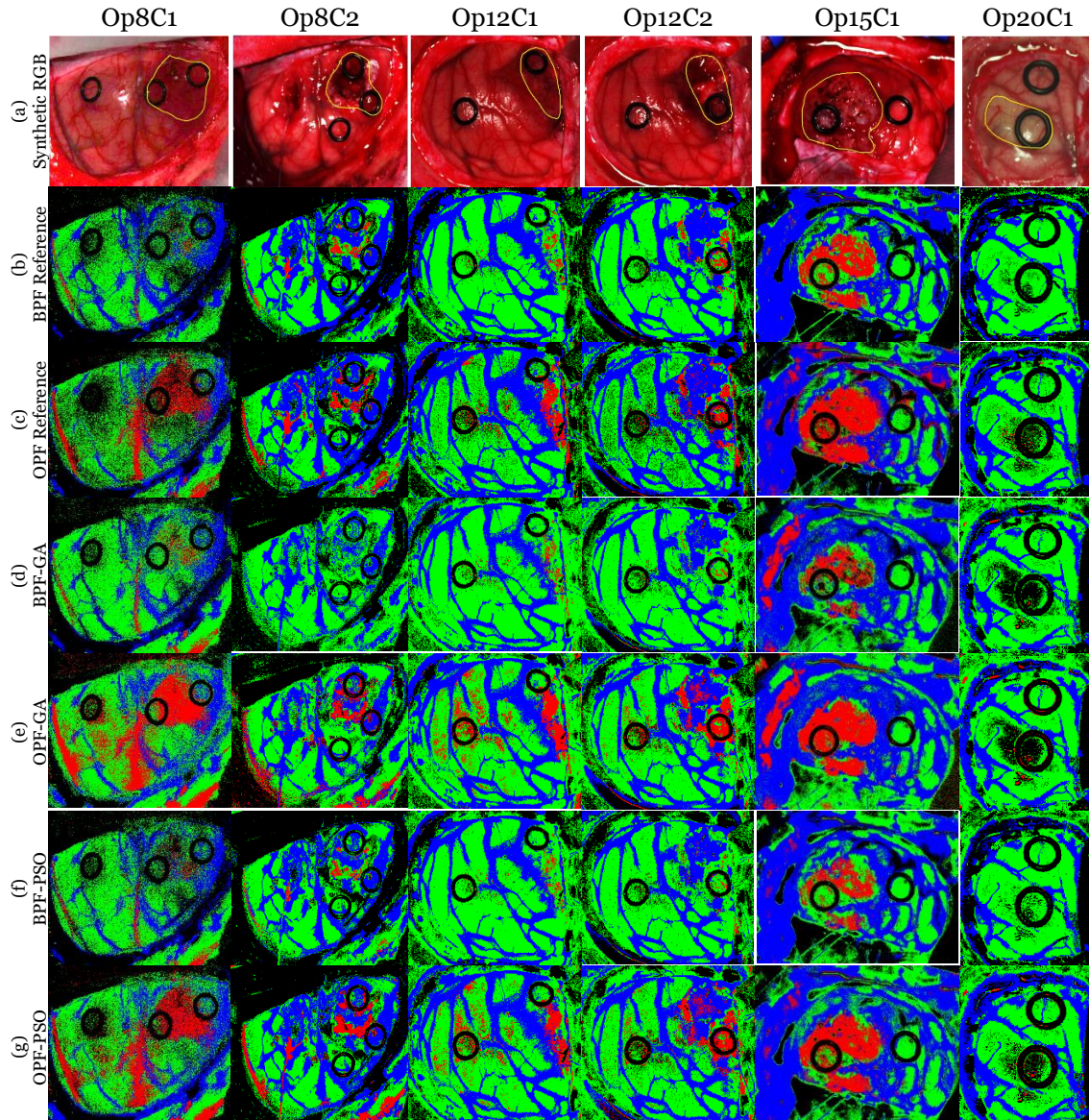


Figure 5-10. Classifications maps of the test dataset. (a) Synthetic RGB images with a yellow line determining the area tumor. (b and c) Reference results with the entire and reduced dataset. (d and e) GA algorithm using 60 generations with entire and reduced dataset. (f and g) PSO algorithm using 60 generations with entire and reduced dataset.

5.5 Band selection using the FoM evaluation metric

In this section, the optimization algorithms of GA and PSO with 60 generations are analyzed again using as an evaluation metric the FoM explained in section 4.2.1. This metric is proposed, because with $OA_{penalized}$ a method with better OA does not imply that it also obtained a better sensitivity in the identification of the tumor class. Therefore, FoM and $FoM_{penalized}$ are based on finding more balanced results among the four classes. This FoM has the goal of finding the most balanced accuracy per class results. After the execution, it was observed that a high number of bands were obtained. Therefore, it was decided to re-evaluate this process with a metric called $FoM_{penalized}$, whose purpose is the same as the FoM, but penalizing the use of a large number of bands.

5.5.1 OPF with FoM evaluation metric

Next, the OPF band selection algorithm is evaluated by means of the GA and PSO optimization algorithms taking into account the FoM to find the most suitable bands for an accurate classification.

5.5.1.1 OPF with GA and FoM

Once the GA is generated, it shows which bands were selected for each test image. Table 5-9 shows the results obtained with these bands after their evaluation. Observing the results obtained and comparing it with the reference results in Table 5-6, it should be noticed that **OA** improves more than 6% respect to the reference results. In the case of **sensitivity**, the success rate of the classes, with the exception of the tumor class, is higher than 80%. The sensitivity of the tumor class is 66%, being much higher than the reference result (44.8%). However, the image *Op20C1* still does not offer good results (0.1%).

Regarding the **specificity**, the results are high, having as a worst class the class of normal tissue with 86.9%. In the case of the **MCC** metric, the success rate of all the classes improves with respect to the reference ones. However, if the tumor class is observed, it should be noted that the image *OP20C1* returns to give bad results, only 2% is correct.

Figure 5-11 shows the **classification maps** obtained in this experiment. It should be noted that the *Op8C1* image shows tumor throughout the classification map. The images *Op12C1* and *Op12C2* show where the brain tumor is located, although it has certain pixels that indicate tumor in areas that are not correct. This happens also with the image *Op8C2*. As for the *Op15C1* image, it shows almost perfectly the location, size and shape of the brain tumor. With respect to the *Op20C1* image, some pixels of the tumor class are displayed distributed by the classification map, although it does not show the tumor area.

Table 5-9. OPF GA FoM results obtained with all bands and the reduced dataset for the SVM training.

Patient ID	OA	Sensitivity				Specificity				MCC			
		NT	TT	HT	BG	NT	TT	HT	BG	NT	TT	HT	BG
Op8C1	69.2%	62.2%	92.0%	45.8%	100.0%	98.2%	70.3%	97.3%	88.1%	65.1%	53.8%	54.5%	72.4%
Op8C2	92.8%	94.0%	61.6%	85.8%	93.9%	99.4%	94.4%	99.7%	96.0%	94.8%	26.1%	90.5%	87.5%
Op12C1	92.9%	89.5%	86.7%	94.0%	99.4%	95.1%	98.0%	99.2%	98.1%	84.2%	78.0%	92.5%	92.1%
Op12C2	72.7%	88.5%	59.6%	94.3%	50.6%	72.9%	97.3%	91.5%	95.3%	55.8%	64.6%	83.3%	53.5%
Op15C1	97.6%	98.2%	97.9%	97.0%	99.4%	97.8%	99.9%	99.9%	99.5%	92.5%	98.4%	96.9%	97.0%
Op20C1	58.4%	92.2%	0.1%	86.1%	100.0%	57.7%	100.0%	98.4%	74.1%	40.9%	2.3%	87.4%	72.7%
AVG	80.6%	87.4%	66.3%	83.8%	90.5%	86.9%	93.3%	97.7%	91.8%	72.2%	53.8%	84.2%	79.2%
AVG ¥ (Ref)	74.3%	72.0%	44.8%	82.7%	95.5%	87.7%	95.4%	96.0%	77.9%	59.4%	42.5%	81.0%	65.5%

*NT: Normal Tissue; TT: Tumor Tissue; HT: Hypervascularized Tissue; BG: Background.

¥ Average reference results (employing 128 bands with the OPF method).

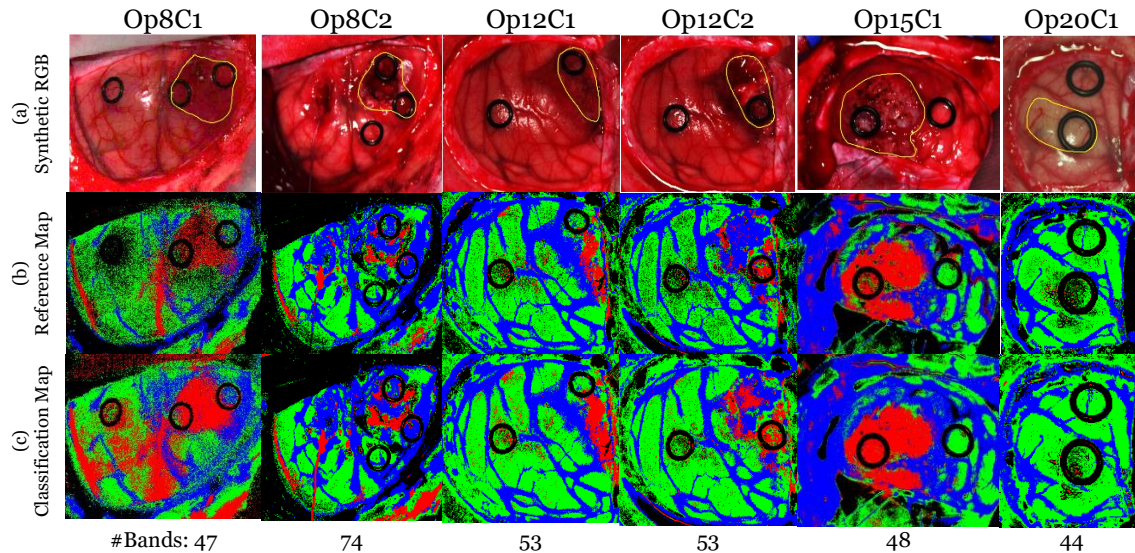


Figure 5-11. Resulting classification maps after GA FoM and the reduced dataset for the SVM training. (a) Synthetic RGB representation of the HS cube with the tumor area surrounded by a yellow line. (b) Reference classification map. (c) Classification Map

5.5.1.2 OPF with PSO and FoM

Once the PSO is executed, the most representative bands were obtained for each image. Table 5-10 shows the results obtained with these bands after their evaluation. Analyzing the results obtained in this experiment, it should be noticed that the average **OA** is slightly lower than the one obtained in the reference results (Table 5-6). The same trend can be observed with the **sensitivity**, having only 43.3% success on the tumor class, compared to 44.8% with the reference one. It is clearly observed that the image Op20C1 does not have any correct pixel of that class. As for the **specificity**, the results are high, giving as a worst result the background class with 83.7%. With respect to the **MCC**, the class with the worst success rate is the tumor class, where only 27% were correctly identified.

From the classification maps presented in Figure 5-12, it is generally pointed out that only the *Op15C1* image clearly provides the location of the brain tumor. However, in this case, there is an area along the left side of the classification map that shows false positives of tumor pixels. The image op20C1 still does not show any tumor and for the rest, there are different areas on all classification maps that show possible locations where the tumor may be.

Table 5-10. OPF PSO FoM results obtained with all bands and the reduced dataset for the SVM training.

Patient ID	OA	Sensitivity				Specificity				MCC			
		NT	TT	HT	BG	NT	TT	HT	BG	NT	TT	HT	BG
Op8C1	55.9%	49.3%	60.6%	41.9%	100.0%	86.3%	76.4%	95.2%	65.7%	38.2%	35.3%	46.5%	46.7%
Op8C2	92.8%	96.6%	32.6%	90.7%	93.1%	98.6%	94.5%	99.8%	97.8%	94.6%	13.1%	93.8%	87.8%
Op12C1	79.8%	41.3%	64.7%	97.6%	98.5%	97.5%	81.8%	95.0%	99.8%	51.2%	26.1%	92.6%	98.4%
Op12C2	60.2%	56.4%	34.0%	97.0%	47.1%	69.9%	84.1%	81.7%	96.3%	24.6%	17.1%	75.7%	51.3%
Op15C1	89.9%	98.4%	67.9%	96.9%	98.4%	89.4%	99.9%	99.7%	98.8%	74.3%	77.8%	96.3%	93.2%
Op20C1	56.7%	89.4%	0.0%	81.7%	98.2%	91.8%	98.6%	98.5%	43.8%	79.6%	-7.4%	84.5%	40.7%
AVG	72.5%	71.9%	43.3%	84.3%	89.2%	88.9%	89.2%	95.0%	83.7%	60.4%	27.0%	81.6%	69.7%
AVG ¥ (Ref)	74.3%	72.0%	44.8%	82.7%	95.5%	87.7%	95.4%	96.0%	77.9%	59.4%	42.5%	81.0%	65.5%

*NT: Normal Tissue; TT: Tumor Tissue; HT: Hypervascularized Tissue; BG: Background.

¥ Average reference results (employing 128 bands with the OPF method).

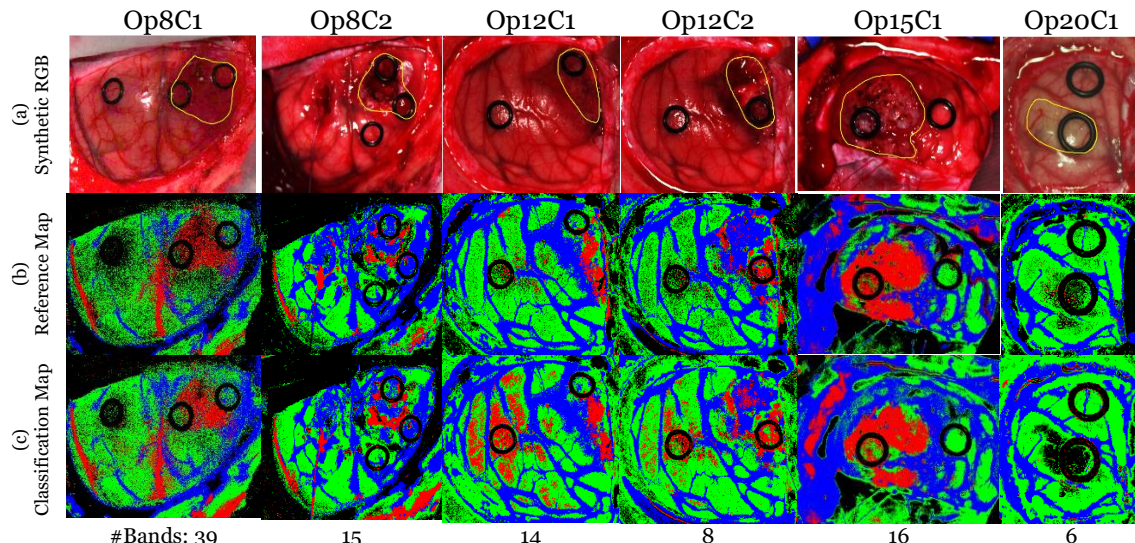


Figure 5-12. Resulting classification maps after PSO FoM and the reduced dataset for the SVM training. (a) Synthetic RGB representation of the HS cube with the tumor area surrounded by a yellow line. (b) Reference classification map. (c) Classification Map

5.5.2 OPF with FoM_{Penalized} evaluation metric

This section presents the OPF band selection algorithm evaluated using the GA and PSO optimization algorithms taking into account the FoM_{Penalized} that offer a penalization when the optimization algorithm employs a high number of bands.

5.5.2.1 OPF with GA and FoM_{Penalized}

Once the genetic algorithm is generated, it shows which bands were selected for each test image taking into account the penalization of the number of bands. Table 5-11 shows the results obtained with these bands after their evaluation. Observing the results obtained and comparing it with the reference results in Table 5-6, it should be noted that the **OA** slightly improve more than 4% the reference result. However, the **sensitivity** improves in a general way. The tumor class, although it has the worst rate of success, is the one that improved the most compared to the reference data, specifically from 44.8% to 64.2%, although it still has an image, Op20C1, which does not identify this class. The **specificity** remains constant and with high results, the worst result is observed in the normal tissue class with 84.6%. As for **MCC**, these results improve slightly, although the tumor class still has a low success rate (45.6%).

Figure 5-13 shows the **classification maps** obtained in this experiment where it should be noted that the Op8C1 and Op12C1 images show tumor throughout the classification map. The image Op12C2 shows where the brain tumor is located, although it has certain pixels that indicate tumor in areas that are not correct, as it also happens with the image Op8C2. As for the Op15C1 image, it shows almost perfectly the location, size and shape of the brain tumor. With respect to the Op20C1 image, some pixels of the tumor class are displayed distributed by the classification map, although it does not show the tumor area.

Observing the Table 5-9 and Figure 5-11, and comparing them with the Table 5-11 and Figure 5-13, it is visualized that the results are similar. However, the number of bands to be used is considerably reduced. Passing on to obtain 74 bands selected in the

Op8C2 image with the OPF GA FoM technique to 18 bands selected with the OPF GA FoM_{Penalized} technique.

Table 5-11. GA FoM_{Penalized} results obtained with all bands and the reduced dataset for the SVM training.

Patient ID	OA	Sensitivity				Specificity				MCC			
		NT	TT	HT	BG	NT	TT	HT	BG	NT	TT	HT	BG
Op8C1	71,0%	66,6%	90,8%	46,7%	100,0%	95,9%	75,1%	98,0%	86,7%	65,8%	57,8%	56,9%	69,4%
Op8C2	92,2%	95,9%	68,8%	87,9%	92,1%	98,2%	94,2%	99,4%	98,8%	93,3%	28,7%	90,0%	87,0%
Op12C1	83,2%	59,4%	88,3%	92,1%	98,8%	93,3%	87,0%	99,8%	99,6%	57,8%	46,2%	89,9%	97,7%
Op12C2	70,8%	89,2%	46,6%	91,9%	51,2%	70,9%	97,7%	88,3%	96,4%	54,5%	55,7%	77,0%	55,8%
Op15C1	94,3%	96,2%	90,4%	95,3%	96,6%	95,4%	99,6%	98,3%	99,1%	85,0%	92,7%	93,5%	93,2%
Op20C1	57,6%	88,1%	0,0%	91,7%	96,8%	53,8%	98,5%	95,7%	87,2%	33,8%	-7,7%	86,3%	83,3%
AVG	78,2%	82,6%	64,2%	84,3%	89,2%	84,6%	92,0%	96,6%	94,6%	65,0%	45,6%	82,3%	81,1%
AVG Υ (Ref)	74,3%	72,0%	44,8%	82,7%	95,5%	87,7%	95,4%	96,0%	77,9%	59,4%	42,5%	81,0%	65,5%

*NT: Normal Tissue; TT: Tumor Tissue; HT: Hypervascularized Tissue; BG: Background.
 Υ Average reference results (employing 128 bands with the OPF method).

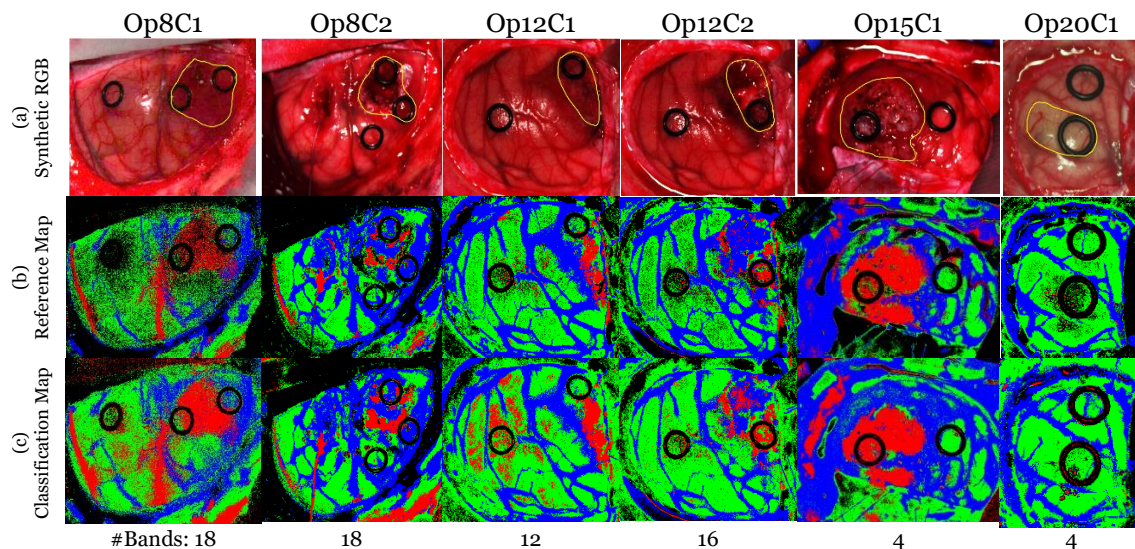


Figure 5-13. Resulting classification maps after GA FoM_{Penalized} and the reduced dataset for the SVM training. (a) Synthetic RGB representation of the HS cube with the tumor area surrounded by a yellow line. (b) Reference classification map. (c) Classification Map

5.5.2.2 OPF with PSO and FoM_{Penalized}

Once the PSO is executed, the most representative bands are obtained for each image. Table 5-12 shows the results obtained with these bands after their evaluation. Analyzing the results obtained with the reference method, it should be noted that the **OA** is slightly higher than the one obtained in the reference (Table 5-6). The same happens with the **sensitivity**, having only 48.8% success of the tumor class, compared to 44.8% with the reference one. It is clearly observed that the image Op20C1 does not have any correct pixel of that class. As for the **specificity**, the results are high, giving as a worst result the background class with 84.5%. With respect to the **MCC**, the class with the worst success rate is the tumor class, where only 37.4% have been correctly identified.

From the **classification maps** observed in Figure 5-14, the results show that the Op8C1 image present false positives of the tumor throughout the classification map. The images Op12C1 and Op12C2 identify where the brain tumor is located, although it has pixels that indicate tumor in areas that are not correct, as it also happens with the image

Op8C2. The *Op15C1* image shows almost perfectly the location, size and shape of the brain tumor. Regarding to the image *Op20C1*, some pixels of the tumor class are displayed distributed by the classification map, although it does not show tumor.

Table 5-12. PSO FoM_{Penalized} results obtained with all bands and the reduced dataset for the SVM training.

Patient ID	OA	Sensitivity				Specificity				MCC			
		NT	TT	HT	BG	NT	TT	HT	BG	NT	TT	HT	BG
Op8C1	55,3%	42,1%	73,3%	40,4%	100,0%	91,1%	71,8%	97,7%	64,0%	38,1%	41,6%	50,0%	45,1%
Op8C2	92,7%	96,9%	37,0%	88,8%	93,1%	98,0%	94,8%	99,6%	98,6%	93,5%	15,7%	91,4%	88,3%
Op12C1	89,9%	78,0%	66,8%	96,5%	99,3%	96,7%	93,9%	96,6%	98,9%	78,3%	47,5%	92,8%	95,0%
Op12C2	69,4%	75,2%	49,2%	95,1%	54,5%	75,2%	93,4%	88,3%	93,0%	46,8%	45,8%	80,0%	53,0%
Op15C1	89,6%	97,6%	66,5%	97,0%	98,9%	90,7%	99,9%	99,2%	97,1%	76,3%	76,9%	96,0%	86,4%
Op20C1	56,6%	88,7%	0,0%	79,7%	99,5%	67,2%	99,8%	99,0%	55,6%	48,2%	-3,0%	84,1%	54,1%
AVG	75,6%	79,8%	48,8%	82,9%	90,9%	86,5%	92,3%	96,7%	84,5%	63,5%	37,4%	82,4%	70,3%
AVG ¥ (Ref)	74,3%	72,0%	44,8%	82,7%	95,5%	87,7%	95,4%	96,0%	77,9%	59,4%	42,5%	81,0%	65,5%

*NT: Normal Tissue; TT: Tumor Tissue; HT: Hypervascularized Tissue; BG: Background.

¥ Average reference results (employing 128 bands with the OPF method).

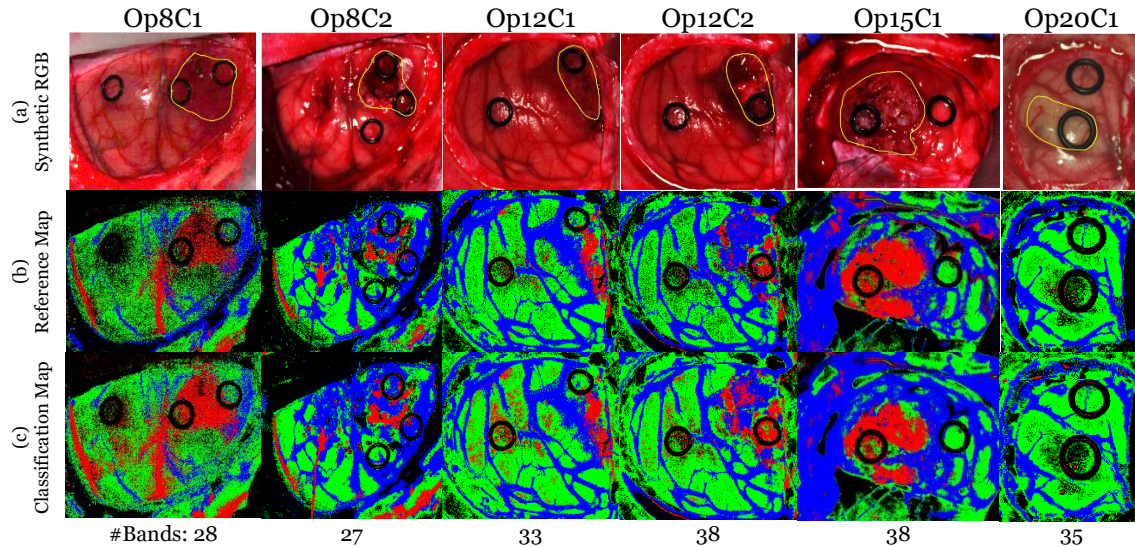


Figure 5-14. Resulting classification maps after PSO FoM_{Penalized} and the reduced dataset for the SVM training. (a) Synthetic RGB representation of the HS cube with the tumor area surrounded by a yellow line. (b) Reference classification map. (c) Classification Map

5.6 Comparison of the OPF results

Below, a comparison of the results obtained with the OPF method with the FoM and with the two best techniques selected in Section 5.4 is presented.

Figure 5-15.a shows the accuracy of the OPF reference, OPF GA and PSO, OPF GA FoM and FoM_{Penalized} and OPF PSO FoM and FoM_{Penalized}. It can be seen that, the results are very similar, but in the case of the use of OPF GA FoM, is the one that has the best accuracy with one of the images and also, the one that has the best result with its worst image. It is also visualized that the next best technique is OPF GA FoM_{Penalized}.

In the case of sensitivity of the tumor class, Figure 5-15.b shows that cases in which OPF GA are used again have a higher success rate than with the OPF PSO algorithms.

However, in this case, there is more difference between the use of OPF GA FoM and FoM_{Penalized}. Specifically, the best case of OPF GA FoM is around 98%, while OPF GA FoM_{Penalized} is only 90%. As for the worst case, all the techniques have an image (*Op20C1*) that has not been able to identify the kind of tumor.

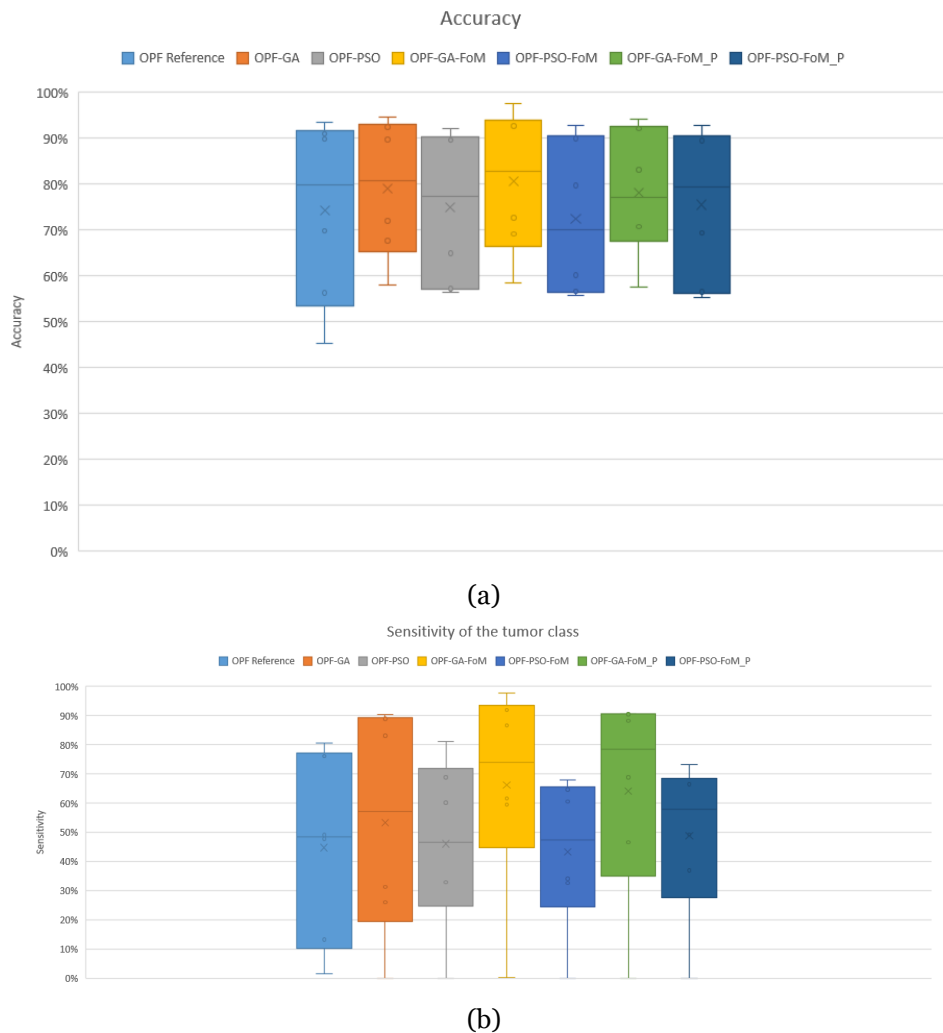


Figure 5-15. Boxplot diagram of the overall accuracy (a) and sensitivity of the tumor class (b) of all FoM evaluated techniques.

Regarding the classification maps observed in Figure 5-16, the first impression is that the results are very similar. In all the images, with the exception of the image *Op20C1*, the tumor area is detected. Analyzing the images one by one, the classification maps of the *Op8C1* image that have their best visualization, are those that use the OPF GA FoM_{Penalized} and OPF PSO FoM_{Penalized} techniques. Regarding the *Op8C2* image, the best results are observed with the same techniques. With respect to images *Op12C1* and *Op12C2*, the best results are obtained by using OPF GA FoM and OPF PSO FoM_{Penalized} techniques. The *Op15C1* image provides the best visualization in all the techniques, although the best visualization of the tumor is observed with the OPF GA FoM technique. The last image, *Op20C1*, as previously commented, no tumor is detected with any technique.

After conducting a thorough analysis, it is decided that the best techniques are the OPF GA FoM, OPF GA FoM_{Penalized} and the OPF PSO FoM_{Penalized}. These three techniques are selected because, although OPF GA FoM and FoM_{Penalized} give better results in the

graphs, the OPF PSO FoM_{penalized} technique in the classification maps gives very good results. Until now, the process that has been followed is to evaluate each of the images with their best bands. In the next section, the best cases are selected and all images are evaluated with the same bands.

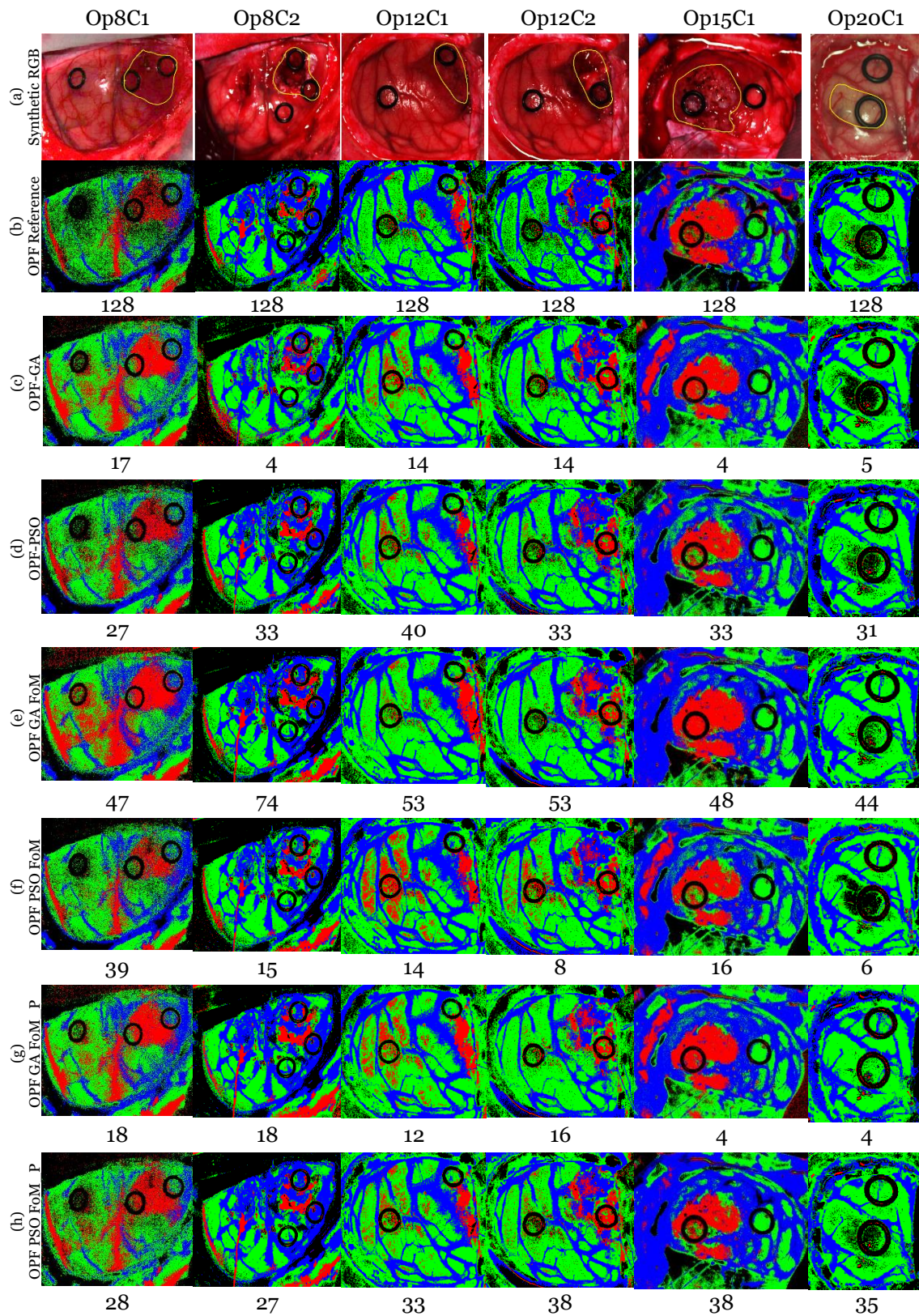


Figure 5-16. Classifications maps of the test dataset. (a) Synthetic RGB images with a yellow line determining the area tumor. (b) OPF Reference. (c and d) OPF GA and PSO (e) OPF GA FoM. (f) OPF PSO FoM. (g) OPF GA FoM_{Penalized}. (h) OPF PSO FoM_{Penalized}.

5.7 Coincident selected bands evaluation

In this section, all test images are evaluated employing the same selected bands. The techniques that were selected to identify the most representative bands are the OPF with GA using the FoM and the FoM_{Penalized} for the evaluation and the OPF with PSO using the FoM_{Penalized}. When these algorithms selected the bands, they identified different bands for each test image. The process followed in this section is to first evaluate all the bands together that were selected in all the test images (level 1 – L1), then evaluate the bands that were repeated in at least two images (level 2 – L2), then evaluate the bands that were repeated in at least three images (level 3 – L3) and thus successively until reach the possible six coincidences. This methodology was already explained in Section 4.2.7.

5.7.1 OPF with GA using FoM evaluation

Table 5-13 shows the average and the standard deviation results of the images at different band levels. In this case, it can be observed that the best **OA** is obtained in level 4 (L4) with 77.3%, closely followed by L2 and L3 with 76%. In terms of **sensitivity**, if only the tumor class is observed, L5 is the one that has the best result with 61.8%, however in this level, the sensitivity of the hypervascularized class is quite low (40.5%). Then it is followed by L4 and L3 with 52.9% and 50.6%, respectively. The **specificity** remains constant except for the last level, which worsens in the hypervascularized class. Finally, the **MCC** as in the specificity, the results remain constant except for levels 5 and 6, giving as a worse result the normal tissue class with a 22.8 and a -18.3 respectively.

Figure 5-17 illustrates the **classification maps** of all the test images after the evaluation of the different levels. It can be seen that in the last levels (L5 and L6), the initial form of the image is not clearly shown and it has a large number of misclassifications when identifying the different classes. Regarding the rest of the levels, the one that best shows the classification maps is L4, where the brain tumors are well delineated in almost all the cases. It should be noted that at L4, a few tumor pixels in the *Op20C1* image are detected correctly.

After this analysis of all the metrics, it was determined that the best case obtained in this method is L4 that is composed by 27 bands.

Table 5-13. Average and standard deviation of accuracy, sensitivity, specificity and MCC using GA FoM of all images.

Level (#bands)	OA AVG (STD) %	Sensitivity AVG(STD)%				Specificity AVG(STD)%				MCC AVG(STD)%			
		NT	TT	HT	BG	NT	TT	HT	BG	NT	TT	HT	BG
L1(121)	74.4 (20.7)	72.7 (23.3)	45.4 (30.9)	82.4 (22.5)	95.4 (8.7)	88.1 (11.7)	95.3 (8.2)	95.9 (6.8)	77.3 (21.9)	60.0 (28.2)	42.5 (31.5)	80.6 (18.5)	65.7 (21.5)
L2(102)	76.0 (19.3)	78.0 (22.6)	47.4 (31.1)	83.3 (20.5)	95.0 (9.6)	87.6 (13.3)	95.3 (8.5)	95.9 (6.6)	81.5 (19.0)	63.7 (25.4)	43.7 (31.6)	81.2 (17.4)	70.0 (21.0)
L3(62)	76.3 (17.2)	81.6 (18.8)	50.6 (29.6)	83.2 (21.5)	91.6 (16.6)	85.6 (14.3)	94.3 (8.5)	96.3 (6.1)	85.0 (16.1)	64.3 (23.7)	42.1 (29.2)	82.0 (16.9)	70.4 (20.9)
L4(27)	77.3 (16.5)	84.4 (15.2)	52.9 (31.1)	83.4 (21.7)	89.8 (21.1)	87.4 (10.4)	93.4 (8.2)	96.9 (5.0)	85.7 (20.7)	69.1 (19.1)	41.5 (30.9)	82.9 (16.6)	71.3 (22.1)
L5(5)	55.3 (21.0)	56.6 (38.1)	61.8 (38.9)	40.5 (28.1)	90.2 (18.2)	70.7 (13.6)	73.7 (28.7)	96.0 (6.0)	77.5 (18.8)	22.8 (42.3)	30.4 (26.3)	42.2 (31.3)	63.9 (23.3)
L6(2)	36.7 (21.1)	11.4 (15.9)	48.7 (28.3)	50.7 (34.0)	70.8 (44.3)	73.8 (15.6)	61.6 (37.5)	59.5 (34.0)	87.6 (16.2)	-18.3 (22.9)	11.4 (28.3)	13.5 (39.1)	55.7 (46.6)

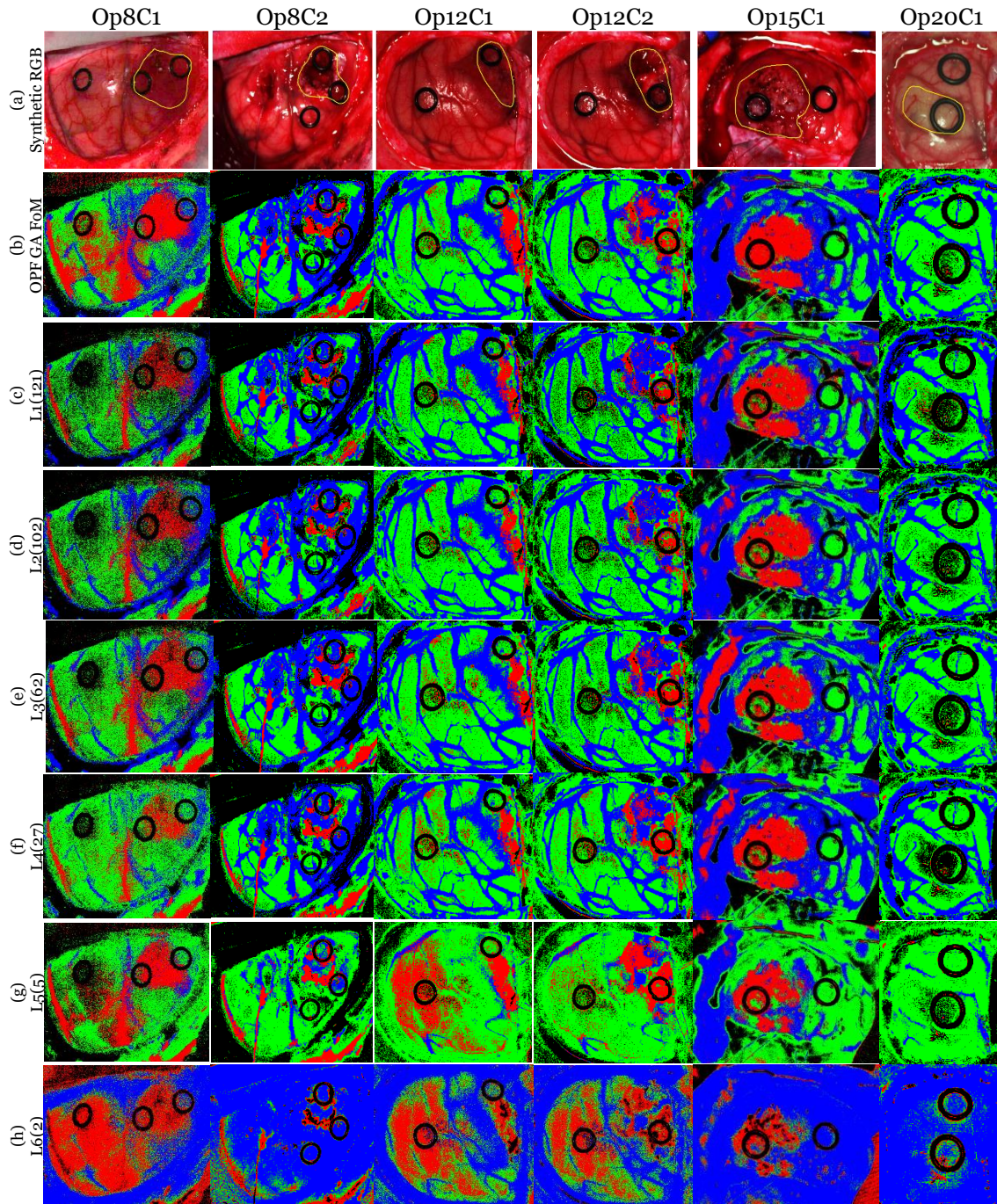


Figure 5-17. Classifications maps of the test dataset using the selected bands by the GA FoM technique

5.7.2 OPF with GA using $FoM_{Penalized}$ evaluation

In this case, the number of levels is only three, because some bands are only repeated in a maximum of three images.

Table 5-14 shows the results obtained using the OPF method with GA and the $FoM_{Penalized}$ for the evaluation of the different coincidence levels. In this case, the number of levels is only three, because some bands are only repeated in a maximum of three images. These results are the mean and standard deviation of the six test images. In terms of **OA**, it is observed that the best result was obtained in L1, with 77.9%, followed very closely by L2 with 77.0%. However, L3 worsens notably the results, achieving only a 54%.

With respect to **sensitivity**, L1 and L2 remain practically the same for all classes. Nevertheless, L3 worsens, especially in the normal tissue class and in the hypervascularized class. The **specificity** follows the same line as in sensitivity, L1 and L2 with similar results and L3 bear off from these results in the normal tissue class and in the tumor class. Regarding the **MCC** metric, it shows that the tumor class is the most affected, with 44.4% in L1 and L2, and 23.6% in level 3. This last level also worsens considerably in normal tissue and hypervascularized classes.

Regarding to the classification maps, Figure 5-18 shows all the test images in the different levels, where it is observed that L3 provides many faults, as for example in the images *Op12C1* and *Op12C2*, which shows a large number of tumor pixels (left side). Regarding L1 y L2, the results are very similar, where the only difference is found in L2, which shows the image *Op12C1* many pixels that are false positives.

After this analysis, all the metrics in L1 and L2 give the same results. So it is decided to choose L1 as the best case due to this level has less false positives in *Op12C1*.

Table 5-14. Average and standard deviation of accuracy, sensitivity, specificity and MCC using GA FoM_{Penalized} Of all images.

Level (#bands)	OA AVG (STD) %	Sensitivity AVG(STD)%				Specificity AVG(STD)%				MCC AVG(STD)%			
		NT	TT	HT	BG	NT	TT	HT	BG	NT	TT	HT	BG
L1(48)	77.9 (17.0)	85.1 (17.6)	52.7 (29.8)	83.5 (20.9)	92.5 (14.2)	87.3 (12.2)	94.6 (8.3)	96.7 (5.1)	85.3 (18.0)	69.0 (21.0)	44.4 (30.9)	82.4 (16.7)	72.7 (20.2)
L2(22)	77.0 (16.8)	83.7 (19.9)	57.0 (32.6)	81.9 (23.0)	90.1 (20.1)	85.2 (13.4)	91.2 (14.4)	97.1 (4.9)	87.7 (17.6)	65.5 (21.8)	44.4 (29.1)	81.8 (16.9)	74.7 (21.1)
L3(2)	53.8 (21.2)	52.8 (42.6)	57.6 (36.5)	48.8 (26.4)	84.8 (27.1)	72.9 (13.2)	70.3 (30.8)	93.1 (8.0)	80.0 (21.1)	20.4 (45.4)	23.6 (23.6)	45.5 (29.1)	61.4 (28.8)

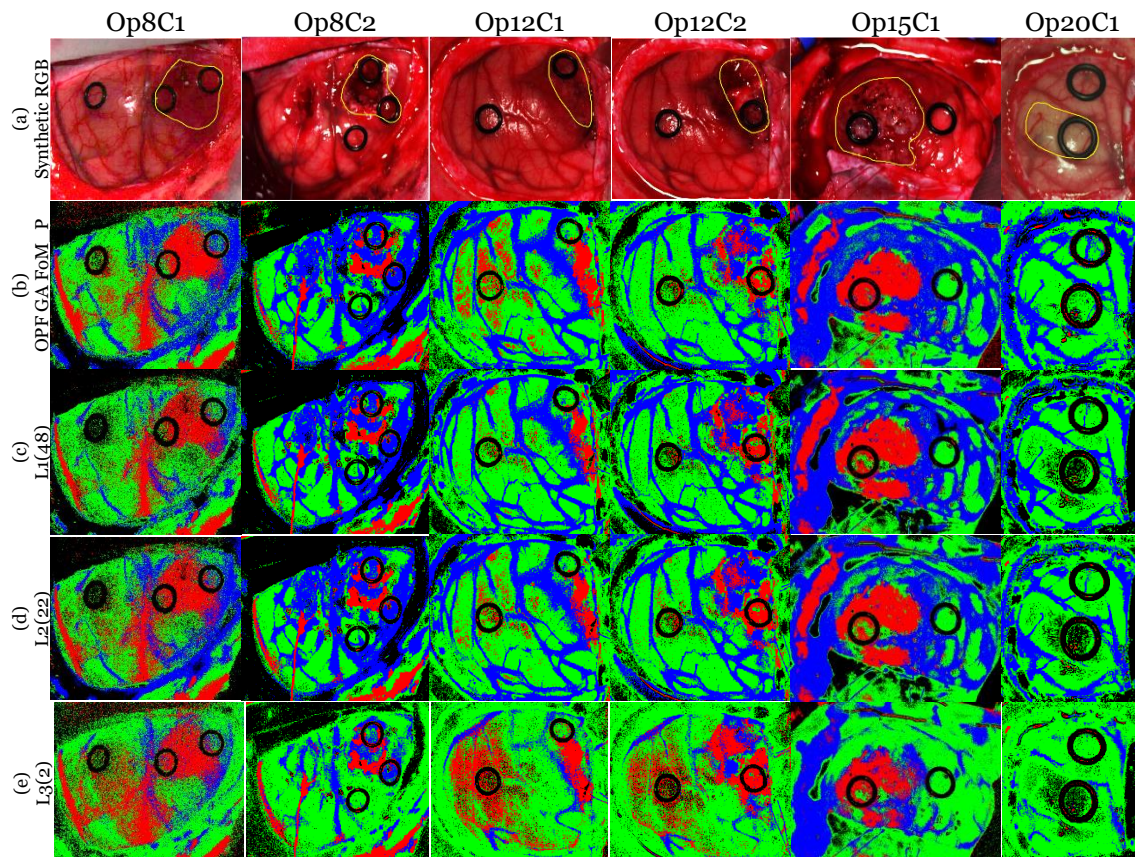


Figure 5-18. Classifications maps of the test dataset using the selected bands by the GA FoM_{Penalized} technique.

5.7.3 OPF with PSO using FoM_{Penalized} evaluation

Table 5-15 the results obtained in this experiment where the OPF method configured with the PSO is employed using the FoM_{Penalized} as the evaluation metric. In this case, as in the previous section, only three levels were found.

In the results, it can be observed that the best **OA** is obtained in the L1 with 75.9%, followed closely by L2 with 74.1%. However, L3 reaches only 58%. The **sensitivity** for all the classes of the first two levels remains practically the same and the L3 worsens in all their classes. In terms of **specificity**, the same line follows, L1 and L2 have similar results and L3 has worse results in all its classes. Finally, with respect to the **MCC** metric, the L3 is the worst result in all classes. In L1 and L2, the normal and hypervascularized tissue class are constants. However, if the rest of the classes are observed, they get worse in the second level, passing the tumor class from 38.4% to 34.3% and the background class from 72.2% to 68.7%.

Regarding the **classification maps** observed in Figure 5-19, it is observed that the L3 presents the worst results, since in the images *Op8C1* and *Op12C1* tumor is visualized in a large part of the map out of the tumor area. Analyzing the two remaining levels, they give slightly different results, although in the first level there are less false positives in the tumor class. This is observed in the images *Op8C1*, *Op12C1* and *Op12C2*, where more pixels that are erroneous are observed identifying the tumor class than in level two. Thus, taking into account each of the metrics, it was decided that the best case using the PSO is L1.

Table 5-15. Average and standard deviation of accuracy. sensitivity. specificity and MCC using PSO FoM_{Penalized} of all images.

Level (#bands)	OA AVG (STD) %	Sensitivity AVG(STD)%				Specificity AVG(STD)%				MCC AVG(STD)%			
		NT	TT	HT	BG	NT	TT	HT	BG	NT	TT	HT	BG
L1(62)	75.9 (17.3)	77.8 (22.2)	47.1 (30.6)	84.5 (20.1)	93.1 (13.0)	87.0 (13.3)	92.9 (11.5)	95.9 (5.7)	84.6 (17.2)	62.5 (19.5)	38.4 (27.7)	82.1 (17.4)	72.2 (19.9)
L2(28)	74.1 (16.9)	73.8 (23.4)	47.8 (28.7)	83.7 (21.5)	91.6 (16.1)	88.9 (88.5)	91.1 (10.7)	96.5 (5.2)	82.1 (22.3)	61.3 (20.0)	34.3 (27.4)	82.5 (16.9)	68.7 (23.1)
L3(4)	57.6 (18.6)	59.4 (29.2)	42.3 (23.9)	69.4 (29.3)	77.6 (33.5)	74.7 (16.1)	84.5 (18.4)	84.1 (11.9)	79.5 (26.3)	30.7 (29.1)	22.5 (30.7)	49.3 (28.0)	52.6 (32.1)

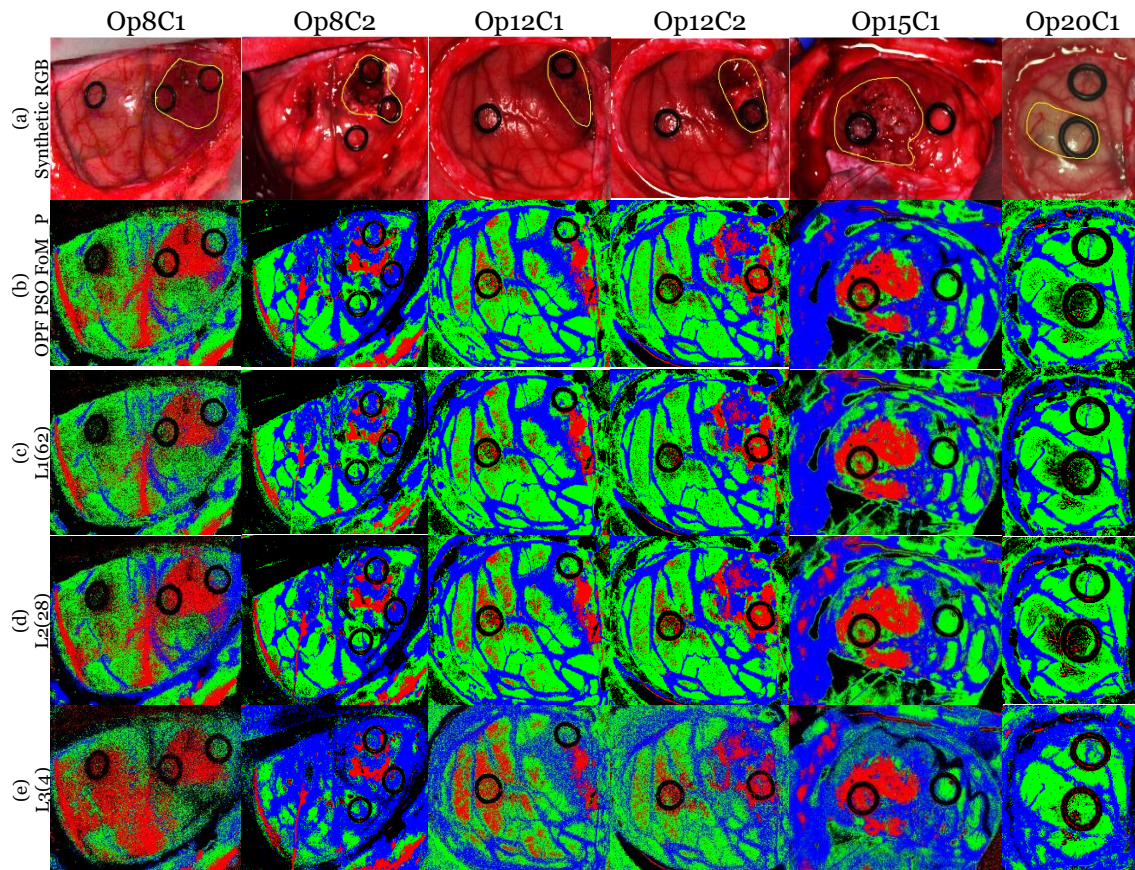


Figure 5-19. Classifications maps of the test dataset using the selected bands by the PSO FoM penalized technique.

5.7.4 Comparison of the coincident selected bands results

Once selected the best cases of the combinations developed for the band selection algorithms, we made a brief comparison and identified the best case of the three methodologies.

The quantitative results obtained are shown in Table 5-16. In this case it is observed that the results of the **OA** are similar, giving the best case to the OPF-GA-FoM_{Penalized} with 77.9% and the worst case to the OPF-PSO-FoM_{Penalized} with 75.9%. In terms of **sensitivity**, the results of the first two cases remain constant, the only more pronounced difference is that in the tumor class, the OPF-GA-FoM achieves 52.9% and the OPF-GA-FoM_{Penalized} reaches 52.7%. The last case has worse results in the normal and tumor tissue classes, with 77.8% and 47.1%, respectively. Nevertheless, the **specificity** remains constant for all cases. Finally, the **MCC** metric shows that the class with the worst result is the tumor class, with the second case having the best result, with 44.4% and the third case having the worst result with 38.4%.

Regarding the **classification maps** shown in Figure 5-20, it is observed as the first impression that the results in all cases are very similar. Analyzing the images one by one, in the case of the first image, *Op8C1*, it is observed that using either the OPF-GA-FoM or the OPF-PSO-FoM_{Penalized} the results are more accurate with less false positives. The best cases that visualizes the image *Op8C2* is the OPF-GA-FoM and OPF-GA-FoM_{Penalized}, since it is observed in the area of the tumor, a higher number of tumor pixels. As for the images *Op12C1* and *Op12C2*, the classification maps of the OPF-GA-FoM_{Penalized} has less false positives of the tumor class. With respect to the *Op15C1* image, it is the one with the

greatest changes among the cases. The OPF-GA-FoM clearly shows where the tumor is located, although it has a small group of false positives of the tumor class in the upper left image. The OPF-GA-FoM_{Penalized}, gives practically the same classification map as the previous case, although the group of false positives is higher. In the case of the OPF-PSO-FoM_{Penalized}, that group of false positives disappears, but also pixels of the tumor class where the tumor is found are lost. Finally, the image *Op20C1* gives practically the same result in all three cases, although OPF-GA-FoM correctly shows some pixels of the tumor class.

After this analysis, it is worth noting that OPF-GA-FoM and OPF-GA-FoM_{Penalized} are the ones that give the best results, being practically the same. Having to choose one of the cases, after a general balance of the metrics, it is decided that the OPF-GA-FoM_{Penalized} is the most complete case using 48 bands.

Table 5-16. Best cases average and standard deviation of accuracy. sensitivity. specificity and MCC.

Technique (#bands)	OA AVG (STD)%	Sensitivity AVG(STD)%				Specificity AVG(STD)%				MCC AVG(STD)%			
		NT	TT	HT	BG	NT	TT	HT	BG	NT	TT	HT	BG
GA-FoM (27)	77.3 (16.5)	84.4 (15.2)	52.9 (31.1)	83.4 (21.7)	89.8 (21.1)	87.4 (10.4)	93.4 (8.2)	96.9 (5.0)	85.7 (20.7)	69.1 (19.1)	41.5 (30.9)	82.9 (16.6)	71.3 (22.1)
GA-FoM_{Pen} (48)	77.9 (17.0)	85.1 (17.6)	52.7 (29.8)	83.5 (20.9)	92.5 (14.2)	87.3 (12.2)	94.6 (8.3)	96.7 (5.1)	85.3 (18.0)	69.0 (21.0)	44.4 (30.9)	82.4 (16.7)	72.7 (20.2)
PSO-FoM_{Pen} (62)	75.9 (17.3)	77.8 (22.2)	47.1 (30.6)	84.5 (20.1)	93.1 (13.0)	87.0 (13.3)	92.9 (11.5)	95.9 (5.7)	84.6 (17.2)	62.5 (19.5)	38.4 (27.7)	82.1 (17.4)	72.2 (19.9)

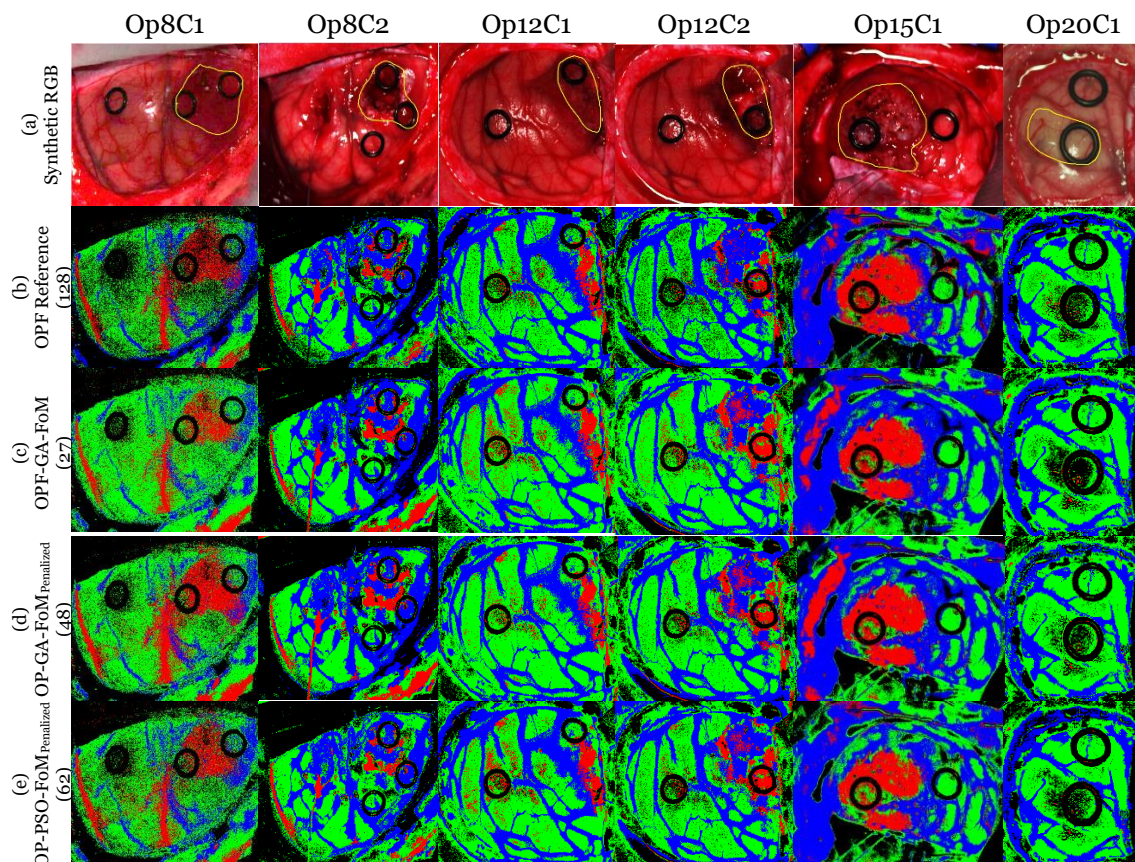


Figure 5-20. Best cases classifications maps. (a) Synthetic RGB images with a yellow line determining the area tumor. (b) OPF Reference. (c and d) OPF GA FoM and FoM_{Penalized} and (e) OPF PSO FoM_{Penalized}.

5.8 Band selection evaluation using ACO algorithm

This section will present the results obtained with the band selection methodology based on the ACO algorithm. This algorithm is evaluated independently due to its structure and work procedure is different from the other two optimization algorithms.

The experimental procedure carried out is as follows: Initially, the first 20 most important bands, which were identified by the ACO algorithm, were selected and evaluated with the entire and reduced training database. Then, once the results were compared, it was selected which method offered the best result and the six test images were then evaluated with the coincident bands.

5.8.1 ACO with the entire training dataset

Table 5-17 shows the results obtained with the band selection procedure with each image independently using the entire training dataset to obtain the most relevant bands. It is observed that the average **OA** obtained is 74.8%. **Sensitivity** is high in all classes with the exception of the tumor class, with 19.6%. It is worth noticing that the images *Op12C1*, and *Op20C1* were not been able to detect any pixel of this class correctly. In terms of **specificity**, the results are high, except for the normal tissue class, which only reaches 76%. Finally, the class with the worst result in the **MCC** metric is again the tumor class with 18.7%. This class has a very small success rate in all images with the exception of the *Op15C1* image.

On the other hand, Figure 5-21 shows the **classification maps** of all the images. *Op8C1*, *op12C1*, *Op12C2* and *Op20C1* show no tumor in the resulting map. Only the image *Op15C1* clearly shows the location of the tumor, although it has false positives on the left side of the classification map.

Table 5-17. Accuracy, sensitivity, specificity and MCC results using the entire dataset with ACO.

Patient ID	OA	Sensitivity				Specificity				MCC			
		NT	TT	HT	BG	NT	TT	HT	BG	NT	TT	HT	BG
Op8C1	54.4%	62.1%	20.9%	50.5%	100.0%	69.8%	86.5%	85.4%	70.1%	31.9%	9.1%	38.3%	52.1%
Op8C2	94.0%	98.2%	31.2%	97.3%	93.4%	97.5%	96.6%	99.8%	98.1%	93.2%	16.5%	97.2%	88.6%
Op12C1	91.3%	97.9%	0.0%	95.3%	99.6%	90.1%	100.0%	97.6%	99.1%	83.5%	-0.3%	92.4%	96.0%
Op12C2	64.8%	93.2%	2.8%	85.5%	51.5%	62.3%	99.9%	82.7%	96.1%	50.9%	13.2%	65.1%	55.0%
Op15C1	86.7%	96.5%	62.7%	93.8%	97.6%	86.8%	100.0%	99.9%	97.0%	69.0%	74.4%	93.1%	85.7%
Op20C1	57.6%	95.8%	0.0%	77.1%	100.0%	50.0%	100.0%	99.3%	91.9%	36.89%	-0.9%	82.9%	91.4%
AVG	74.8%	90.6%	19.6%	83.2%	90.4%	76.1%	97.1%	94.1%	92.1%	60.9%	18.7%	78.2%	78.1%
AVG ¥ (Ref)	73.9%	93.1%	17.1%	82.6%	89.2%	73.4%	97.5%	94.7%	94.8%	59.7%	24.9%	78.0%	81.2%

* NT: Normal Tissue; TT: Tumor Tissue; HT: Hypervascularized Tissue; BG: Background.

¥ Average reference results (employing 128 bands with the BPF method).

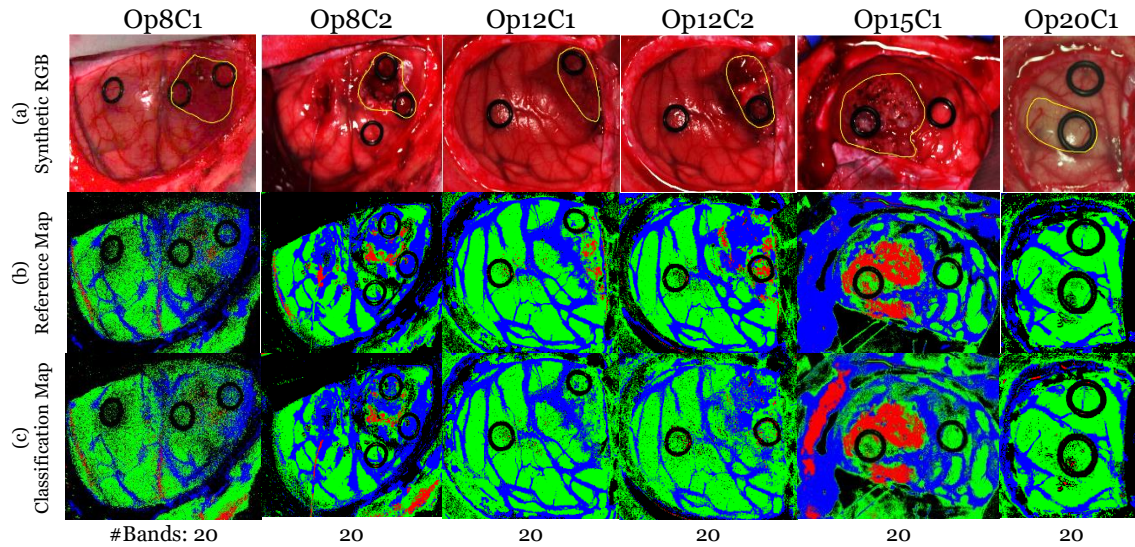


Figure 5-21. Resulting classification maps after ACO and the entire dataset for the SVM training. (a) Synthetic RGB representation of the HS cube with the tumor area surrounded by a yellow line. (b) Reference classification map. (c) Classification Map.

5.8.2 ACO with the reduced training dataset

After the evaluation of the results using the entire dataset, the same procedure is performed again with the reduced dataset. In this case, Table 5-18 shows that the average **OA** does not exceed 70%, although in two images an OA of more than 92% is achieved. In terms of **sensitivity**, the tumor class is the lowest with respect to the rest with 44%. However, respect to the previous method where the entire training dataset is employed, the tumor class accuracy has an improvement of 24.4%. Similarly, to the previous case, the image *Op20C1* does not identify any pixel of tumor class. Regarding to the **specificity**, the results are high, giving the worst result to the background class with 82.3%. Finally, with respect to **MCC**, the tumor class has the worst result, with 26.8%, where only one image, *Op15C1*, has a success rate of 88% and the rest of images does not exceed 23%.

Regarding the classification maps of the obtained for each test image shown in Figure 5-22, with the exception of the image *Op20C1*, they show a large number of tumor pixels. Specifically, the images *Op8C1* and *Op12C1* show more pixels of the erroneous tumor class than correct ones. The remaining images, *Op8C2*, *Op12C2* and *OpC1*, although they also have pixels that indicate tumor where it is not correct, there is a greater number of correct pixels of that class.

Table 5-18. Accuracy, sensitivity, specificity and MCC results using the reduced dataset with ACO.

Patient ID	OA	Sensitivity				Specificity				MCC			
		NT	TT	HT	BG	NT	TT	HT	BG	NT	TT	HT	BG
Op8C1	42.3%	26.4%	48.0%	37.3%	100.0%	85.1%	64.8%	92.8%	48.7%	14.1%	12.1%	37.4%	35.7%
Op8C2	92.4%	97.5%	33.3%	87.3%	92.6%	98.7%	94.0%	99.7%	98.5%	95.4%	12.6%	91.0%	87.5%
Op12C1	71.1%	9.7%	75.1%	97.1%	99.2%	98.3%	71.5%	94.8%	99.7%	18.5%	22.9%	90.9%	98.7%
Op12C2	59.3%	76.8%	24.5%	95.1%	33.8%	61.2%	93.4%	78.4%	95.2%	34.7%	22.9%	70.2%	38.2%
Op15C1	93.3%	97.0%	83.2%	96.2%	99.0%	94.1%	99.9%	100.0%	98.0%	82.6%	88.4%	96.0%	89.6%
Op20C1	57.7%	92.1%	0.0%	82.1%	99.8%	72.1%	99.9%	98.6%	53.9%	56.4%	-2.23%	85.0%	52.2%
AVG	69.3%	66.6%	44.0%	82.5%	87.4%	84.9%	87.2%	94.1%	82.3%	53.4%	26.8%	78.4%	67.0%
AVG Y (Ref)	74.3%	72.0%	44.8%	82.7%	95.5%	87.7%	95.4%	96.0%	77.9%	59.4%	42.5%	81.0%	65.5%

*NT: Normal Tissue; TT: Tumor Tissue; HT: Hypervascularized Tissue; BG: Background.
 Y Average reference results (employing 128 bands with the OPF method).

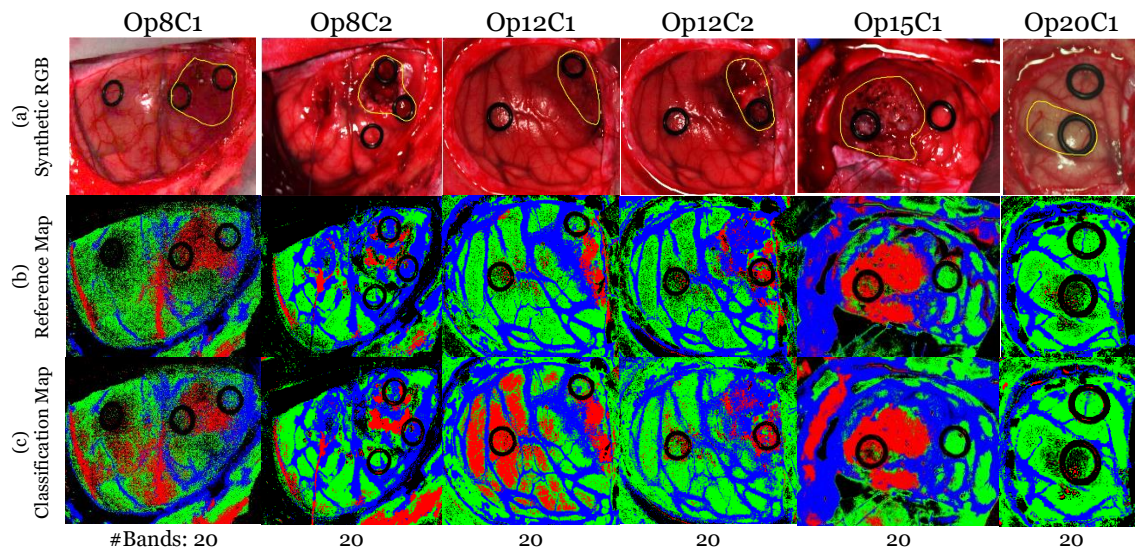


Figure 5-22. Resulting classification maps after ACO and the reduced dataset for the SVM training. (a) Synthetic RGB representation of the HS cube with the tumor area surrounded by a yellow line. (b) Reference classification map. (c) Classification Map

5.8.3 Coincident selected bands evaluation using ACO

After analyzing the results obtained with the ACO algorithm, it was decided that the best results were obtained with the reduced training dataset. Therefore, as in section 5.7, the test images were evaluated again but using the coincident bands in the different levels. In this case, the bands were repeated in four images, generating four levels to be evaluated.

Table 5-19 shows the average results and standard deviation of the different levels. In this case, the best case of **OA** is obtained in L1, with 76.4%, although L2 has a slightly lower **OA**, specifically with 73.7%. In the **sensitivity**, for all levels, the class with the worst rate of success is the tumor class. Observing this class, L1 is the one that achieves the best result (47.6%), followed very closely by L2. In terms of **specificity**, the results remain constant, with the exception of the normal and tumor tissue classes of the last level 61.2% and 43.9%, respectively. In the **MCC** metric, it can be observed again that

the tumor class has the worst result at all levels, reaching in the last level to -20.4% accuracy.

With respect to the maps observed in Figure 5-23, L3 and L4 produce many errors when identifying the different classes. Regarding L1 and L2, classification maps improve and provide similar results. If these classification maps are observed in detail, it is visualized that the images *Op12C1* and *Op12C2* of L1 have greater precision than in L2. In L2, there is a greater number of false positives for the tumor class (left side of the classification maps).

Taking into account all the metrics, it was decided that the best case is to use L1, that is, all the bands that were selected among the six images (81 bands).

Table 5-19. Average and standard deviation of accuracy, sensitivity, specificity and MCC using ACO.

Level (#bands)	OA AVG (STD) %	Sensitivity AVG(STD)%				Specificity AVG(STD)%				MCC AVG(STD)%			
		NT	TT	HT	BG	NT	TT	HT	BG	NT	TT	HT	BG
L1(81)	76.4 (18.7)	80.2 (22.8)	47.6 (26.2)	83.6 (21.1)	94.3 (9.5)	87.4 (14.7)	93.8 (10.1)	96.6 (4.7)	83.8 (18.1)	65.3 (24.4)	40.7 (29.7)	82.1 (18.4)	71.8 (19.5)
L2(32)	73.7 (18.9)	77.3 (24.2)	42.9 (27.6)	83.5 (22.4)	91.2 (17.1)	85.2 (14.3)	91.0 (11.1)	95.8 (6.0)	84.8 (20.7)	60.2 (24.09)	29.4 (28.2)	81.0 (20.0)	72.2 (22.0)
L3(6)	62.9 (19.0)	65.2 (36.1)	30.1 (27.1)	71.2 (32.4)	87.6 (25.0)	82.3 (14.5)	77.9 (20.7)	90.1 (11.9)	84.0 (23.6)	45.9 (32.3)	5.0 (18.4)	64.7 (25.9)	70.3 (25.8)
L4(1)	37.7 (23.9)	65.9 (34.8)	38.6 (35.0)	24.5 (32.1)	25.8 (37.2)	61.2 (38.5)	43.9 (27.6)	77.5 (30.6)	81.4 (27.0)	25.5 (41.0)	-20.4 (37.0)	-3.3 (30.2)	10.8 (49.8)

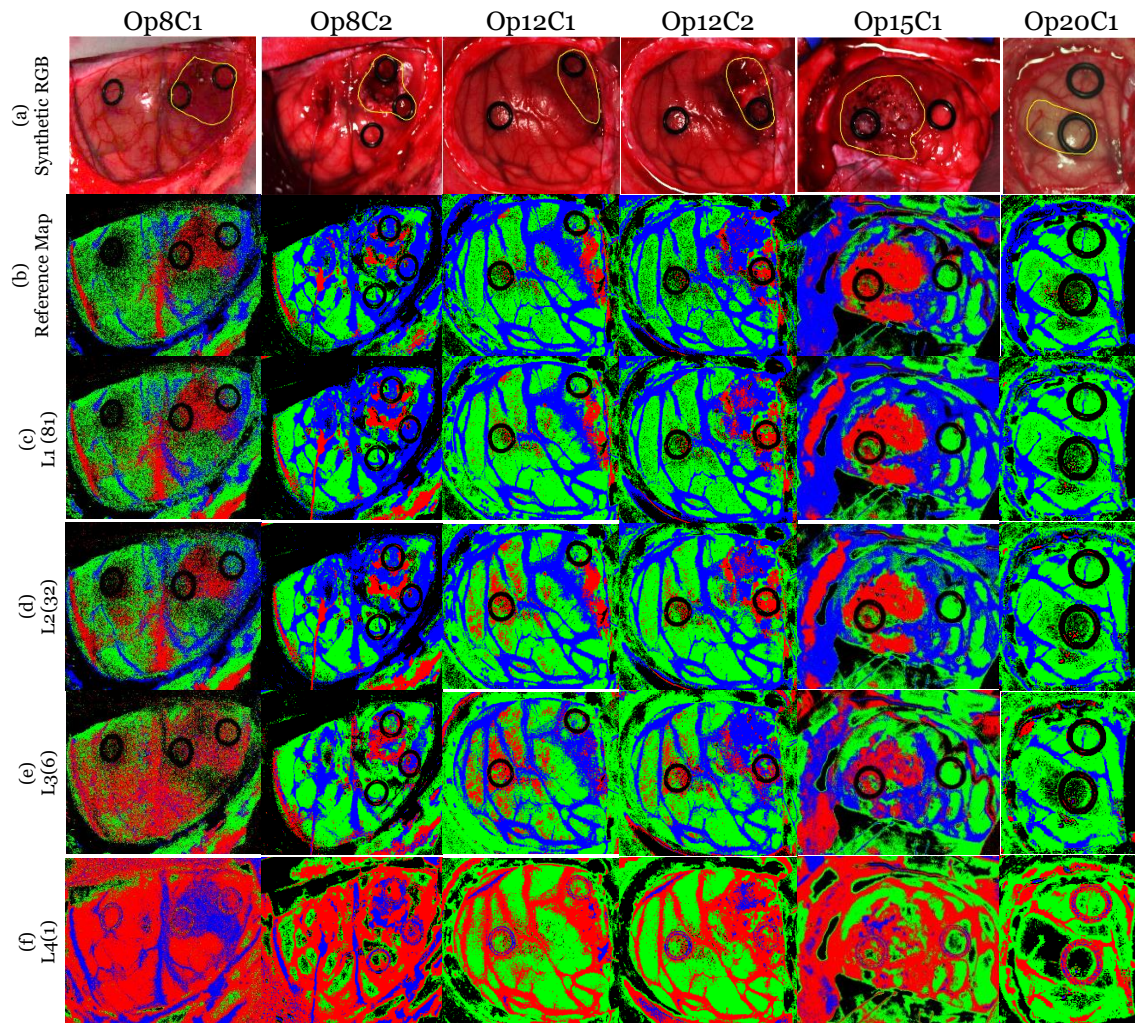


Figure 5-23. Classifications maps of the test dataset using the selected bands by the ACO algorithm.

5.9 Summary

This chapter has showed the results obtained when selecting the bands that provide more information when classifying HS brain images for the detection and delineation of brain tumors. This selection process was divided into different methodologies, increasing the success rate of the results after the use of the reduced training dataset. First, the GA and PSO algorithms were evaluated having as a condition for the band selection the $OA_{\text{Penalized}}$ metric. From the best results obtained in these evaluations, these algorithms were re-evaluated having as a condition for the band selection the FoM and the $FoM_{\text{Penalized}}$ metrics in order to take into account the balance of the sensitivity (accuracy per class) results. After selecting the best cases, a new evaluation of the test images was performed using the coincident bands obtained for all the test images in the previous independent evaluations. This analysis was performed in different levels. In this case, the best case obtained was the use of the GA using the $FoM_{\text{Penalized}}$ (48 bands) with the coincident bands in at least one image, providing a 77.9% of **OA** and a tumor **sensitivity** of 52.7%.

Once it was decided which was the best case (OPF-GA- $FoM_{\text{Penalized}}$), another optimization algorithm was analyzed. This algorithm, ACO, was evaluated independently since it follows a different structure compared with the other algorithms. However, the

process followed was the same. First, the bands that the ACO selected with the entire and reduced dataset were evaluated. Then, it was decided which case gave the best performance, and the coincident bands were evaluated for all the test images at different levels. In this case, the best result was obtained in the L1 (81 bands). This means that all the bands that the ACO had selected for each HS test image independently were used, providing 76.4% of **OA** and a tumor **sensitivity** of 47.6%.

Analyzing these two results, the best of these cases is the OPF-GA-FoM_{Penalized} method as it provided better quantitative and qualitative results employing only 48 bands. Table 5-20 shows the results of all the images after evaluating the OPF-GA-FoM_{Penalized} L1, the average values of all the patients of the results and the average values of the reference results. It can be seen that the **OA** improves 3.6% with respect to the reference results, giving in the images Op8C2, Op12C1 and Op15C1 the best results with 92.6%, 93.3% and 91.5% respectively. In terms of **sensitivity**, the tumor class has the lowest result, specifically 52.7%, although it improves by almost 8% compared to the reference ones. The worst cases are with the Op12C2 image (35.7%) and with the Op20C1 image (0.0%). The **specificity** has good results in all classes, and has similar results with reference with the exception of the background class, which improves by 7%. As in sensitivity, the metric **MCC** tumor class exhibits the worst result, specifically 44.4%. This result is slightly higher than the reference ones (42.5%).

Figure 5-24 illustrates the **classifications maps** of the OPF-GA-FoM_{Penalized}. Looking at all the images one by one, in the Op8C1 image, it is observed that there are more false positives of the tumor class with respect to the reference map, in the Op8C2 image, it shows more true positives of the tumor class than the reference one, although it also has more false positives. In the cases of the Op12C1 and Op12C2 images, both images have more true positives of the tumor class and less false positives of said class by the classification map. The Op15C1 image shows a greater number of false positives on the upper left side, and the Op20C1 image does not show tumor.

Figure 5-25 shows the spectral signatures of the healthy tissue (green color), the tumor tissue (red color), the hypervascularized tissue (blue color) and the final bands that have been selected. It can be seen that the bands are mainly grouped into small groups throughout the spectral signature. These are some of the groups of the bands: 1-8, 17-20, 33-38, 43-49, 55-63, 72-81 and 123-128, that correspond to 440.5-465.96 nm, 498.71-509.62 nm, 556.91-575.1 nm, 593.29-615.12 nm, 636.94-666.05 nm, 698.79-731.53 nm and 884.32-902.51 nm.

Table 5-20. Accuracy, sensitivity, specificity and MCC results using OPF-GA-FoM^{Penalized} L1.

Patient ID	OA	Sensitivity				Specificity				MCC			
		NT	TT	HT	BG	NT	TT	HT	BG	NT	TT	HT	BG
Op8C1	58.7%	50.4%	70.2%	42.8%	100.0%	90.3%	78.3%	96.8%	66.5%	44.3%	45.9%	50.5%	46.5%
Op8C2	92.6%	95.2%	60.1%	87.8%	93.1%	99.3%	94.1%	99.7%	97.4%	95.3%	24.7%	91.2%	87.4%
Op12C1	93.3%	91.7%	74.3%	94.8%	99.3%	95.2%	98.2%	98.2%	98.8%	86.1%	71.1%	92.5%	94.5%
Op12C2	74.3%	84.6%	35.7%	98.2%	63.9%	81.3%	97.1%	86.6%	92.9%	61.9%	43.4%	79.7%	60.9%
Op15C1	91.5%	98.4%	75.8%	96.1%	98.6%	91.9%	99.9%	100.0%	98.0%	79.0%	83.3%	95.8%	89.7%
Op20C1	57.2%	90.0%	0.0%	81.2%	100.0%	65.6%	99.9%	98.9%	58.5%	47.5%	-1.9%	84.9%	57.2%
AVG	77.9%	85.1%	52.7%	83.5%	92.5%	87.3%	94.6%	96.7%	85.3%	69.0%	44.4%	82.4%	72.7%
AVG £ (Ref)	78.8%	93.0%	28.0%	87.4%	95.4%	82.0%	98.1%	93.3%	93.9%	68.8%	34.0%	80.3%	86.0%
AVG ¥ (Ref)	74.3%	72.0%	44.8%	82.7%	95.5%	87.7%	95.4%	96.0%	77.9%	59.4%	42.5%	81.0%	65.5%

* NT: Normal Tissue; TT: Tumor Tissue; HT: Hypervascularized Tissue; BG: Background.

¥ Average reference results (employing 128 bands with the OPF method).

£ Average reference results (employing 128 bands with the BPF method).

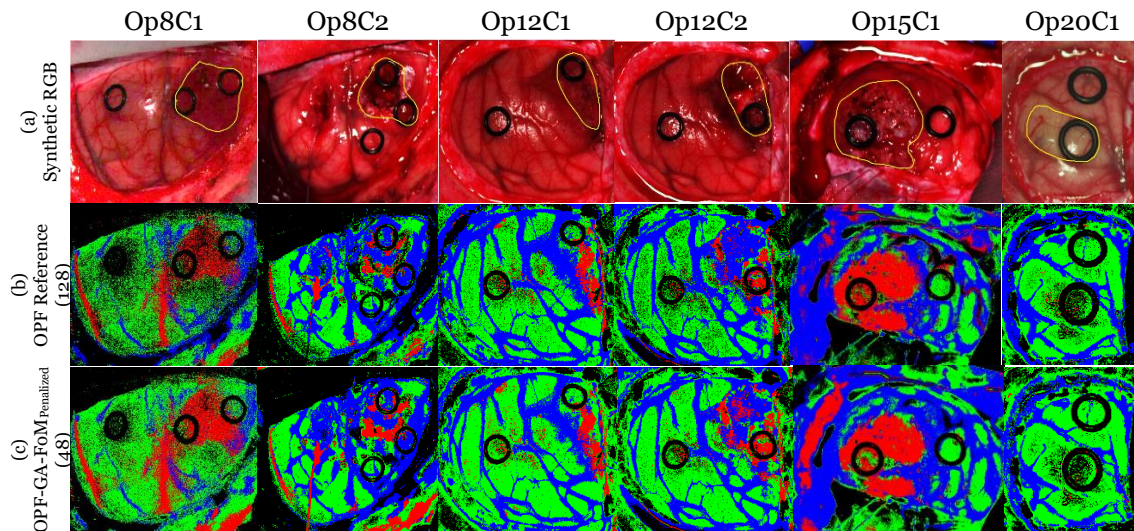


Figure 5-24. Best case classification map. (a) Synthetic RGB images with a yellow line determining the area tumor. (b) OPF Reference. (c) OPF GA FoM^{Penalized} L1.

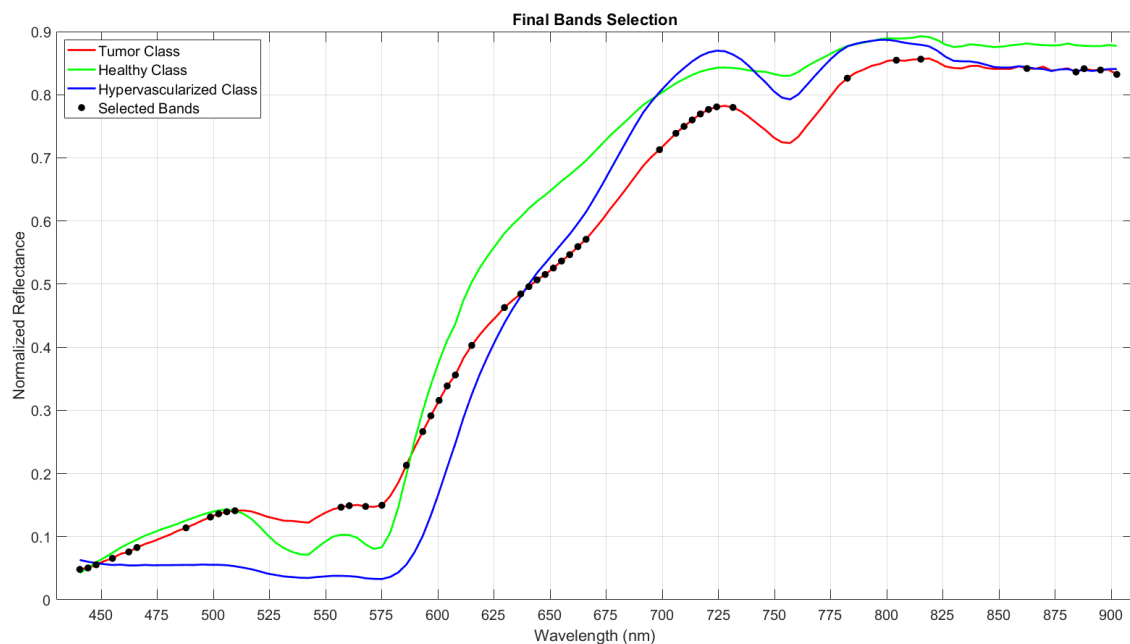


Figure 5-25. Normalized average signature of the classes and final selected bands.

Table 5-21. Accuracy, sensitivity, specificity and MCC results using OPF-GA-FoM_{Penalized} L1.

Band ID	λ (nm)	Band ID	λ (nm)								
1	440.50	18	502.34	43	593.29	56	640.58	72	698.79	95	782.46
2	444.14	19	505.98	44	596.93	57	644.22	74	706.06	101	804.29
3	447.78	20	509.62	45	600.57	58	647.86	75	709.70	104	815.20
5	455.05	33	556.91	46	604.20	59	651.50	76	713.34	117	862.49
7	462.33	34	560.55	47	607.84	60	655.13	77	716.98	123	884.32
8	465.96	36	567.83	49	615.12	61	658.77	78	720.62	124	887.96
14	487.79	38	575.10	53	629.67	62	662.41	79	724.25	126	895.23
17	498.71	41	586.01	55	636.94	63	666.05	81	731.53	128	902.51

Chapter 6: Conclusions & Future Lines

6.1 Conclusions

In accordance with the objectives of this Master Thesis, the use of different optimization algorithms for the selection of the most representative bands in the identification of brain tumors has been evaluated. For this work, the HS images described in Chapter 3 were used with the aim of identifying the bands that allow differencing between the different tissues within the VNIR range of the electromagnetic spectrum.

The SVM classifier was used to evaluate the bands selected by the optimization algorithms following a leave-one-patient-out cross-validation. The optimization algorithms employed were the GA, the PSO and the ACO. With the GA and PSO algorithms, several methodologies were performed. First, the bands were selected after using the entire dataset, optimizing the $OA_{\text{Penalized}}$ metric (BPF method). This methodology was assessed with 30 and 60 generations. Then, due to the large execution times (~ 3 hours per test image with 60 generations), and with the additional goal of evaluating a reduced and a balanced training dataset, the labeled dataset was reduced using a methodology based on the K-means clustering algorithm (OPF method). Once reduced, the optimization algorithms were evaluated with 60 generations, which took ~ 4 min per test image for obtaining the optimized bands.

At that time, it was observed that after evaluating the selected bands, the case that obtained the best OA was not the one that obtained the best sensitivity in the tumor class, so two new evaluation metrics (FoM and $FoM_{\text{Penalized}}$) were proposed. These metrics were employed to evaluate the OPF method. After evaluation, the best cases were selected and all the test images were evaluated employing the same selected bands. This evaluation was divided into several levels: first evaluating the test images with all the bands selected for each image together (L1), then evaluating the images with the bands repeated in at least two images (L2) and so on.

As for the ACO algorithm, it worked in a different way than the other two optimization algorithms, and it was evaluated with the complete and reduced labeled dataset. After choosing the best result, all images were evaluated with the same bands and with the same procedure as with the GA and PSO algorithms.

In Chapter 4, it was observed that the overall average sensitivity of the tumor class was not very high. With the exception of the Op20C1 image, the brain tumor was correctly identified, although with many false positives spread across the classification maps. It

was also observed that by reducing the dataset and selecting the most relevant bands, the results improved with respect to the reference ones (128 bands). After all the experiments performed, it was decided that the best case was the OPF-GA-FoM_{penalized} using the Level 1 (48 bands). The most important spectral regions identified were: 440.5-465.96 nm, 498.71-509.62 nm, 556.91-575.1 nm, 593.29-615.12 nm, 636.94-666.05 nm, 698.79-731.53 nm and 884.32-902.51 nm.

6.2 Future lines

The future work of this Master Thesis has many paths to follow. On the one hand, thanks to the ITHACA project, the amount of data in the train and test database will be increased. With this improvement, it will be able to corroborate the results obtained in this work. The increased database can be employed also to identify different tissues and tumor types, apart from delineating the boundaries of the tumor.

Another field of future research is to perform an optimization of the hyperparameters of the SVM algorithm. One way to do this could be to execute within the optimization algorithm another algorithm of the same family that will optimize the parameters of the SVM classifier each time the main algorithm selects different bands. For this purpose, the best possible prediction model could be achieved in each execution.

It would be also interesting to perform more experiments in the design of the training dataset reduction algorithm, because after performing the balance of the labeled dataset (1000 pixels per class), the results improved significantly. It is necessary to remember that, initially, this methodology was proposed as a solution to accelerate the execution time of the optimization algorithm and the improvements that it could offer have not been studied in detail in this work.

Finally, it could be also interesting to try to correlate the most representative spectral ranges, obtained in this work, with the biological properties of brain tissue, especially with the goal of differentiating the tumor and normal tissue.

References

- [1] A. A. Gowen, C. P. Donnell, P. J. Cullen, G. Downey, and J. . Frias, "Hyperspectral imaging e an emerging process analytical tool for food quality and safety control," *elsevier*, vol. 18, no. 12, pp. 590–598, May 2007.
- [2] J. Wang, X. Wang, K. Zhang, K. Madani, and C. Sabourin, "Morphological Band Selection for Hyperspectral Imagery," *IEEE Geosci. Remote Sens. Lett.*, vol. 15, no. 8, pp. 1259–1263, Aug. 2018.
- [3] P. D. Randall B. Smith, "Introduction to Hyperspectral Imaging," *Middlet. Res. Tech. Notes*, p. 24, 2012.
- [4] P. Shippert, "Introduction to Hyperspectral Image Analysis," *Earth Sci. Appl. Spec. Res. Syst. Inc.*
- [5] D. Wu and D. W. Sun, "Advanced applications of hyperspectral imaging technology for food quality and safety analysis and assessment: A review - Part I: Fundamentals," *Innovative Food Science and Emerging Technologies*, vol. 19, pp. 1–14, 2013.
- [6] J. K. Delaney *et al.*, "Visible and Infrared Imaging Spectroscopy of Picasso's Harlequin Musician : Mapping and Identification of Artist Materials in Situ," *Appl. Spectrosc.*, vol. 64, no. 6, pp. 584–594, Jun. 2010.
- [7] S. Legnaioli *et al.*, "Recovery of archaeological wall paintings using novel multispectral imaging approaches," *Herit. Sci.*, vol. 1, no. 1, p. 33, 2013.
- [8] G. Lu and B. Fei, "Medical hyperspectral imaging: a review," *J. Biomed. Opt.*, vol. 19, no. 1, p. 010901, Jan. 2014.
- [9] M. Halicek, H. Fabelo, S. Ortega, G. M. Callico, and B. Fei, "In-Vivo and Ex-Vivo Tissue Analysis through Hyperspectral Imaging Techniques: Revealing the Invisible Features of Cancer," *Cancers (Basel)*, vol. 11, no. 6, p. 756, May 2019.
- [10] P. Ghamisi, J. Plaza, Y. Chen, J. Li, and A. J. Plaza, "Advanced Spectral Classifiers for Hyperspectral Images: A review," *IEEE Geosci. Remote Sens. Mag.*, vol. 5, no. 1, pp. 8–32, Mar. 2017.
- [11] L. Van Der Maaten, E. Postma, and J. Van Den Herik, "Dimensionality Reduction: A Comparative Review," *Vis. cogn.*, vol. 12, no. 1, pp. 1–36, Jan. 2009.
- [12] R. Yang, L. Su, X. Zhao, H. Wan, and J. Sun, "Representative band selection for hyperspectral image classification," *J. Vis. Commun. Image Represent.*, vol. 48, pp. 396–403, Oct. 2017.
- [13] D. Ravi, H. Fabelo, G. M. Callico, and G. Yang, "Manifold Embedding and Semantic Segmentation for Intraoperative Guidance with Hyperspectral Brain Imaging," *IEEE Trans. Med. Imaging*, 2017.

-
- [14] M. Zamalloa, L. J. Rodríguez-Fuentes, M. Peñagarikano, G. Bordel, and J. P. Uribe, "Feature selection VS. feature transformation in reducing dimensionality for speaker recognition," *ResearchGate*, vol. 53, no. May 2014, p. 5, 2008.
- [15] D. Patra, J. Dash, C. Pradhan, and R. N. R. Parida, "Mathematical Analysis of PCA, MDS and ISOMAP Techniques in Dimension Reduction," vol. 3, no. 5, pp. 61–67, 2015.
- [16] C. O. S. Sorzano, J. Vargas, and a P. Montano, "A survey of dimensionality reduction techniques," *Nat. Cent. Biotechnol.*, pp. 1–35, Mar. 2014.
- [17] A. Buja, D. F. Swayne, M. L. Littman, N. Dean, H. Hofmann, and L. Chen, "Data Visualization With Multidimensional Scaling," *J. Comput. Graph. Stat.*, vol. 17, no. 2, pp. 444–472, Jun. 2008.
- [18] K. Sastry, D. E. Goldberg, and G. Kendall, "Genetic Algorithms," in *Search Methodologies*, Boston, MA: Springer US, 2014, pp. 93–117.
- [19] R. E. and K. Behdi, "Particle Swarm Optimization in Structural Design," in *Swarm Intelligence, Focus on Ant and Particle Swarm Optimization*, no. December, I-Tech Education and Publishing, 2007, pp. 1–24.
- [20] S. Sharma and K. M. Buddhiraju, "Spatial–spectral ant colony optimization for hyperspectral image classification," *Int. J. Remote Sens.*, vol. 39, no. 9, pp. 2702–2717, May 2018.
- [21] F. D. van der Meer *et al.*, "Multi- and hyperspectral geologic remote sensing: A review," *Int. J. Appl. Earth Obs. Geoinf.*, vol. 14, no. 1, pp. 112–128, Feb. 2012.
- [22] P. W. Yuen and M. Richardson, "An introduction to hyperspectral imaging and its application for security, surveillance and target acquisition," *Imaging Sci. J.*, vol. 58, no. 5, pp. 241–253, Oct. 2010.
- [23] L. M. Dale *et al.*, "Hyperspectral Imaging Applications in Agriculture and Agro-Food Product Quality and Safety Control: A Review," *Appl. Spectrosc. Rev.*, vol. 48, no. 2, pp. 142–159, Mar. 2013.
- [24] S. Ortega, H. Fabelo, D. K. Iakovidis, A. Koulaouzidis, and G. M. Callico, "Use of Hyperspectral/Multispectral Imaging in Gastroenterology. Shedding Some–Different–Light into the Dark," *J. Clin. Med.*, vol. 8, no. 1, p. 36, Jan. 2019.
- [25] P. Yu, M. Huang, M. Zhang, and B. Yang, "Optimal Wavelength Selection for Hyperspectral Imaging Evaluation on Vegetable Soybean Moisture Content during Drying," *Appl. Sci.*, vol. 9, no. 2, p. 331, Jan. 2019.
- [26] Y. Tan, *Fireworks Algorithm*. Berlin, Heidelberg: Springer Berlin Heidelberg, 2015.
- [27] S. F. C. Soares, A. A. Gomes, M. C. U. Araujo, A. R. G. Filho, and R. K. H. Galvão, "The successive projections algorithm," *TrAC Trends Anal. Chem.*, vol. 42, pp. 84–98, Jan. 2013.
- [28] W. Cai, Y. Li, and X. Shao, "A variable selection method based on uninformative variable elimination for multivariate calibration of near-infrared spectra," *Chemom. Intell. Lab. Syst.*, vol. 90, no. 2, pp. 188–194, Feb. 2008.
- [29] K. Nagasubramanian, S. Jones, S. Sarkar, A. K. Singh, A. Singh, and B. Ganapathysubramanian, "Hyperspectral band selection using genetic algorithm and support vector machines for early identification of charcoal rot disease in soybean stems," *Plant Methods*, vol. 14, no. 1, p. 86, Dec. 2018.

- [30] M. Wang, C. Wu, L. Wang, D. Xiang, and X. Huang, "A feature selection approach for hyperspectral image based on modified ant lion optimizer," *Knowledge-Based Syst.*, vol. 168, no. January, pp. 39–48, Mar. 2019.
- [31] S. Yu, S. De Backer, and P. Scheunders, "Genetic feature selection combined with composite fuzzy nearest neighbor classifiers for hyperspectral satellite imagery," *Pattern Recognit. Lett.*, vol. 23, no. 1–3, pp. 183–190, Jan. 2002.
- [32] N. Akhter, S. Dabhade, N. Bansod, and K. Kale, "Feature Selection for Heart Rate Variability Based Biometric Recognition Using Genetic Algorithm," no. 1, Springer Berlin Heidelberg, 2016, pp. 91–101.
- [33] S. E. Haupt and R. L. Haupt, "Genetic algorithms and their applications in environmental sciences," pp. 1–8.
- [34] S. N. Deepa and S. N. Sivanandam, "Introduction to Genetic Algorithms," Berlin, Heidelberg: Springer Berlin Heidelberg, 2008, pp. 15–37.
- [35] S. N. Sivanandam and S. N. Deepa, "Introduction to Particle Swarm Optimization and Ant Colony Optimization," in *Introduction to Genetic Algorithms*, Berlin, Heidelberg: Springer Berlin Heidelberg, 2007, pp. 403–424.
- [36] J. Robinson and Y. Rahmat-Samii, "Particle Swarm Optimization in Electromagnetics," *IEEE Trans. Antennas Propag.*, vol. 52, no. 2, pp. 397–407, 2004.
- [37] Eberhart and Yuhui Shi, "Particle swarm optimization: developments, applications and resources," in *Proceedings of the 2001 Congress on Evolutionary Computation (IEEE Cat. No.01TH8546)*, 2002, vol. 1, pp. 81–86.
- [38] M. Dorigo and C. Blum, "Ant colony optimization theory: A survey," *Theor. Comput. Sci.*, vol. 344, no. 2–3, pp. 243–278, Nov. 2005.
- [39] D. Martens, M. De Backer, R. Haesen, J. Vanthienen, M. Snoeck, and B. Baesens, "Classification With Ant Colony Optimization," *IEEE Trans. Evol. Comput.*, vol. 11, no. 5, pp. 651–665, Oct. 2007.
- [40] C. Blum, "Ant colony optimization: Introduction and recent trends," *Phys. Life Rev.*, vol. 2, no. 4, pp. 353–373, Dec. 2005.
- [41] S. Vapnik, V. N., & Kotz, *Estimation of Dependences Based on Empirical Data*, vol. 40. Springer New York, 2006.
- [42] F. Cheng, J. Zhang, Z. Li, and M. Tang, "Double distribution support vector machine," *Pattern Recognit. Lett.*, vol. 88, pp. 20–25, Mar. 2017.
- [43] C. J. Burges, *A tutorial on support vector machines for pattern recognition. Data mining and knowledge discovery.*, vol. 2. Springer Berlin Heidelberg, 1998.
- [44] Chih-Wei Hsu and Chih-Jen Lin, "A comparison of methods for multiclass support vector machines," *IEEE Trans. Neural Networks*, vol. 13, no. 2, pp. 415–425, Mar. 2002.
- [45] G. J. J. Van Den Burg and P. J. F. Groenen, "GenSVM: A generalized multiclass support vector machine," *J. Mach. Learn. Res.*, vol. 17, pp. 1–42, 2016.
- [46] Y. Li, H. Zhang, Q. Guo, and X. Li, "Machine Learning Methods for Ship Detection in Satellite Images," 2017.
- [47] H. Fabelo *et al.*, "HELICoiD project: A new use of hyperspectral imaging for brain cancer detection in real-time during neurosurgical operations," in *Proceedings of SPIE - The International Society for Optical Engineering*, 2016, vol. 9860.

- [48] H. Fabelo *et al.*, “An intraoperative visualization system using hyperspectral imaging to aid in brain tumor delineation,” *Sensors*, vol. 18, no. 2, 2018.
- [49] H. Fabelo *et al.*, “Spatio-spectral classification of hyperspectral images for brain cancer detection during surgical operations,” *PLoS One*, vol. 13, no. 3, pp. 1–27, Mar. 2018.
- [50] R. Salvador *et al.*, “Demo: HELICoiD tool demonstrator for real-time brain cancer detection,” in *Conference on Design and Architectures for Signal and Image Processing, DASIP*, 2017.
- [51] H. Fabelo *et al.*, “In-Vivo Hyperspectral Human Brain Image Database for Brain Cancer Detection,” *IEEE Access*, pp. 1–1, 2019.
- [52] A. H. Guedes, “Implementación de algoritmos de clasificación de imágenes hiperespectrales para la detección de tumores cerebrales sobre tarjetas gráficas programables.” 2016.
- [53] “Neurocirugía Contemporánea,” *CC Attribution-Share Alike 4.0 International*, 2011. [Online]. Available: <http://neurocirugiacontemporanea.com/doku.php?id=meninge>. [Accessed: 08-Jul-2019].
- [54] D. N. Louis *et al.*, “The 2016 World Health Organization Classification of Tumors of the Central Nervous System: a summary,” *Acta Neuropathol.*, vol. 131, no. 6, pp. 803–820, Jun. 2016.
- [55] H. Fabelo *et al.*, “Deep Learning-Based Framework for In Vivo Identification of Glioblastoma Tumor using Hyperspectral Images of Human Brain,” *Sensors (Basel)*, vol. 19, no. 4, 2019.
- [56] C.-L. Huang and J.-F. Dun, “A distributed PSO–SVM hybrid system with feature selection and parameter optimization,” *Appl. Soft Comput.*, vol. 8, no. 4, pp. 1381–1391, Sep. 2008.
- [57] Tianyou Zhang, Xiuju Fu, R. S. M. Goh, Chee Keong Kwoh, and G. K. K. Lee, “A GA-SVM feature selection model based on high performance computing techniques,” in *2009 IEEE International Conference on Systems, Man and Cybernetics*, 2009, no. October, pp. 2653–2658.
- [58] O. Kadri, L. H. Mouss, and M. D. Mouss, “Fault diagnosis of rotary kiln using SVM and binary ACO,” *J. Mech. Sci. Technol.*, vol. 26, no. 2, pp. 601–608, Feb. 2012.
- [59] Z. Tao, L. Huiling, W. Wenwen, and Y. Xia, “GA-SVM based feature selection and parameter optimization in hospitalization expense modeling,” *Appl. Soft Comput.*, vol. 75, pp. 323–332, Feb. 2019.
- [60] C. Chang and C. Lin, “LIBSVM : A Library for Support Vector Machines,” *ACM Trans. Intell. Syst. Technol.*, vol. 307, pp. 1–39, 2013.
- [61] P. Refaeilzadeh, L. Tang, and H. Liu, “Cross-Validation,” in *Implantable Bone Conduction Hearing Aids*, Basel: KARGER, 208AD, pp. 1–6.
- [62] M. A. Brovelli, M. Crespi, F. Fratarcangeli, F. Giannone, and E. Realini, “Accuracy assessment of high resolution satellite imagery orientation by leave-one-out method,” *ISPRS J. Photogramm. Remote Sens.*, vol. 63, no. 4, pp. 427–440, Jul. 2008.
- [63] Setia Pramana, “Resampling methods,” 2016. [Online]. Available: <https://es.slideshare.net/hafidztio/resampling-methods>. [Accessed: 09-Jul-2019].

-
- [64] A. G. Lalkhen and A. McCluskey, "Clinical tests: sensitivity and specificity," *Contin. Educ. Anaesth. Crit. Care Pain*, vol. 8, no. 6, pp. 221–223, Dec. 2008.
- [65] G. Grunau and S. Linn, "Detection and Diagnostic Overall Accuracy Measures of Medical Tests," *Rambam Maimonides Med. J.*, vol. 9, no. 4, p. e0027, Oct. 2018.
- [66] M. Stojanovic *et al.*, "Understanding sensitivity, specificity and predictive values," *Vojnosanit. Pregl.*, vol. 71, no. 11, pp. 1062–1065, 2014.
- [67] S. Boughorbel, F. Jarray, and M. El-Anbari, "Optimal classifier for imbalanced data using Matthews Correlation Coefficient metric," *PLoS One*, vol. 12, no. 6, pp. 1–17, Jun. 2017.
- [68] Y. Liu, J. Cheng, C. Yan, X. Wu, and F. Chen, "Research on the Matthews Correlation Coefficients Metrics of Personalized Recommendation Algorithm Evaluation," *Int. J. Hybrid Inf. Technol.*, vol. 8, no. 1, pp. 163–172, Jan. 2015.
- [69] T. Kanungo, N. S. Netanyahu, and A. Y. Wu, "An Efficient k-Means Clustering Algorithm: Analysis and Implementation," *IEEE Trans. Pattern Anal. Mach. Intell.*, vol. 24, no. 7, pp. 881–892, Aug. 2002.
- [70] R. S, S. Addamani, Venkat, and R. S, "Spectral Angle Mapper algorithm for remote sensing image classification," *IJISSET - Int. J. Innov. Sci. Eng. Technol.*, vol. 1, no. 4, pp. 201–205, Dec. 2014.